Multivariable Sliding-mode Extremum Seeking Control in Power Electronic Systems

by

Shirin Fartash Toloue

M.Sc., Ferdowsi University of Mashhad, Mashhad, Iran, 2014
B.Sc., Ferdowsi University of Mashhad, Mashhad, Iran, 2010

Thesis Submitted in Partial Fulfillment of the
Requirements for the Degree of
Doctor of Philosophy

in the
School of Mechatronic Systems Engineering
Faculty of Applied Sciences

SIMON FRASER UNIVERSITY
Fall 2019

Approval

Name:	**Shirin Fartash Toloue**
Degree:	**Doctor of Philosophy (Mechatronics)**
Title:	**Multivariable Sliding-mode Extremum Seeking Control in Power Electronic Systems**
Examining Committee:	**Chair:** Behraad Bahreyni Associate Professor
	Mehrdad Moallem Senior Supervisor Professor
	Jiacheng (Jason) Wang Supervisor Assistant Professor
	Krishna Vijayaraghavan Supervisor Associate Professor
	Mohammad Narimani Internal Examiner Lecturer
	Alireza Bakhshai External Examiner Professor Department of Electrical and Computer Engineering Queen's University
Date Defended:	**August 20, 2019**

Abstract

This thesis investigates the design and implementation of extremum seeking control with application to power electronics. To this end, a novel multivariable sliding-mode extremum seeking (MSES) scheme is developed and applied to several control and optimization problems involving maximum power point tracking (MPPT) and motor drives. The behavior of the controller in terms of convergence characteristics and stability is studied using nonlinear systems analysis tools.

The proposed MSES is utilized in three applications. First, we apply the concept to MPPT in an alternator-based energy conversion system. The objective is to achieve optimal power conversion at different speeds and output voltages of a Lundell alternator. The performance of the proposed controller is experimentally verified on a laboratory-scale setup through controlling the alternator field current and output voltage to gain fast and precise convergence and robust performance in face of disturbances and uncertainties.

In the second application, the proposed MSES is used to tune a proportional-integral (PI) controller which regulates the current of a permanent magnet synchronous motor (PMSM). The performance of the proposed MSES tuning method in terms of accuracy, parametric variations, and load torque disturbances is investigated through several experimental tests on a PMSM setup.

In the third application, the MSES concept is extended to a PMSM-drive system which emulates an exercise machine working at low speeds. In this case, the algorithm is modified to a multi-objective sliding-mode extremum seeking (MOES) optimization scheme for torque control of a PMSM as well as minimization of its torque ripples. To this end, the MSESC method is utilized to implement an adaptive iterative learning control (AILC) strategy for torque ripple minimization. The performance of the proposed MOES in terms of torque ripple suppression, steady state and transient performance, and load disturbance rejection is experimentally verified through synthesizing different mechanical impedances.

Keywords: multivariable extremum seeking, sliding-mode, maximum power point tracking, alternator-based energy conversion, PI tuning, permanent magnet synchronous motor, multi-objective extremum seeking, exercise machine.

Dedication

To my dear parents, Simin and Mohsen,
and my loving companion, Matin.

"Seek the wisdom that will untie your knot.
Seek the path that demands your whole being"

-Rumi

Acknowledgements

I would like to thank my senior supervisor, Prof. Mehrdad Moallem, for his invaluable support, guidance, and insightful discussions throughout this research. It was a privilege for me to work with him and learn from his experience. I also thank my other supervisors Dr. Jason Wang and Dr. Krishna Vijayaraghavan for providing valuable comments that helped me to improve this work.

I express my gratitude to the examining committee Dr. Alireza Bakhshai and Dr. Mohammad Narimani for accepting to be present in my defence. I also thank Dr. Behraad Bahreyni for chairing the defence session.

I acknowledge funding by the Natural Sciences and Engineering Research Council of Canada (NSERC). I also thank the Kaiser Foundation for providing me with the Kaiser Foundation Award for Digitally Controlled Power Electronics.

Many thanks go to my colleagues and labmates at the Motion and Power Electronic Control Laboratory (MPECL), specially Dr. Hossein Kamali and Dr. Yaser Mohammadian Roshan who directly contributed to the project.

Last but foremost, I give my deepest appreciation to my beloved husband, Matin Rahmatian, for all his patience and encouragement during this long journey. Finally but importantly, I express my humble gratitude to my parents, to whom I owe everything.

Table of Contents

List of Tables

List of Figures

Chapter 1

Introduction

1.1 Motivation of Research

Power electronic systems are developing rapidly in different industrial applications such as automation, energy conversion, utility systems, and etc [6,7,11,45]. By developing the power electronic systems, new problems and challenges arise which require to come up with new control strategies.

In many power electronic applications, there is a nonlinearity in the system and the objective is to regulate the system such that it achieves its optimal performance with minimal knowledge about the system model [2]. The nonlinearity might be in the plant, as a physical nonlinearity such as energy-conversion systems [16, 44, 48]. These systems mostly operate under a wide range of uncertain structural/environmental parameters and disturbances while it is desired to maximize the power generated by the system regardless of the magnitude of changes in parameters [24]. Moreover, in some applications, the nonlinearity might be in the control objective, added to the system through a cost functional of an optimization problem. One notable example of this scenario in power electronic applications is the fixed-gain proportional-integral-derivative (PID) controllers which are conventionally utilized for control of PMSMs [77, 100]. The conventional PID controllers are sensitive to parameter variations and load torque disturbances which leads to a degradation in PMSM control in terms of accuracy and robustness [50].

In recent years, considerable amount of research and development has been done for designing new control methods including adaptive and artificial intelligence controllers [51,57,67,88]. Although the proposed methods achieve some of the desired control objectives, they mostly rely on the full knowledge of the system and thus their performance is restricted by the accuracy of system model. Moreover, the proposed intelligent methods need to be trained beforehand. Also,

their functionality is degraded over time if they are not periodically trained. This motivates further studies which are provided in the coming parts of this thesis.

1.2 Background and Overview of the Present State of Technology

Conventional control methods are mainly applicable to systems with "known" set points and performance functions [2]. However, in many power electronic applications, the performance function is partially or totally unknown, and the objective is to regulate the system so that the output reaches the extremum (maximum/ minimum) value. This problem is called "Extremum-seeking" or "Self-optimizing" control [47].

In the past few years, extremum seeking has been vastly used in different engineering applications including control applications [10,97] as well as optimization problems [2,41]. The former domain mostly deals with tuning the system set points to achieve an optimal value of the output whereas the latter domain mostly considers tuning of parameters in a feedback law [97]. One of the foremost reasons for extensive use of extremum seeking controllers is that they are model-free and can be utilized in real-time optimization [2]. Consequently, they are appropriate for nonlinear time-varying systems with parametric uncertainties and systems with partially or totally unknown input-output characteristics. Different types of extremum seeking controllers have been proposed during the past decades [59,60,81,95,98]. In the following, two main ESC methods used in the literature are introduced.

1.2.1 Gradient-based Extremum Seeking Control

Gradient-based ESC is the most popular ESC method in the literature and has been applied in many different engineering applications [1, 10, 81, 95]. In this type of control, a perturbation- which is commonly a sine waveform- is added to the search signal and the optimum value is obtained by observing the effect of the perturbation on the performance function measurement. Fig. 1.1 depicts control block diagram of gradient-based ESC for a general nonlinear system with a performance function defined as $y = f(\theta)$ where θ is the input to the system which is controlled by the gradient-based extremum seeking control such that the optimal system output y is generated. In this study, it is crucial to note that all of the plant components are allowed to be unknown.

The system input is obtained by adding a sine perturbation signal to the adaptation input $\hat{\theta}$ [10]

$$\theta = a_2 sin(\omega t) + \hat{\theta}. \tag{1.1}$$

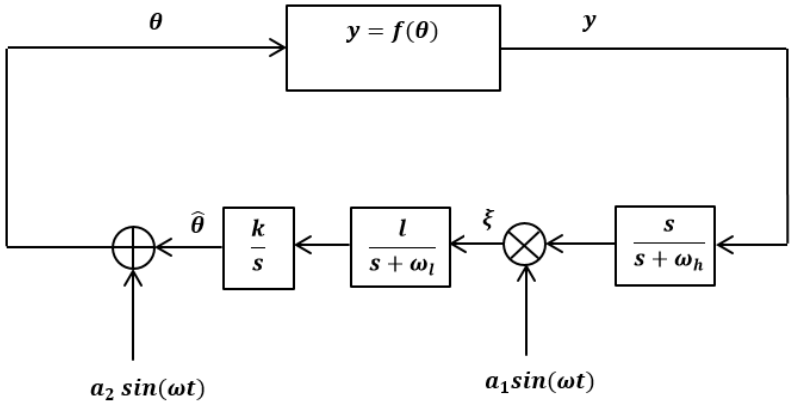

Figure 1.1: Control block diagram of gradient-based ESC [10].

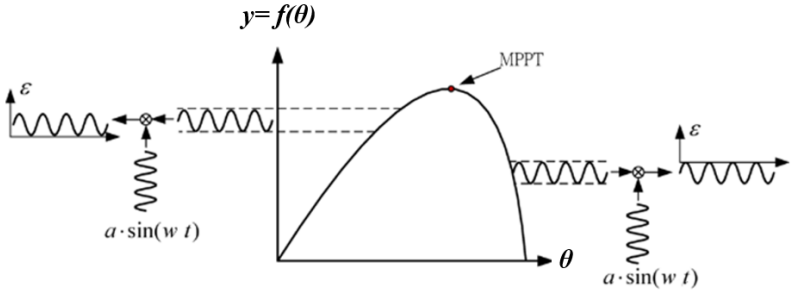

Figure 1.2: An illustration of a sinusoidal perturbation [95].

where a_2 is the amplitude and ω is the frequency of perturbation signal. In (1.1), the adaptation signal $\hat{\theta}$ shifts the sine waveform towards the gradient direction. The resultant value makes the modulation phase of the algorithm. The system response to signal θ is measured in the objective value y [10]

$$y = f(\hat{\theta} + a_2 sin(\omega t)). \tag{1.2}$$

Then, the output y is filtered by a high-pass filter so that its DC component is eliminated. The output of high-pass filter is demodulated by the same sine perturbation signal to extract the gradient direction which- with a slight abuse of notation- is obtained as

$$\xi = y(\frac{s}{s+h})(a_1 sin(\omega t)). \tag{1.3}$$

This concept is simply illustrated in Fig. 1.2. As can be seen, a small amount of sinusoidal perturbation is introduced to the system. In the case of a negative

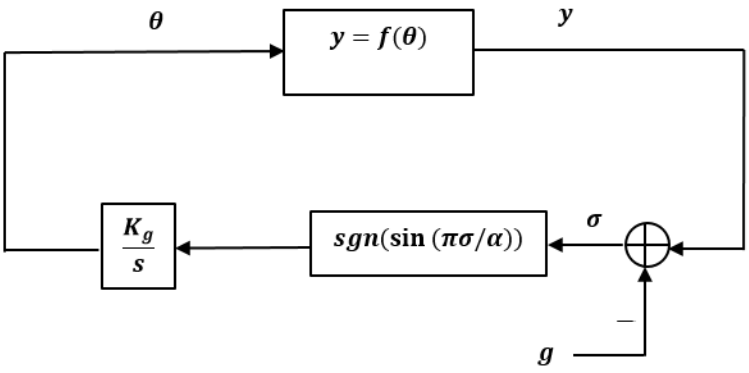

Figure 1.3: Multivariable gradient-based extremum seeking control [90].

(positive) ξ, the operation point lies on the right (left) side of the curvature, respectively.

Since only the DC component of demodulated signal is needed for gradient calculation, a low pass filter is applied to filter the demodulated signal ξ. This information is utilized to calculate the shift in the sine signal towards the gradient. This part of the algorithm is called the adaptation law and is calculated as follows

$$\hat{\theta} = -\xi(\frac{k}{s})(\frac{s}{s+h}). \tag{1.4}$$

where k is a positive constant that specifies the adaptation speed.

One main drawback of the gradient-based ESC is that the convergence speed and stability are dependent to the Hessian matrix [46]. This can severely reduce the effectiveness of gradient-based ESC in many different applications [3]. In early $70's$, Korovin and Utkin proposed sliding-mode ESC [42, 43]. In this approach, the system performance function is forced to remain on an increasing/decreasing sliding surface [10]. One main advantage of the sliding-mode ESC over the gradient-based ESC is that it does not require any gradient information of the system for optimization. Hence, it is more robust to the system dynamic changes and uncertainties [85].

1.2.2 Sliding-mode Extremum Seeking Control

The basic idea of this controller is to make f follow an increasing/ decreasing time function via sliding-motions [97, 98]. Consider the maximization of a performance function $y = f(\theta)$. In this problem, y is forced to track an increasing time function irrespective of the unknown gradient via sliding mode. A basic sliding-mode analog optimization method can be found in Fig(1.3).

Pick any increasing function $g(t)$ and try to keep $y - g(t)$ at a constant value by proper choice of $\dot{\theta}$. If so, $f(\theta)$ increases at the same rate as $g(t)$, independent of whether $\theta < \theta^\star$ or $\theta > \theta^\star$. To this end, let

$$\sigma = f(\theta) - g(t) \tag{1.5}$$

where $\dot{g}(t) = p$ for $p > 0$ in a maximization problem. So that

$$\dot{\sigma} = \frac{df}{d\theta}\dot{\theta} - \dot{g}(t) \tag{1.6}$$

with the optimizing law of [90]

$$\dot{\theta} = k\ sgn(sin(\pi\sigma/\alpha)) \qquad k > 0 \tag{1.7}$$

where k is a positive constant and sgn is a sign function. In (1.7), the gain k determines the convergence rate. The sine which is used in the signum function, helps the ESC algorithm to find correct direction of which the objective function becomes maximum. Moreover, α defines the bound on the error that is allowed by the system. Additionally, if the system is slower or faster than the driving signal, then chattering happens. The chattering frequency can be considerably decreased by decreasing the parameter α [97].

1.2.3 Multivariable Extremum Seeking and Its Application in Control and Optimization Case Studies

Most of the studies on ESC have focused on single-input-single-output (SISO) systems. However, there are many power electronic applications in which control/optimization is a multivariable problem [2]. This study focuses on the application of multivariable extremum seeking methods on three well-known problems in power electronics: MPPT in an alternator-based energy conversion system (reffered as a control problem), as well as PID and ILC tuning for PMSM current regulation and torque ripple minimization, respectively (referred as two important power electronic optimization problems).

Control Problem: MPPT in an Alternator-based Energy Conversion System

One well-known multivariable control example in power electronics is MPPT in alternator-based energy conversion system. In this system, the output power of the alternator depends on its shaft driving speed and load voltage at the output [75]. Thus, to achieve energy-efficient power conversion, it is imperative that the alternator works at its optimal point for different speeds and load voltages.

In [66] and [65], a switched-mode rectifier (SMR) load-matching technique is utilized for a Lundell alternator. In this case, two parameters have to be controlled for power maximization; namely, the alternator field current and the duty ratio of the DC/DC boost converter. The only applied control algorithm for alternator MPPT in multivariable case is a decentralized controller proposed in [66]. The proposed controller is a combination of an individual field controller to control the field current and a control limiter followed by a comparator to control the duty ratio of the converter switch. The main drawbacks of the decentralized ESC are its high cost and low efficiency [23].

As a good candidate, multivariable extremum seeking control (MESC) can be applied to the system to maximize the alternator output power through controlling the input variables of the system. In this work, the application of MESC for MPPT in a Lundell alternator-based energy conversion system is studied.

Optimization Problem: PID Tuning in PMSM Current Regulation

As an important optimization example one can refer to PID tuning in PMSM current regulation. In recent years, several systematic PID tuning methods have been proposed. For instance, trial-and-error [80], Ziegler-Nichols [34], and internal model control (IMC) [27] are some of the most popular PID tuning methods that have been proposed in different PMSM control applications. However, these methods utilize off-line tuning algorithms which lack the capability to handle time-varying uncertainties. Moreover, they rely on the full knowledge of the system model and thus their performance is restricted by the accuracy of PMSM model. In [67], a model reference adaptive control (MRAC) technique for PID tuning has been proposed. Although the proposed method can vary the gains online, it is dependent on the system model and precise values of its parameters. Artificial intelligence methods for PID tuning has also been utilized in PMSM control applications. In [36], a fuzzy approach has been presented for PID tuning. The proposed method uses off-line tuning and it cannot deal with time-varying uncertainties. In [35], a neural network control technique has been applied for PID tuning in direct torque control of PMSM drive. Although the proposed tuning method can approximate the nonlinear mapping through learning, it suffers from high computational burden which may be restrictive in practical applications.

Recently, extremum seeking as a real-time adaptive optimization method has been proposed for tuning the PID gains [40, 41]. The extremum seeking method modifies the PID parameters iteratively by minimizing a cost function which characterizes the desired performance of the system. In [41], a multivariable

gradient-based ES method has been proposed for PID tuning. The working principle of this scheme is presented in subsection 1.2.4.

Optimization Problem: ILC Tuning in PMSM Torque Ripple Minimization

When a PMSM is operating at low speeds, torque ripples are inevitable and a proper control method should be used such that the ripples are suppressed while the system tracks a desired torque [71, 92].

Several methods have been proposed to minimize the effect of torque ripples in PMSM drive systems. Broadly, the research can be divided into two main directions: (i) Improving the motor design [31, 101], and (ii) Utilizing more advanced control techniques [20,58]. While the motor design approach is restrictive by numerous factors such as cost and complexity, great advances have been made in utilizing control techniques [30, 52]. To this end, early works have focused on controlling the stator excitation currents to generate ripple-free torque profiles. These methods require adequate knowledge about the motor or plenty of off-line tests for system identification and fail to control the drive system properly due to parameter variations and disturbances (see e.g., [68, 92]).

Recently, ILC has been utilized in PMSM torque ripple minimization. This method does not require a detailed plant model and is based on learning the desired control input by iteratively updating the input so as to reduce the periodic torque pulsations [72]. In [49], a proportional type discrete ILC which incorporates both the previous cycle error information and current cycle error feedback has been proposed. Torque ripple contains non-periodic components which cannot be suppressed by ILC, resulting in accumulative effect due to non-periodic disturbances. To alleviate this problem a forgetting factor has been incorporated in the learning law of ILC in [68]. The value of the proportional gain and forgetting factor in ILC have significant effect on steady state and dynamic performance of the system and should be selected based on a compromise between torque ripple suppression and stability.

Utilizing adaptive gains in the ILC scheme improves the convergence rate and dynamic performance of the system. In [89], a parameter optimization-based ILC has been proposed to adjust the forgetting factor online to achieve torque ripple reduction, while speed up the convergence rate and improve the dynamic performance of the system compared with the conventional fixed-gain ILC. However, the learning gain is fixed and no study is conducted on the effect of learning gain on torque suppression in dynamic/steady state condition. In [99], a variable gain ILC has been proposed to remove measurement uncertainties and guarantee the tracking error convergence to zero. However, in this approach the

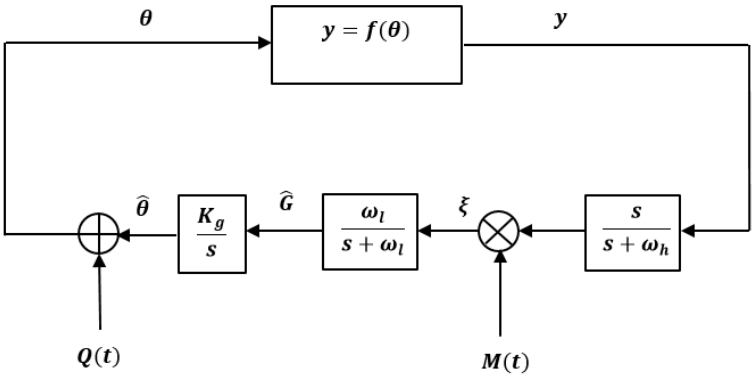

Figure 1.4: Multivariable gradient-based extremum seeking control [90].

time domain uncertainty is not considered. In [91], a predictive variable gain has been proposed which covers the drawbacks of the adaptive ILC proposed in [99]. However, it requires the precise parameters of PMSM model for eliminating undesirable vibrations of PMSM system.

In this work, multivariable extremum seeking is utilized for PMSM torque ripple minimization . The proposed approach requires minimal knowledge about the motor parameters. Hence, it can be utilized in any tracking application involving PMSM operating at low speeds such as position sensorless drives [26], robotics [56], machine tools [79], and haptic interfaces [32].

1.2.4 Multivariable Gradient-based Extremum Seeking Control

Extending the gradient-based ESC to the multivariable case is done by assigning a sine waveform to every input channel with some phase shift [23]. Fig. (1.4), shows the multivariable gradient-based ES design, where K_g is a positive definite diagonal matrix, and the perturbation signals are defined as [23]

$$Q(t) = a_1[sin(\omega_1 t) \;\; sin(\omega_2 t) \;\; ... \;\; sin(\omega_n t)^T \tag{1.8}$$

$$M(t) = a_2[sin(\omega_1 t) \;\; sin(\omega_2 t) \;\; ... \;\; sin(\omega_n t)]^T \tag{1.9}$$

where ω_j/ω_k are rational for all j and k, and a_1 and a_2 are real numbers, with the frequencies chosen such that $\omega_j \neq \omega_k$ and $\omega_j + \omega_k \neq \omega_m$ for distinct j, k and m.

In particular, the design derives an estimate θ of the gradient vector by adding the probing signal Q to the estimate $\hat{\theta} = [\hat{\theta_1} \;\; \hat{\theta_2} \;\; ... \;\; \hat{\theta_n}]^T$ [23].

Multivariable gradient-based ESC helps to reduce the hardware costs and increase the efficiency of the control/ optimization. However, as mentioned earlier, one main drawback of this control method is that it depends on the gradient

information. Moreover, due to the high magnitude switching of gradient term, the gradient-based ES fails to reject the effect of disturbances and parameter variations appropriately [86]. This is specifically critical in MPPT tracking of alternator based system which works at various speeds and load uncertainties are inevitable. This is also crucial in PMSM current regulation and torque ripple minimization for which PID and ILC are sensitive to parameter variations and load torque disturbances.

1.3 Summery of Contributions and Outline of the Dissertation

Regarding the drawbacks of multivariable gradient-based extremum seeking controller, it is desired to design a more efficient, gradient-independent multivariable ESC. To this end, multivariable sliding-mode extremum seeking control would be a good candidate to address the mentioned problems. Although certain studies can be found in the literature on multivariable sliding-mode control [28, 37, 61, 74, 82], to the best of my knowledge, no studies have been conducted on multivariable sliding-mode extremum seeking control. In this work, a novel multivariable sliding-mode extremum seeking control scheme is proposed and its application is studied in several power electronic control/optimization problems. In this regard, the contributions of this thesis are summarized as follows:

1.3.1 Chapter 2: Multivariable Sliding-mode Extremum Seeking Control

This chapter provides the ground work upon which the rest of the thesis is developed. In the beginning, the design principle for the proposed multivariable sliding-mode extremum seeking controller is presented. It is shown that the proposed controller extends conventional scalar sliding-mode ESC by defining multiple sliding surfaces through a sliding manifold vector with different control parameters. In the following, convergence and stability analysis of the proposed controller both outside and inside the ϵ-vicinity of the extremum point is studied. The results of this chapter are used in chapter 3 as a control framework for MPPT in an alternator energy conversion system. The outcomes of research presented in this chapter have been published in [19], [85], and [87].

1.3.2 Chapter 3: MPPT in an Alternator-based Energy Conversion System

In this chapter, the application of the proposed controller presented in chapter 2 is studied for MPPT of a laboratory-scale alternator-based energy conversion system. The proposed MSES controller maximizes the alternator output power at various speeds by controlling the alternator's field current and its output voltage. Furthermore, the performance of the proposed controller is compared with a multivariable gradient-based method through experimental studies. The results demonstrate that the proposed controller offers advantages in terms of speed, accuracy, and robust performance. The outcomes of research presented in this chapter have been published in [19], and [87].

1.3.3 Chapter 4: Extremum Seeking PI Tuning for PMSM Current Regulation

High-performance current control is critical for obtaining smooth output torque in PMSMs. To this end, the application of the proposed MSES scheme for PI tuning in PMSM current regulation is studied in this chapter. The proposed MSES tuning optimizer varies the PI gains by minimizing a cost function based on the feedback error term. The resulting PI controller can achieve fast and accurate tracking response, high disturbance rejection, and low sensitivity to PMSM parameter variations. Furthermore, the stability of proposed control strategy is investigated through a Lyapunov analysis and its performance is evaluated through experimental studies. The results indicate that the proposed controller can offer improved performance in terms of accuracy, parametric variations, and load torque disturbances when compared with a conventional PI and a recently proposed PI controller using gradient-based extremum seeking tuning method. The simulation results of this study were published in [86]. The experimental outcomes have been published in [17].

1.3.4 Chapter 5: PMSM Torque Ripple Minimization and Control using Multi-objective Extremum Seeking Control

When a PMSM is operating at low speeds, torque ripples are inevitable and a proper control method should be used such that the ripples are suppressed while the system tracks a desired torque. To this end, a multi-objective extremum-seeking (MOES) approach is proposed for torque control of a PMSM and minimization of its torque ripple. The latter aspect is important in human-machine interface applications such as haptic devices requiring smooth torque profiles at slow speeds. The proposed MOES scheme combines an adaptive iterative learning control (AILC) method with an adaptive PI controller which makes

the system less sensitive to load disturbances and improves the control performance for torque regulation during transient events. Experiments are performed on a proof-of-concept exercise machine that generates desired torque profiles and mechanical impedances based on user's preference. The performance of the proposed controller is further compared with a recently proposed adaptive PI controller. The experimental results validate the effectiveness of the proposed controller in terms of torque ripple suppression, steady state and transient performance, as well as load disturbance rejection. The research outcomes presented in this chapter have been published in [18].

1.3.5 Chapter 6: Conclusions and Suggestions for Future Works

The research outcomes and achievements are summarized in this chapter. General conclusions are made based on the theories, simulations and experiments provided in the thesis. Some ideas that have been generated during the whole project but have not had a chance to be investigated are suggested as future works.

Chapter 2

Multivariable Sliding-mode Extremum Seeking Control

In this chapter, a novel multivariable sliding-mode extremum seeking controller is proposed. The proposed controller combines the merits of multivarible sliding mode with ESC. In particular, the use of model-free ES makes the controller independent of the system model [23]. Besides, sliding-mode control can provide robust performance [28, 37, 61, 69, 74, 82]. The proposed controller extends conventional scalar sliding mode ESC proposed in [62–64, 96, 97] by defining multiple sliding surfaces through a sliding manifold vector with different control parameters. Due to applying multivariable sliding-mode control, fast and smooth convergence along with robust performance can be achieved. Furthermore, in contrast to decentralized ESC, it only applies one control loop for maximization/minimization. A rigorous study is conducted on convergence and stability analysis of the proposed controller both outside and inside the ϵ-vicinity of the extremum point. In the outside region, a Lyapunov-like function is introduced and its stability characteristics are obtained in the multivariable case. In the inside region, different cases that may arise as the system enters this region are studied. Finally, a theorem is presented for convergence of the system both outside and inside the ϵ-vicinity of the extremum point. The control principles presented in this chapter have been used in next chapters in different power electronic control/optimization problems.

This chapter is organized as follows. In section 2.1, the proposed multivariable sliding-mode extremum seeking controller is presented. In section 2.2, the convergence and stability analysis of the proposed controller is fully studied both outside and inside the ϵ-vicinity of the extremum point. Finally, section 2.3 concludes from this chapter.

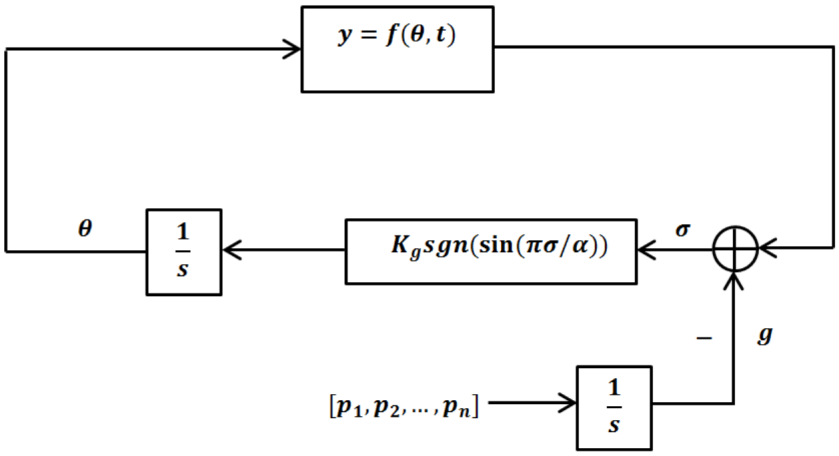

Figure 2.1: Control block diagram of multivariable sliding-mode ESC.

2.1 Controller Design

Consider the block diagram shown in Fig. 2.1. The performance function of the system is generally represented as follows

$$y(t) = f(\boldsymbol{\theta}, t) \tag{2.1}$$

where $f : \mathbb{R}^n \rightarrow \mathbb{R}$, $y \in \mathbb{R}$ is the output, t is time and $\boldsymbol{\theta} = [\theta_1 \ \ \theta_2 ... \theta_n]$ is the vector of n parameters to be controlled. $f(\boldsymbol{\theta}, t)$ is partially or totally unknown and the objective is to control $\boldsymbol{\theta}$ such that f is maximized (or minimized).

Without loss of generality, assume that $f(\boldsymbol{\theta}, t)$ has a maximum point. The proposed controller applies n sliding surfaces to control n parameters of the system. Let us define the sliding-surface vector $\boldsymbol{\sigma(t)}$ as follows

$$\boldsymbol{\sigma(t)} = [\sigma_1 \ \ \sigma_2 \ \ .... \ \ \sigma_n] \tag{2.2}$$

where

$$\sigma_i = y - p_i t \tag{2.3}$$

in which $p_i > 0 \quad (i = 1, 2, ..., n)$ is the slope of i^{th} sliding surface. The vector of driving signals is defined as follows

$$\boldsymbol{p} = [p_1 \ \ p_2 \ \ ... \ \ p_n] \tag{2.4}$$

Accordingly, $\boldsymbol{g(t)}$ is defined as

$$\dot{\boldsymbol{g}}(\boldsymbol{t}) = \boldsymbol{p} \tag{2.5}$$

where $\boldsymbol{g(t)}$ is an increasing function with $p_i > 0$ $(i = 1, ..., n)$ for the maximization problem. By selecting the sliding-surface vector as (2.2), the goal is to reach the sliding surfaces and remain on them thereafter.

The optimizing control law is defined such that stability of the system is guaranteed. To this end, the following control law is defined for the system

$$\dot{\boldsymbol{\theta}} = K_g sgn(sin(\frac{\boldsymbol{\pi\sigma}}{\alpha})) \tag{2.6}$$

where $sgn(.)$ is a signum function, $\boldsymbol{\alpha} = [\alpha_1 \ \ \alpha_2 ... \ \ \alpha_n]$ is a $1 \times n$ vector for which each element is a positive constant. $K_g = diag([k_{g1}, ..., k_{gn}])$ is an $n \times n$ diagonal positive definite matrix which determines the convergence rate. Since the performance function is not known, the periodic switching signal $sgn(sin(\frac{\boldsymbol{\pi\sigma}}{\alpha}))$ is applied to find the direction in which the system becomes maximized. The multivariable sliding mode ESC achieves the maximum point of the system by forcing f to remain on the increasing sliding surface vector, i.e $\boldsymbol{\sigma(t)} \to 0$. On the sliding-mode vector, the performance function f increases with the increasing of the reference function $g(t)$ and the system moves toward the maximum vector $\boldsymbol{\theta^*}$.

Choosing the controller parameters properly guarantees the stability of the system. In [98], a study is conducted for selecting the parameters in a scalar sliding-mode ESC. A similar procedure can be extended to the multivariable case as discussed in current work. As k_{gi} becomes larger, the convergence rate to the extremum point increases. Moreover, α has to be selected as a small positive constant so that sliding motions occur for $k_{gi}|\frac{df}{d\theta_i}| > |\dot{g}_i|$ $(i = 1, 2, ..., n)$, and the error $e(t)$ approaches zero with a bandwidth of ζ. In this case, $\boldsymbol{\theta}$ converges to $\boldsymbol{\theta^*}$ within a finite time. The region defined by $|\frac{df}{d\theta_i}| > |\dot{g}_i|/k_{gi}$ $(i = 1, 2, ..., n)$, quantifies $\boldsymbol{\theta}$ with the optimizing law (2.6). The stability and convergence conditions for ESC in a multivariable setting are presented in the following section.

2.2 Convergence and Stability Analysis in Multivariable Sliding-mode Extremum Seeking Controller

In this section, convergence analysis is conducted for both outside and inside an ϵ-vicinity of the maximum. For a system with multivariable performance function, the ϵ-vicinity of the maximum can be considered as a surface for $\theta_1, \theta_2, ..., \theta_n$, whereas for the j^{th} input it can be defined as follows:

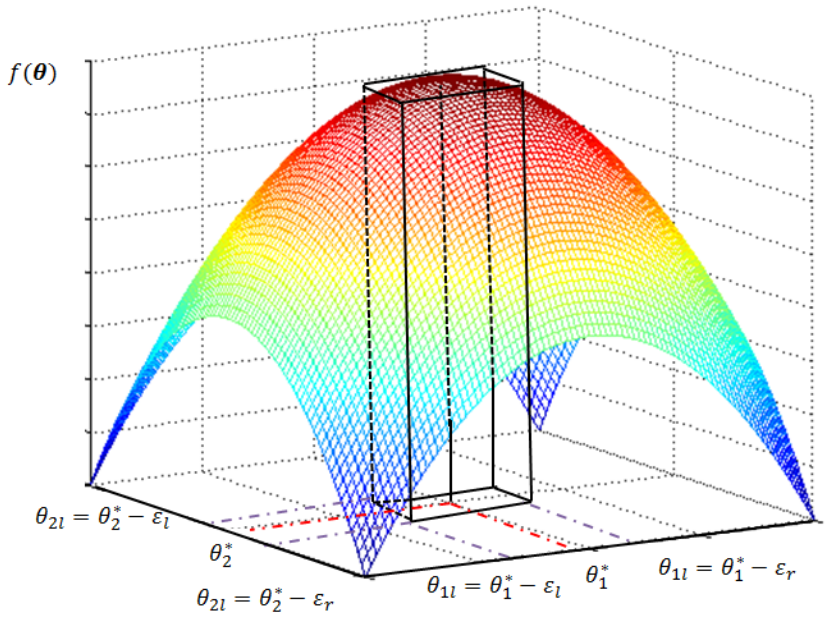

Figure 2.2: A 3D example of ϵ-vicinity surface for a two-variable performance function.

$$\theta^*_{j(\epsilon_l,\epsilon_r)} = \{\theta_j | \theta_j^* - \epsilon_l \leq \theta_j \leq \theta_j^* + \epsilon_r\} \quad j = 1, 2, ..., n \tag{2.7}$$

where ϵ_l and ϵ_r are positive constants. Accordingly, the following holds for the regions near the maximum

$$\begin{cases} |\frac{\partial f}{\partial \theta_j}| > \frac{p_j}{k_{gj}} & \forall \theta_j \overline{\in} \theta^*_{j(\epsilon_l,\epsilon_r)} \quad j = 1, 2, ..., n \\ |\frac{\partial f}{\partial \theta_j}| < \frac{p_j}{k_{gj}} & \forall \theta_j \in \theta^*_{j(\epsilon_l,\epsilon_r)} \\ |\frac{\partial f}{\partial \theta_j}| = \frac{p_j}{k_{gj}} & for \;\; \theta_j = \theta_j^* - \epsilon_l \;\; or \;\; \theta_j = \theta_j^* + \epsilon_r \end{cases} \tag{2.8}$$

Fig. 2.2 illustrates a simple example for ϵ-vicinity surface of the maximum of a two-variable performance function.

2.2.1 Case 1: Stability and Convergence Analysis outside the ϵ-vicinity of the maximum

Assume $\theta_j(0)$ is outside the ϵ-vicinity of the maximum, i.e. $\theta_j \overline{\in} \theta^*_{j(\epsilon_l,\epsilon_r)}$; hence, $|\frac{\partial f}{\partial \theta_j}| > \frac{p_j}{k_{gj}}$. In this region, convergence analysis of the proposed controller is conducted using a Lyapunov-like function as follows

$$V = \frac{1}{2}\boldsymbol{\sigma}\boldsymbol{\sigma}^T \tag{2.9}$$

The time derivative of V is

$$\dot{V} = \dot{\boldsymbol{\sigma}}\boldsymbol{\sigma}^T = (\frac{\partial f}{\partial \boldsymbol{\theta}}\dot{\boldsymbol{\theta}} - \boldsymbol{p})\boldsymbol{\sigma}^T \tag{2.10}$$

Considering (2.6), $\dot{V}$ can be rewritten as

$$\dot{V} = (\frac{\partial f}{\partial \boldsymbol{\theta}} K_g sgn(sin(\frac{\pi \boldsymbol{\sigma}}{\alpha})) - \boldsymbol{p})\boldsymbol{\sigma}^T \tag{2.11}$$

To guarantee stability of the system, $\dot{V}$ should be negative. The terms $\frac{\partial f}{\partial \boldsymbol{\theta}}$ and $\boldsymbol{p}$ are $1 \times n$ vectors. Moreover, K_g and $sgn(.)$ are considered to be $n \times n$ diagonal matrices. Hence, we can write $\boldsymbol{a} = (\frac{\partial f}{\partial \boldsymbol{\theta}} K_g sgn(sin(\frac{\pi \boldsymbol{\sigma}}{\alpha})) - \boldsymbol{p})$ in the following form

$$\boldsymbol{a} = \begin{bmatrix} \frac{\partial f}{\partial \boldsymbol{\theta_1}} & .... \frac{\partial f}{\partial \boldsymbol{\theta_n}} \end{bmatrix} \begin{bmatrix} k_{g1} & 0 & \cdots & 0 \\ 0 & k_{g2} & \cdots & 0 \\ \vdots & \vdots \ddots & \vdots & \\ 0 & 0 & \cdots & k_{gn} \end{bmatrix} \times$$
$$\begin{bmatrix} sgn(sin(\frac{\pi\sigma_1}{\alpha_1}))) & 0 & \cdots & 0 \\ 0 & sgn(sin(\frac{\pi\sigma_2}{\alpha_2}))) & \cdots & 0 \\ \vdots & \vdots \ddots & \vdots & \\ 0 & 0 & \cdots & sgn(sin(\frac{\pi\sigma_n}{\alpha_n}))) \end{bmatrix}$$
$$- \boldsymbol{p} \tag{2.12}$$

since K_g and $sgn(.)$ are diagonal matrices, $\boldsymbol{a}$ is obtained as a vector. Therefore, each entry of $\boldsymbol{a}$ is as follows

$$\boldsymbol{a}_j = \Big(\frac{\partial f}{\partial \theta_j} k_{gj} \big(sgn(sin(\frac{\pi\sigma_j}{\alpha_j}))\big)\Big) - p_j \tag{2.13}$$

Accordingly, (2.11) can be rewritten as

$$\dot{V} = \boldsymbol{a}\sigma^T = \sum_{1 \le j < n} a_j \sigma_j \tag{2.14}$$

For stability, it is sufficient that each term of (2.14) be negative. Let us consider the region $\frac{\partial f}{\partial \theta_j} > 0$. If $2k\alpha_j < \sigma_j(0) < 2(k+1)\alpha_j$, then $sgn(sin(\frac{\pi\sigma_j}{\alpha_j}))) < 0$, and (2.14) can be re-written as

$$\dot{V} = \sum_{1 \le j < n} \Big(- \frac{\partial f}{\partial \theta_j} k_{gj} - p_j \Big) \mid \sigma_j \mid \tag{2.15}$$

Hence, one can conclude $\dot{V} < 0$ and σ_j is kept at the sliding manifold $\sigma_j = (2k+1)\alpha_j$. Now, assume that $\frac{\partial f}{\partial \theta_j} < 0$. If $(2k-1)\alpha_j < \sigma_j(0) < (2k+1)\alpha_j$,then $sgn(sin(\frac{\pi\sigma_j}{\alpha_j}))) > 0$ and with a similar inference, (2.15) can be written as

$$\dot{V} = \sum_{1\leq j<n} \Big(\frac{\partial f}{\partial \theta_j} k_{gj} - p_j\Big) \mid \sigma_j \mid \tag{2.16}$$

Considering the sliding-mode existence region $k_{gj}|\frac{\partial f}{\partial \theta_j}| - p_j > 0$, one can conclude $\dot{V} < 0$ and σ_j is kept at the sliding manifold $\sigma_j = 2k\alpha_j$.

In the following, a convergence analysis is conducted to prove asymptotic stability of the controller in the multivatiable case. Suppose that the sliding manifolds $\forall \sigma_j = m_j\alpha_j$ are initially in the region $\frac{\partial f}{\partial \theta_j} > 0$ and $(m_j-1)\alpha_j < \sigma_j < (m_j+1)\alpha_j$ at time t_1 with the centre line $m_j\alpha_j$ and width of $2\alpha_j$. In case of stability, if $\sigma_j(t_1) > m_j\alpha_j$, σ_j will converge to $m_j\alpha_j$. In case of instability ($\dot{V} > 0$), $\sigma_j(t_1)$ leaves the region during the time interval τ_j. Let us define a vector of time delays for n sliding surfaces as $\boldsymbol{\tau} = [\tau_1 \ \ \tau_2 ... \ \ \tau_n]$. The aim is to make σ_j remain on the sliding-mode existence region of $(m_j-1)\alpha_j < \sigma_j < (m_j+1)\alpha_j$. In [97], a condition is defined to reach convergence in the scalar case. Here, we extend this condition to the multivariable case as follows

$$\sum_{1\leq j<n} \left(\Big| [- \frac{\partial f}{\partial \theta_j} k_{gj} - p_j] \tau_j \Big| - \alpha_j \right) \leq \sum_{1\leq j<n} \left(\Big(\frac{\partial f}{\partial \theta_j} k_{gj} - p_j\Big)\Big(\frac{\alpha_j}{\frac{\partial f}{\partial \theta_j} k_{gj} + p_j} + \tau_j\Big)\right) \tag{2.17}$$

Since $\frac{\partial f}{\partial \theta_j} > 0$ and $p_j > 0$, (5.27) can be rewritten as follows

$$\sum_{1\leq j<n} \frac{\partial f}{\partial \theta_j} k_{gj}\tau_j + \sum_{1\leq j<n} \tau_j p_j \leq \left(\frac{\sum_{1\leq j<n} \frac{\partial f}{\partial \theta_j} k_{gj} - \sum_{1\leq j<n} p_j}{\sum_{1\leq j<n} \frac{\partial f}{\partial \theta_j} k_{gj} + \sum_{1\leq j<n} p_j} + 1 \right) \sum_{1\leq j<n} \alpha_j + \sum_{1\leq j<n} (\frac{\partial f}{\partial \theta_j}) k_{gj}\tau_j - \sum_{1\leq j<n} p_j\tau_j \tag{2.18}$$

Let us define the fractional part as

$$\phi = \frac{\sum_{1\leq j<n} \frac{\partial f}{\partial \theta_j} k_{gj} - \sum_{1\leq j<n} p_j}{\sum_{1\leq j<n} \frac{\partial f}{\partial \theta_j} k_{gj} + \sum_{1\leq j<n} p_j} + 1 \tag{2.19}$$

Further algebraic manipulations result in

$$2 \sum_{1\leq j<n} \tau_j p_j \leq \phi \sum_{1\leq j<n} \alpha_j \tag{2.20}$$

Hence, it can be concluded that $2\boldsymbol{\tau}\boldsymbol{p}^T \leq \phi \sum_{1\leq j<n} \alpha_j$.

Equation (5.30) can be simplified to $2\boldsymbol{\tau p}^T \leq \sum_{1<j<n} \alpha_j$. This leads to a larger sliding-mode existence region to guarantee stability in a larger area. Hence, through satisfaction of the above goals, the system will stably converge to the ϵ-vicinity of the maximum $f(\boldsymbol{\theta^*})$.

2.2.2 Case 2: Convergence Analysis inside the ϵ-vicinity of the maximum

In the ϵ-vicinity of the maximum, the reaching condition does not hold. In this case, two different states can be considered for the system:

1) The system converges to the maximum with oscillations;

2) The system moves through the ϵ-vicinity, goes outside and switches among the sliding mode vectors.

Assume that at $t = t_0$, the system enters the ϵ-vicinity of the maximum as shown for case 1 in Fig. 2.3. This figure can be interpreted as projection of the multi-dimensional performance function $f(\boldsymbol{\theta})$ on one surface along with one of the θ_j axes. Here, the projection of f is defined as

$$\boldsymbol{proj}_{\theta_j}(f(\boldsymbol{\theta})) = \xi(\theta_j) \tag{2.21}$$

Without loss of generality, assume that $\theta_j(t_0)$ is at the left side of the ϵ-vicinity

$$\theta_j(t_0) = \theta_j^* - \epsilon_l \quad j = 1, 2, ..., n \tag{2.22}$$

Moreover, $-\alpha_j < \sigma_j(t) < 0$. Here, the reaching condition does not hold. In this case, $|\frac{\partial f}{\partial \theta_j}| < \frac{p_j}{k_{gj}}$ is satisfied and the convergence speeds of $\theta_j(t)$ and $\sigma_j(t)$ are respectively obtained as follows:

$$\dot{\theta_j}(t) = k_{gj} sgn(sin(\pi\sigma_j(t)/\alpha)) = k_{gj} > 0 \tag{2.23}$$

$$\dot{\sigma_j}(t) = k_{gj} \frac{\partial f}{\partial \theta_j} sgn(sin(\pi\sigma_j(t)/\alpha)) - p_j < 0 \tag{2.24}$$

According to (2.23), $\theta_j(t)$ will increase. Therefore, considering $\frac{\partial f}{\partial \theta_j} > 0$, the system will move towards the maximum θ_j^* for $t > t_0$. It may reach the maximum or may even move across it while $\dot{\sigma_j}(t)$ keeps decreasing.

Now, consider the case that the parameter $\theta_j(t)$ moves across the maximum θ_j^* as shown for case 1 in Fig. 2.3. In this case, $\frac{\partial f}{\partial \theta_j}$ changes sign, i.e. $\frac{\partial f}{\partial \theta_j} < 0$ and $0 < \sigma_j(t) < \alpha_j$. Hence, the relations shown above are replaced by

$$\dot{\theta_j}(t) = k_{gj} sgn(sin(\pi\sigma_j(t)/\alpha)) = -k_{gj} < 0 \tag{2.25}$$

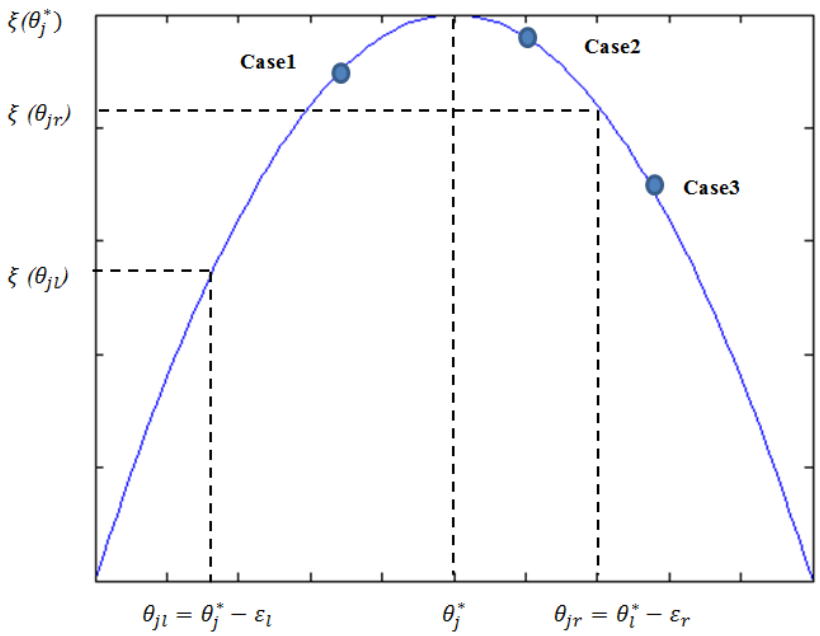

Figure 2.3: Two cases about the direction of motion for $\theta_j(t)$.

$$\dot{\sigma_j}(t) = k_{gj}\frac{\partial f}{\partial \theta_j} sgn(sin(\pi\sigma_j(t)/\alpha)) - p_j < 0 \tag{2.26}$$

As a result, parameter $\theta_j(t)$ changes its direction of motion after reaching the next sliding surface. It can be seen that inside the ϵ-vicinity, the system converges to the maximum $\boldsymbol{\theta^*}$ with oscillations.

Without loss of generality, assume that $\theta_j(t)$ moves from $\theta_j^* - \epsilon_l^*$ to $\theta_j^* + \epsilon_r^*$, from which the necessary time interval is determined by

$$\Delta t = \frac{\epsilon_l + \epsilon_r}{k_{gj}} \tag{2.27}$$

Defining $\Delta\xi_j$ as $\Delta\xi_j = \xi_j(\theta_r) - \xi_j(\theta_l)$ when $\theta_j(t)$ moves from surface $\sigma_j t_0$ to $\sigma_{j-1}(t_0 + \Delta t) = \sigma_j(t_0 + \Delta t) + \alpha_j$, we have

$$\sigma_{j-1}(t_0 + \Delta t) = \Delta\xi_j - p_j\frac{\epsilon_l + \epsilon_r}{k_{gj}} + \alpha_j \tag{2.28}$$

In this case, at $t = t_0 + \Delta t$,and for $\sigma_{j-1}(t_0 + \Delta t) < 0$ the following holds

$$\frac{\Delta\xi_j + \alpha_j}{\epsilon_l + \epsilon_r} \leq \frac{p_j}{k_{gj}} \tag{2.29}$$

If (2.29) does not hold, i.e., $\frac{\Delta\xi_j+\alpha_j}{\epsilon_l+\epsilon_r} > \frac{p_j}{k_{gj}}$ is outside the ϵ-vicinity of the maximum.

For simplicity, the projection of cost function $\xi(\theta_j, t)$ can be assumed to be symmetrical about the maximum θ_j^*. Hence,

$$\xi(\theta_j(t)) = \xi(-\theta_j(t)) \qquad \theta_j \in \theta^*_{j\epsilon_l,\epsilon_r} \tag{2.30}$$

$$\epsilon_l = \epsilon_r = \epsilon \tag{2.31}$$

$$\Delta\xi_j = \xi(\theta_{jr}) - \xi(\theta_{jl}) = 0 \tag{2.32}$$

Then, inside the ϵ-vicinity of the maximum, $\frac{p_j}{k_{gj}} > \frac{\alpha_j}{2\epsilon}$ and outside the ϵ-vicinity, $\frac{p_j}{k_{gj}} < \frac{\alpha_j}{2\epsilon}$ is satisfied.

In [64], it is shown that the convergence speed (rise time) to the optimum inside the ϵ-vicinity is faster with a smaller constant $k_{gj} \;\; j = 1, ..., n$ and a narrower ϵ-vicinity which is determined by smaller value $\frac{p_j}{k_{gj}}$ for $j = 1, 2, ..., n$.

Now assume that case 3 in Fig. 2.3 corresponds to the sliding mode $\sigma_{j-1}(t)$ which occurs outside the ϵ-vicinity. Let's define a new region with the distance ϵ_l^* and ϵ_r^* from left and right side of θ_j^*, respectively, where

$$\theta^*_{j(\epsilon_l^*,\epsilon_r^*)} = \{\theta_j | \theta_j^* - \epsilon_l^* \leq \theta_j \leq \theta_j^* + \epsilon_r^*\} \tag{2.33}$$

$$\epsilon^* > \epsilon \tag{2.34}$$

Moreover, assume that $\xi(\theta_j, t)$ is symmetrical and the system moves into the ϵ^*-vicinity from the left side. In the region between ϵ^* and ϵ-vicinities, $\frac{p_j}{k_{gj}} < \frac{\alpha_j}{2\epsilon}$. As in case 3, assume that $\theta_j(t)$ is inside the ϵ-vicinity. At $t - t_{01}$, $\theta_j(t)$ moves out of the ϵ-vicinity from the right side and reaches the next sliding mode $\sigma_{j-1} = 0$ at $t = t_1$. Thus

$$\theta_j^* - \epsilon < \theta_j(t_1) = \theta_j^* + \epsilon + k(t_1 - t_{01}) < \theta_j^* - \epsilon^* \tag{2.35}$$

$$\xi(\theta_j^* - \epsilon) < \xi(t_1) < \xi(\theta_j^* \pm \epsilon^*) \tag{2.36}$$

Since $\theta_j(t)$ is outside the ϵ-vicinity, $\sigma_{j-1}(t)\dot{\sigma}_{j-1}(t) < 0$ holds and $\xi(\theta_j)$ falls on the sliding surface $\sigma_{j-1}(t)$ which makes $\theta_j(t)$ move back to the ϵ-vicinity of θ_j^*. The above discussions can be summarized as follows:

Theorem : The multivariable sliding mode extremum seeking system with the sliding mode surfaces given by (2.2) and the optimizing control law given by (2.6) will stably converge to the maximum point from outside of the region $|\frac{\partial f}{\partial \theta_j}| \leq \frac{p_j}{k_{gj}}$ by switching among sliding modes $\boldsymbol{\sigma} = [m_1\alpha \;\; m_2\alpha \;\; ... \;\; m_n\alpha]$, if

$$\begin{cases} m_j = 2k & in \;\; region \;\; \frac{\partial f}{\partial \theta_j} > 0 \\ m_j = 2k+1 & in \;\; region \;\; \frac{\partial f}{\partial \theta_j} < 0 \quad k \in J \end{cases} \tag{2.37}$$

in which $m_j \in J \ \ (j = 1, 2, ..., n)$ where J is a set of integer numbers, and if

$$2\boldsymbol{\tau}\boldsymbol{p}^T \leq \sum_{1<j<n} \alpha_j \tag{2.38}$$

the system will enter the ϵ-vicinity of the maximum and converges to θ_j^* with oscillations. Now if

$$\frac{p_j}{k_{gj}} < \frac{\alpha_j}{2\epsilon} \tag{2.39}$$

$\theta_j(t)$ will move out of the ϵ-vicinity, oscillates within $y(\theta_j^*)$ and $y(\theta_j^* \pm \epsilon^*)$, goes on $\sigma_{j-1}(t)$ and moves back to the ϵ-vicinity of the maximum θ_j^*.

2.3 Conclusion

In this chapter, a multivariable sliding-mode extremum seeking controller is proposed by defining multiple sliding surfaces for the controller. Then, a rigorous study is conducted on the stability analysis and convergence of the proposed controller both outside and inside the ϵ-vicinity of the extremum point of the system. The resultant conclusions are summarized through a theorem at the end of the chapter. The performance of the proposed multivariable sliding-mode extremum seeking scheme will be further studied in control and optimization applications in the following chapters.

Chapter 3

MPPT IN AN ALTERNATOR-BASED ENERGY CONVERSION SYSTEM

One problem in the alternator energy conversion system is that the power-voltage curve has a sweat point at each speed. This causes obstacle for MPPT particularly when the load has a constant voltage. In other words, the maximum power cannot be achieved at various alternator speeds because the fixed output voltage may not be matched to the alternator characteristics at certain speeds. In this chapter, the proposed multivariable sliding-mode ESC presented in chapter 2 is proposed for MPPT in a Lundell alternator when the switched-mode rectifier (SMR) load-matching technique is applied. This application involves extremum seeking with two parameters to be controlled for power maximization; namely, the alternator's field current and its output load voltage. Experimental results are presented, which demonstrate that the controller can achieve accurate and robust power maximization.

The organization of this chapter is as follows. In section 3.1, the alternator electrical behaviour is studied. In this section, the alternator power-voltage diagrams at various operating speeds are presented. Then, the function of the alternator output power as well as its relationship to the control parameters are derived. In section 3.2, the efficiency of the proposed controller for MPPT in the alternator system is investigated. First, the laboratory-scale setup and its different parts are presented. Then, the performance of the proposed controller is compared with a gradient-based ESC both in steady state and transient conditions. Conclusions are presented in Section 3.3.

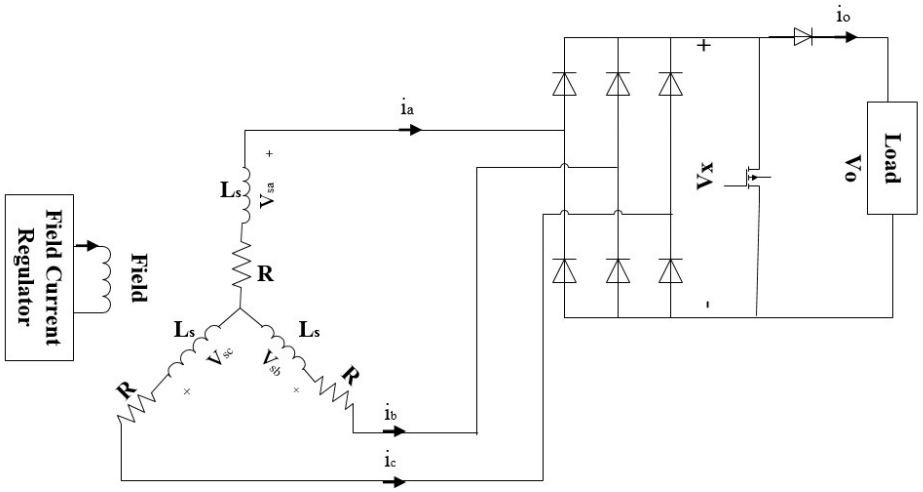

Figure 3.1: A simple schematic of the alternator circuit with a full-bridge rectifier.

3.1 Alternator Electrical Behaviour

Fig. 3.1 shows a simple schematic diagram of an alternator electrical model. The alternator is a 3-phase synchronous generator followed by a full-bridge rectifier. In the alternator circuit, the field current regulator applies a pulse-width modulated voltage across the field windings to produce the field current i_f. The rotor magnetic field, produced from the dc field current i_f, passes through the 3-phase windings of the stator, and generates inductive voltages of v_{as}, v_{bs} and v_{cs} as follows

$$v_{as} = K_a \omega_s i_f cos(\omega_s t) \tag{3.1}$$

$$v_{bs} = K_a \omega_s i_f cos(\omega_s t - \frac{2\pi}{3}) \tag{3.2}$$

$$v_{cs} = K_a \omega_s i_f cos(\omega_s t + \frac{2\pi}{3}) \tag{3.3}$$

where K_a is a constant and is called the motor constant and ω_s is the electrical frequency which is proportional to the alternator mechanical speed ω_m and the number of machine poles ρ ($\omega_s = \frac{\rho}{2}\omega_m$). Moreover, the magnitude of the inductive voltages is proportional to the field current i_f and the alternator mechanical speed ω_m which is given by $V_s = K_a \omega_m i_f$ [75].

Utilizing (3.1)-(3.3), and assuming that a resistive load R across the alternator, the phase currents can be expressed as,

$$i_{as} = K_a \frac{\rho}{2R} \omega_m i_f cos(\omega_s t) = i_l cos(\omega_s t) \tag{3.4}$$

$$i_{bs} = K_a \frac{\rho}{2R} \omega_m i_f cos(\omega_s t - \frac{2\pi}{3}) = i_l cos(\omega_s t - \frac{2\pi}{3}) \tag{3.5}$$

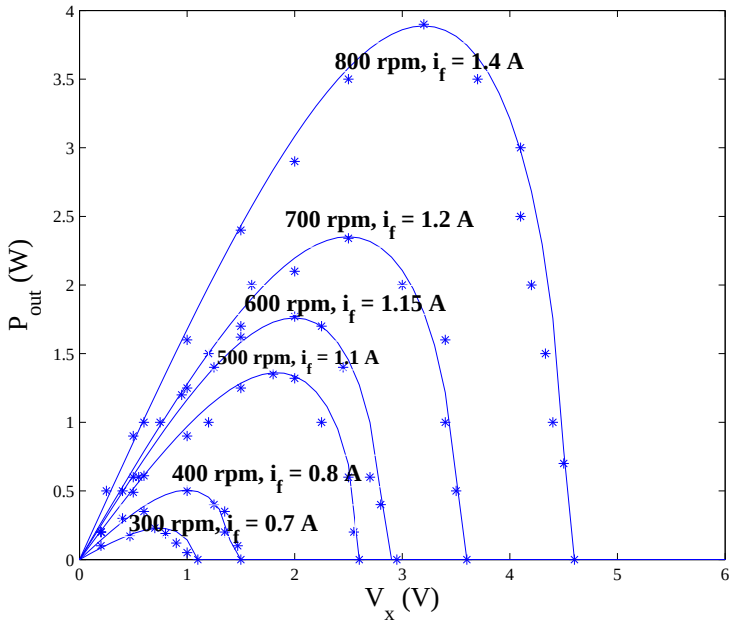

Figure 3.2: 2D alternator operating loci (Solid lines refers to simulation results and the stars show the experimental results).

$$i_{bs} = K_a \frac{\rho}{2R} \omega_m i_f cos(\omega_s t + \frac{2\pi}{3}) = i_l cos(\omega_s t + \frac{2\pi}{3}) \tag{3.6}$$

where $i_l = K_a \frac{\rho}{2R} \omega_m i_f$ is the amplitude of the load current. The AC voltage generated by the alternator passes through the full-bridge rectifier and generates a DC voltage V_x which makes the input voltage to DC/DC boost converter [66], [85].

For alternator MPPT under variable speed, one has to study the relationship between the output power versus alternator parameters. Considering the alternator output current which is obtained based on Fourier series analysis of the signals in the system, [9]

$$i_{out} = \frac{3}{\pi} \frac{\sqrt{v_s^2 - (\frac{2V_o}{\pi})^2}}{\omega_s L_s} \tag{3.7}$$

in which V_o is the load voltage, then the available power in the alternator system would be [9]

$$P_{out} = \frac{3V_o}{\pi} \frac{\sqrt{v_s^2 - (\frac{2V_o}{\pi})^2}}{\omega_s L_s} \tag{3.8}$$

where L_s is the self-inductance of stator windings and $V_s = k\omega i_f$ where ω is the alternator electrical speed.

Fig. 3.2 shows a two-dimensional alternator operating loci in simulation (solid line) and experiment (star). As shown, for any given speed, there exists a specific voltage for which the output power becomes maximum. If the load voltage is fixed, the maximum power cannot be achieved at various alternator speeds, because the fixed output voltage may not be matched to the alternator characteristics. To overcome this issue, a load-matching technique is applied to the alternator system. Thus, a power electronic DC/DC boost converter is utilized to act as a virtual controllable DC load at the alternator output terminals (see Fig. 3.1).

The boost converter allows higher levels of power to be achieved by boosting up the alternator output voltage V_x to the desired load voltage V_o. As long as the boost converter operates in the continuous conduction mode (CCM) and the PWM frequency is much higher than the bandwidth of the control loop, its input-output relationship is as follows

$$V_x = (1 - d)V_o \tag{3.9}$$

where d is the duty ratio of the boost converter and is controlled by the MOSFET switch of the boost converter. The load-matched operation is easily achieved by choosing the complement of the duty ratio (d') as follows [65]

$$d' = 1 - d = (\frac{\sqrt{2}\pi k_a}{4Vo})i_f\omega_s \tag{3.10}$$

Fig. 3.3 illustrates the 3D relationship of the alternator field current and output voltage versus the output power. As can be seen, at each speed there is a field current and output voltage for which the output power becomes maximum. In this application, the goal is to deliver maximum power to the load by controlling the load-matching operation and consequently by regulating the output voltage of the alternator. Considering (3.10), the above objective is achieved by controlling the field current and duty ratio as a function of output voltage and alternator speed [66].

3.2 Experimental Results

3.2.1 Setup Description

Fig. 3.4 shows the experimental setup used in this project. This system is a laboratory-scale emulation for an application in railway industry where an instrumented railcar (e.g., responsible for friction management) is to be powered using an alternator system that is connected to the railcar's wheel using a pulley

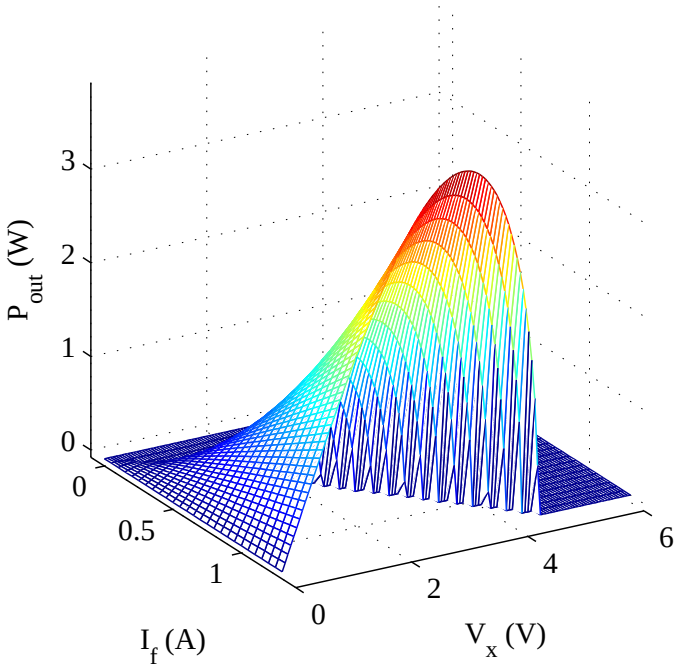

Figure 3.3: 3D alternator operating loci.

mechanism. The alternator is used to charge a battery (constant voltage load) which is utilized to provide power to several instruments aboard the railcar. A main objective is to achieve maximum power transfer to the battery at different travelling speeds of the train. As shown in Fig. 3.5, a load with constant voltage is applied which can be interpreted as a battery with a fixed voltage.

In the setup, instead of the train wheel, a MaxMotion Permanent Magnet DC Motor MM5090FC is utilized to rotate an ACDelco 334-2224A remanufactured alternator . The motor rotation is transferred to the alternator via a timing belt. The alternator rotational speed ω is considered nearly twice the motor rotational speed Ω (based on the equality of forces at both sides $R\Omega = r\omega$ and $r = \frac{1}{2}R$).

Fig. 3.6 illustrates the real-time control structure of the setup. In the setup, the DC load is an NHR 4700 which can be programmed to maintain the desired constant voltage load. The DC voltage of load is set at $6V$. The objective is to deliver maximum power to the load by controlling the alternator output voltage V_x and the field current I_f. The input to the multivariable sliding-mode ESC is the alternator output power P_{alt} which is obtained by using $P_{alt} = V_x I_x$. The calculated alternator output power is sent to the controller via a dSPACE DS1103 real-time controller board. Since ADC terminals of the dSPACE only measure the voltage, a small resistance $R_x = 0.1\Omega$ is added in series with the

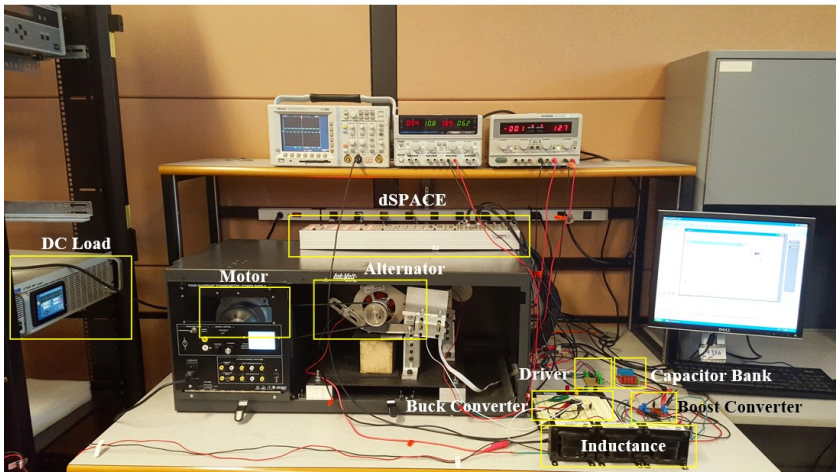

Figure 3.4: Experimental implementation of the proposed multivariable sliding-mode ESC on the motor-alternator setup.

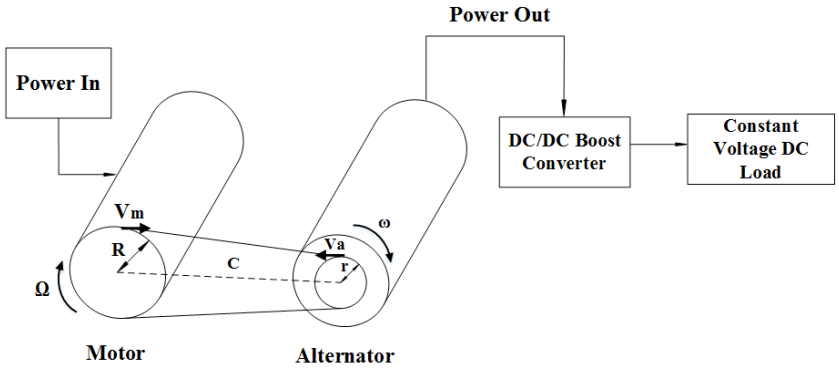

Figure 3.5: A simple schematic of motor-alternator setup.

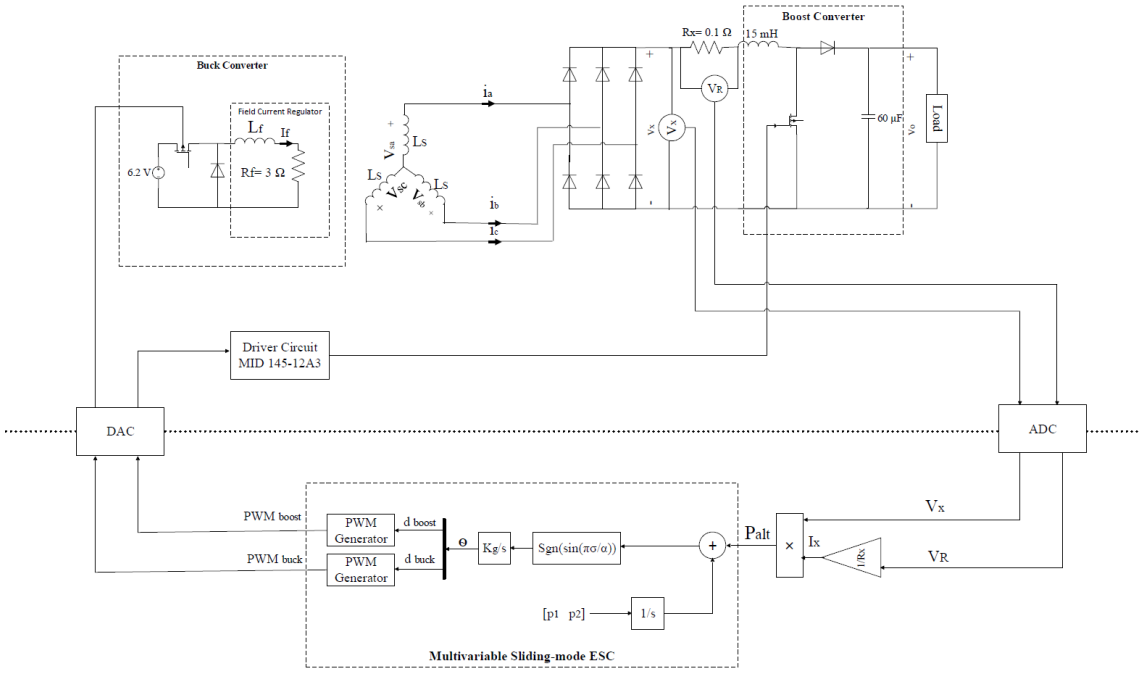

Figure 3.6: Real-time control structure of the setup using dSPACE control board.

alternator output and the voltage across the resistance is measured (V_R). Hence, I_x can be easily obtained from $I_x = V_R/R_x$. Also, the alternator output voltage V_x is measured by directly connecting the ADC terminal to the alternator output terminals.

In the proposed approach, controlling V_x and I_f is done by calculating proper values for the duty cycle of the DC/DC boost converter (d_{boost}) as well as the duty cycle of the DC/DC buck converter (d_{buck}). As mentioned earlier, since the DAC terminals of dSPACE can only send voltages to the analogue part, I_f cannot be controlled directly. A DC/DC buck converter is applied to the alternator field terminals and the output of buck converter provides proper field voltage. Since $V_f = R_f i_f$, by adjusting the value of V_f, i_f can be adjusted accordingly. Thus,

$$d_{buck} = \frac{V_o}{V_i} \tag{3.11}$$

where V_i is the voltage of power supply and has the value of $V_i = 6.2V$. Also, $V_o = R_f I_f$. The internal resistance of the alternator field is $R_f = 3\Omega$.

In the output of the controller, the adjusted buck and boost duty cycles are PWM modulated and the PWM signals are fed to the setup via a Digital to Analogue Converter (DAC) of the dSPACE board.

In the experiment, a MOSFET switch with an ON voltage of $13V$ is used in the DC/DC boost converter. Since, the maximum allowable output voltage

Table 3.1: Experimental Parameters of the Setup

Parameter	Value
Alternator nominal output amperage	$65A$
Alternator nominal output voltage	$12V$
Alternator nominal shaft speed	$1500rpm$
Motor nominal speed	$1750rpm$
Nominal DC voltage of motor armature	$90V$
Motor full load amperage	$5.2A$
Motor nominal torque	$2.034N.m$
R_f	$\simeq 3\ \Omega$
L_s	15 mH
DC constant load voltage	6V
$f_{sampling}$	100 kHz
$f_{switching-boost}$	10 kHz
$f_{switching-buck}$	1 kHz

of the dSPACE DAC/ADC terminals is $\pm 10V$, a driver is needed to drive the high power switch of the DC/DC boost converter. Moreover, to ensure that the buck and boost converters operate in CCM, the converter switching frequency and the controller sampling frequency should be adjusted appropriately, which is achieved by choosing $f_{switching} \ll f_{sampling}$ (at least 10 times smaller). Table I shows the important parameters for this implementation.

3.2.2 Results

Fig. 3.7 shows the control block diagram of the alternator system using the proposed multivariable sliding-mode controller. Here, p is a 1×2 vector and two sliding surfaces are considered. The gradient vector is derived by obtaining the error σ and feeding it to the block of $sgn(sin(\pi(.)/\alpha))$. Thus, the controlled parameters are given by $\theta = [d_{boost}, d_{buck}]$. The duty cycle d_{boost} is fed to the DC/DC boost converter and alternator output voltage V_x is adjusted . Furthermore, d_{buck} is fed to the buck converter and accordingly the alternator field current i_f is adjusted which determines the 3-phase alternator voltages. In the application described, what is important to be maximized is the average steady-state power of the system and not the instantaneous power. To this end, the

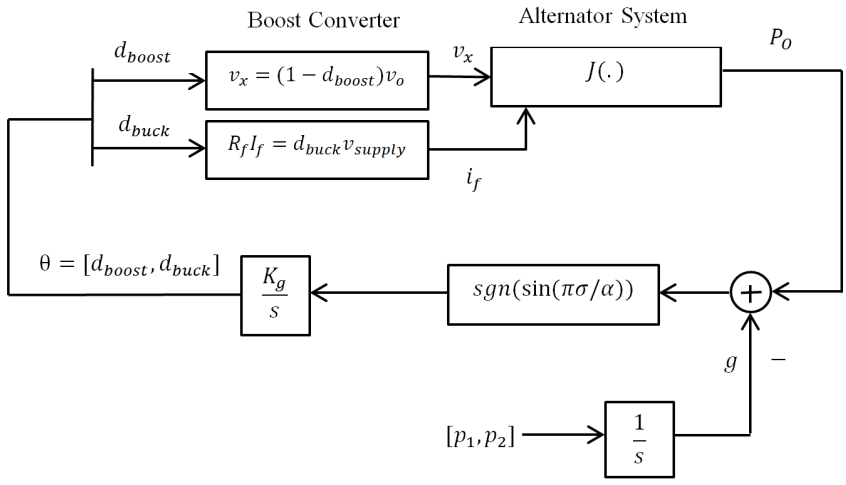

Figure 3.7: Alternator control block diagram using the proposed controller.

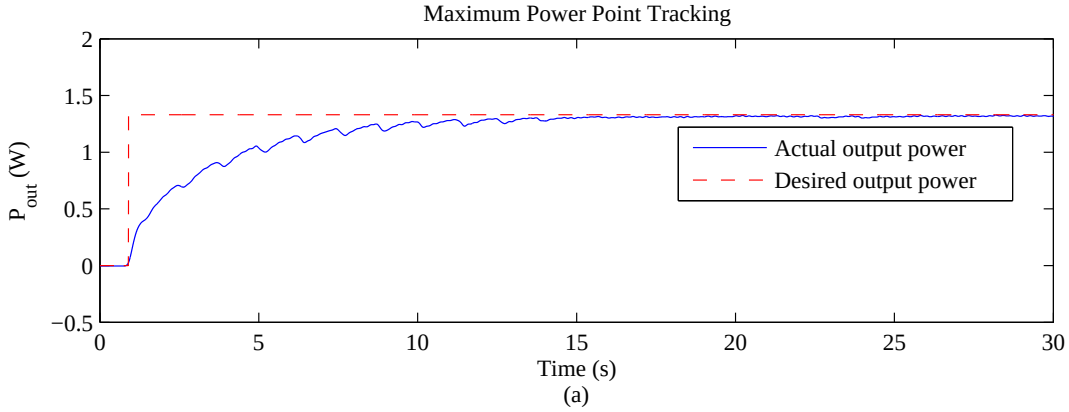

(a)

average values for the duty cycles of the boost and buck converters are tuned using the proposed extremum seeking algorithm. Since the mechanical dynamics of the system are much slower than the electrical dynamics, and also the electrical system is stable, the transient response in the maximization process can be safely neglected .

Steady State and Transient Tracking Performance

The proposed controller is built in the MATLAB/SIMULINK environment with a sampling period of $t_s = 10^{-5}s$ and its performance is studied using the *dSPACE Control Desk 3.7.3*. Fig. 3.8 and 3.9 show the experimental results when the proposed controller and the multivariable gradient-based ESC are applied to the setup system and the alternator operates at 500 rpm (in which maximum output power is $1.3W$ for $V_x \simeq 1.5V$, $i_f = 1.1A$, $d_{boost} \simeq 38\%$ and $d_{buck} \simeq 53\%$). As the motor starts to rotate, the power increases until it reaches the maximum value.

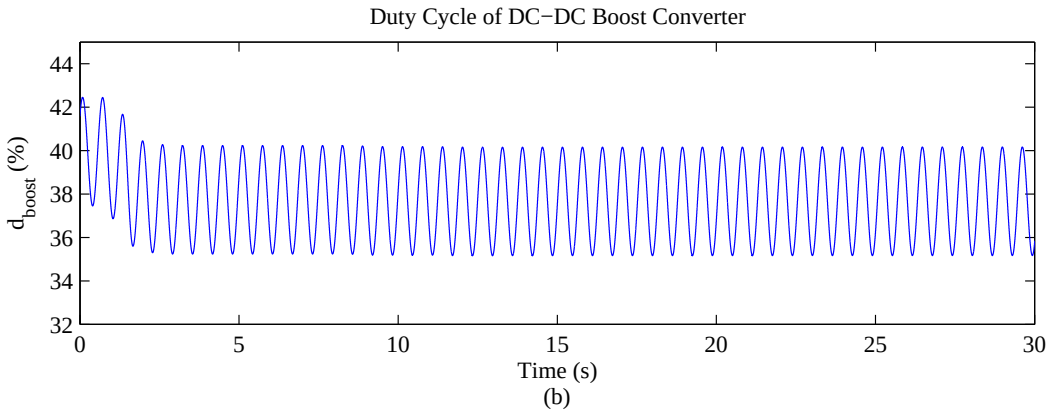

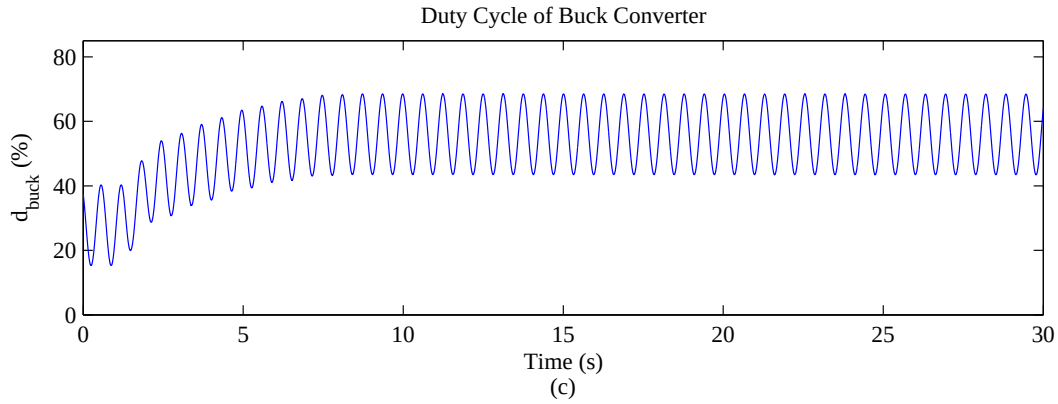

Figure 3.8: Experimental results for (a) alternator output power, (b) d_{boost}, and (c) d_{buck} when the multivariable gradient-based extremum seeking controller is applied to the alternator system at 500rpm.

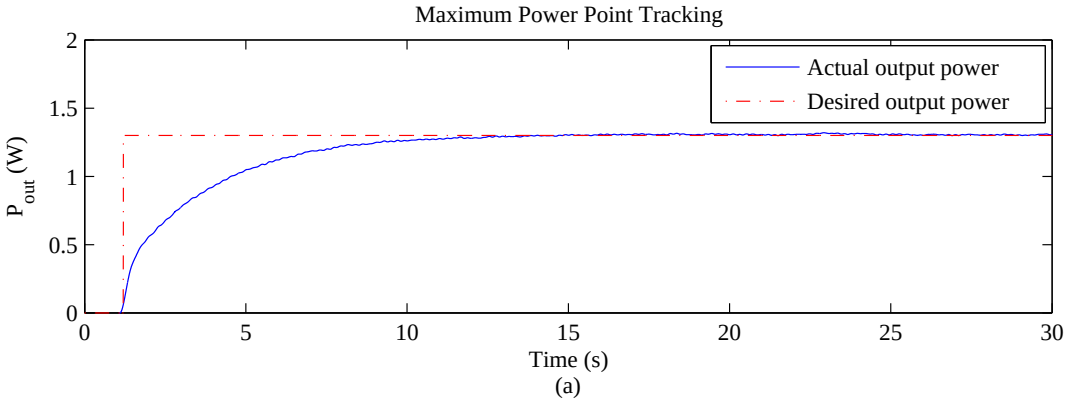

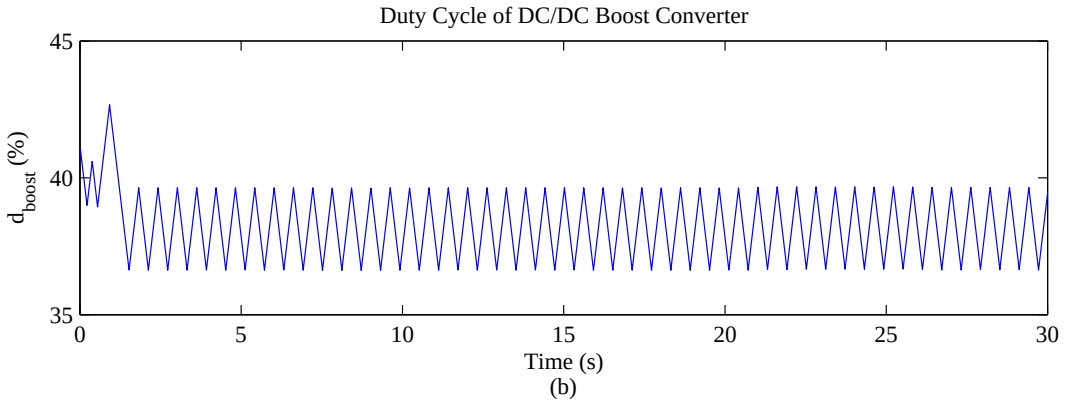

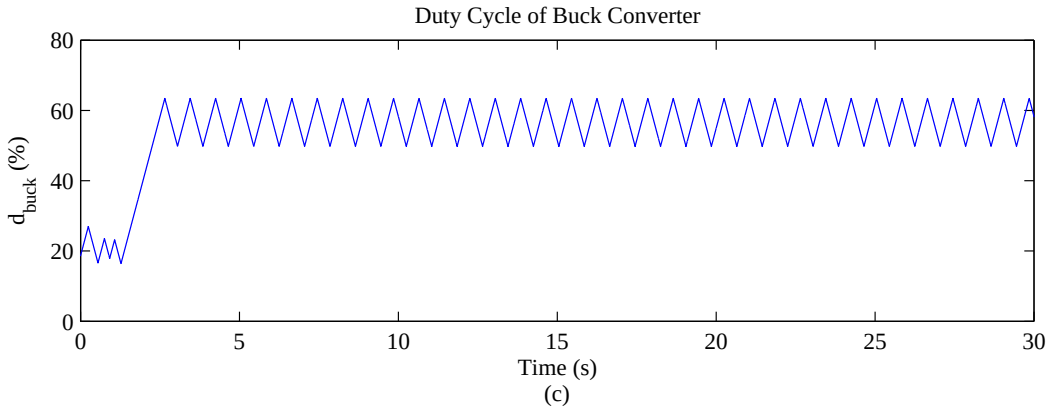

Figure 3.9: Experimental results for (a) alternator output power, (b) d_{boost}, and (c) d_{buck} when the proposed multivariable sliding-mode extremum seeking controller is applied to the alternator system at 500rpm.

Comparing the results of the two controllers, it can be seen that the proposed controller can track maximum output power more smoothly. This is specifically evident in the beginning of operation, where the multivariable gradient-based ESC method results in small oscillations. Moreover, the convergence speed of the proposed controller is higher than the other controller.

To further study the efficiency of the proposed controller, a disturbance is added to the alternator and the controller performance is investigated under transient conditions. Fig. 3.10 and 3.11 show the experimental results for the two controllers when the alternator speed changes from 300 rpm to 500 rpm at about $t = 24s$. Based on Fig. 3.2, the desired maximum output power should change from $P_{outmax} = 0.25W$ to $P_{outmax} = 1.3W$. Also, the boost and buck duty cycles and field current should change from $d_{boost} \simeq 40\%$ to $d_{boost} \simeq 38\%$, $d_{buck} \simeq 35\%$ to $d_{buck} \simeq 53\%$ and $i_f = 0.7A$ to $i_f = 1.1A$, respectively.

As demonstrated in Fig. 3.11, the proposed controller reaches a smooth steady state response in less than 5 seconds. However, the MPPT result in Fig. 3.10 illustrates that after the speed changes, the response of multivariable gradient-based ESC oscillates and reaches the steady-state in about 10 seconds. One point which can be observed in all the figures is that the power convergence speed for both controllers is relatively high. This delay is the time period for the motor to get to the adjusted speed, whether there is a controller or not, and cannot be considered as a disadvantage of the proposed controller.

Control Parameters Selection

Appropriate parameter selection increases the controller efficiency. The stability and convergence analysis presented in Chapter 2, provides a systematic guideline for selecting control parameters in multivariable sliding-mode ESC. As k_{g_i} increases, the sliding-mode existence region becomes smaller and the convergence speed increases. However, increasing k_{g_i} results in increasing p_i if it is desired that the sliding-mode region remains large enough [97]. On the other hand, fast convergence speed compromises the steady state performance. According to [97], the amplitude of the steady state oscillation of the system is governed by

$$m_i = \int_0^{\alpha_i/p_i} k_{g_i} dt = k_{g_i}\alpha_i/p_i \quad i = 1, ..., n \tag{3.12}$$

Considering (3.12), as k_{g_i} increases, the amplitude of the steady state oscillations would increase. In the experiments, K_g and P are selected as $K_g = [7.5\ \ 0;\ 0\ \ 5]$, and $P = [0.2\ \ 0.5]$.

Moreover, based on (3.12) , it is desirable to keep α_i as small as possible. In general, increasing α results in steady state oscillations with higher amplitudes.

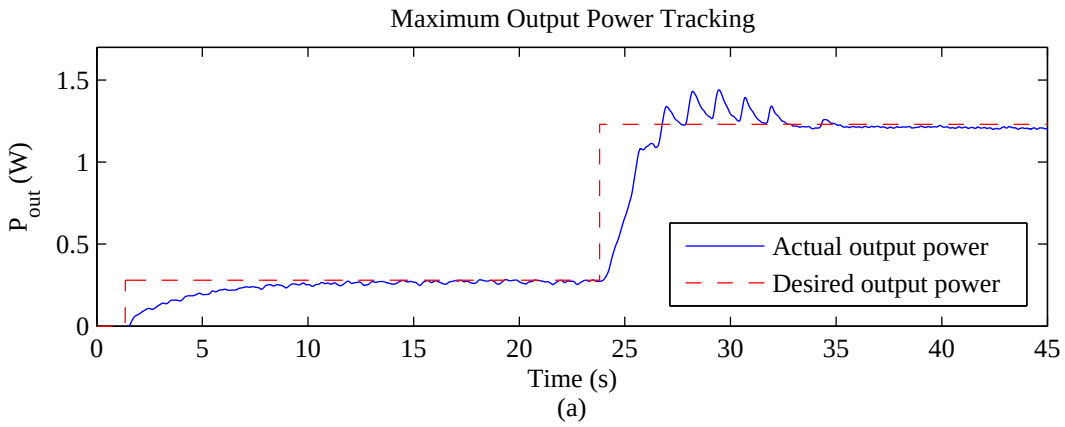

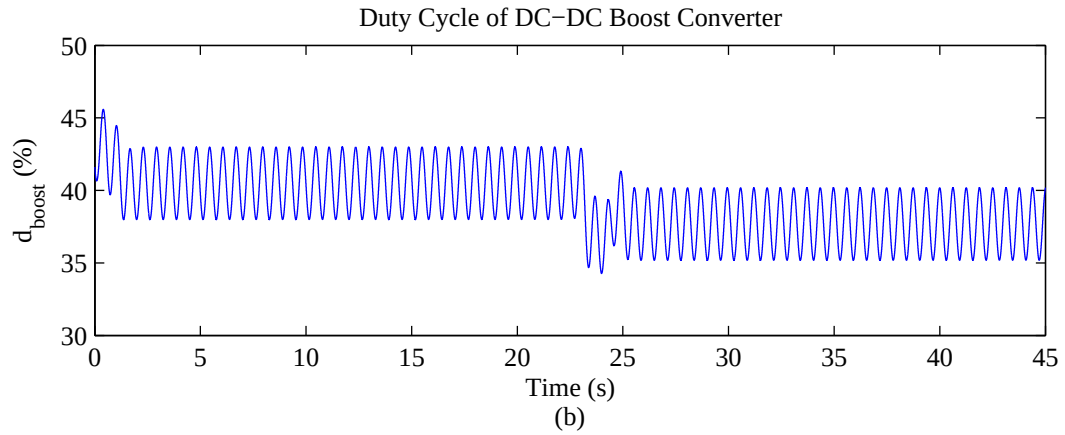

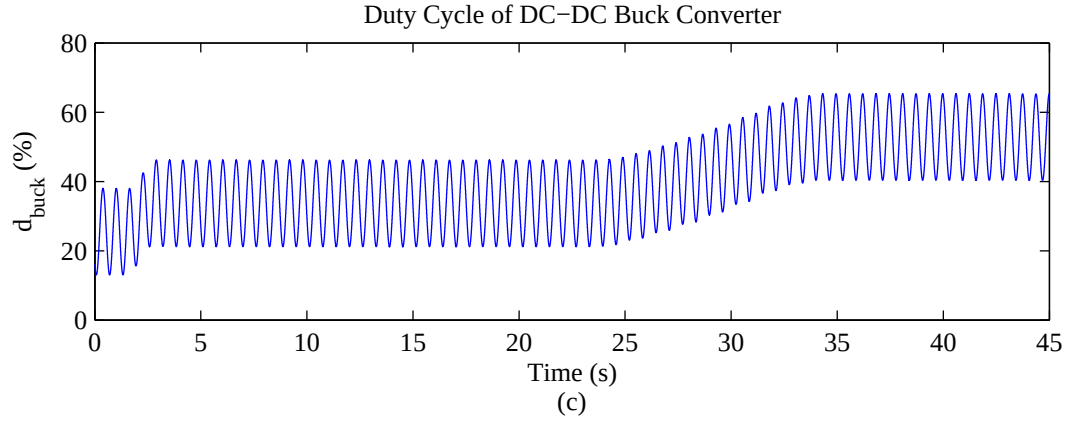

Figure 3.10: Transient experimental results for (a) alternator output power, (b) d_{boost}, and (c) d_{buck} when the multivariable gradient-based extremum seeking controller is applied to the alternator system and the speed changes from 300 to 500rpm at 24s.

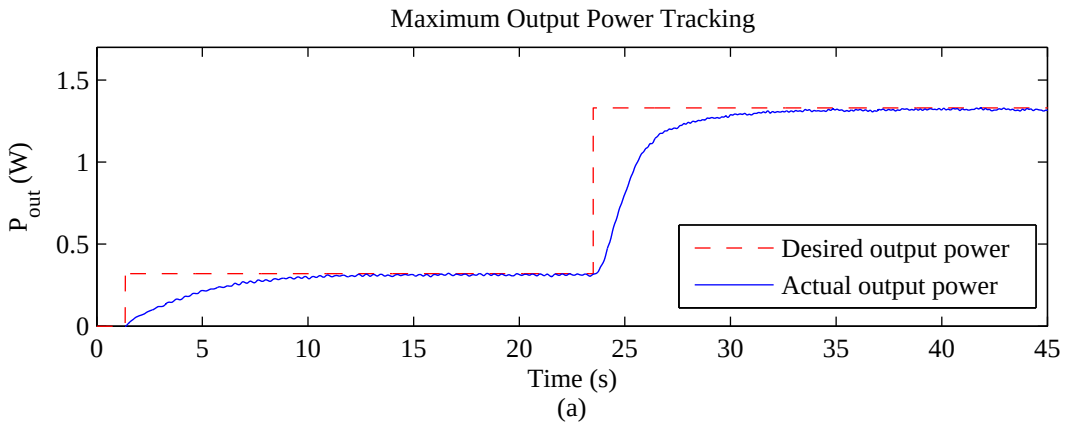

(a)

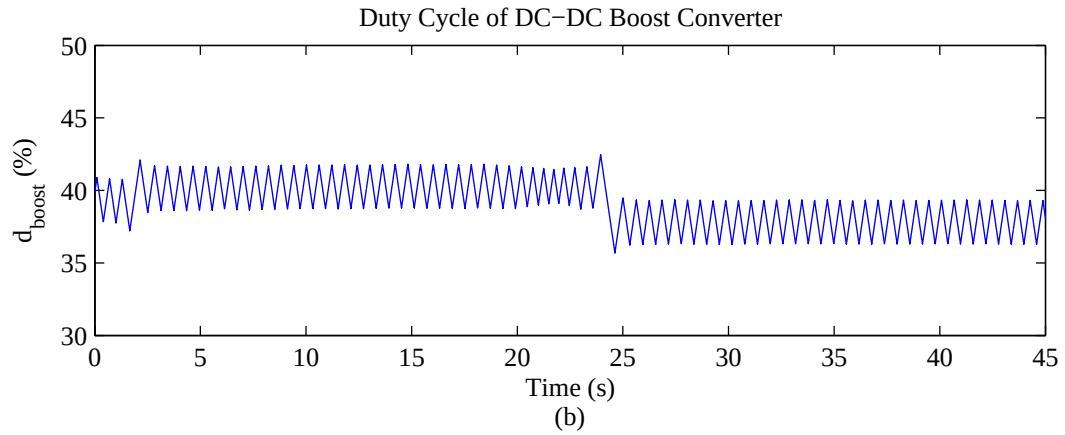

(b)

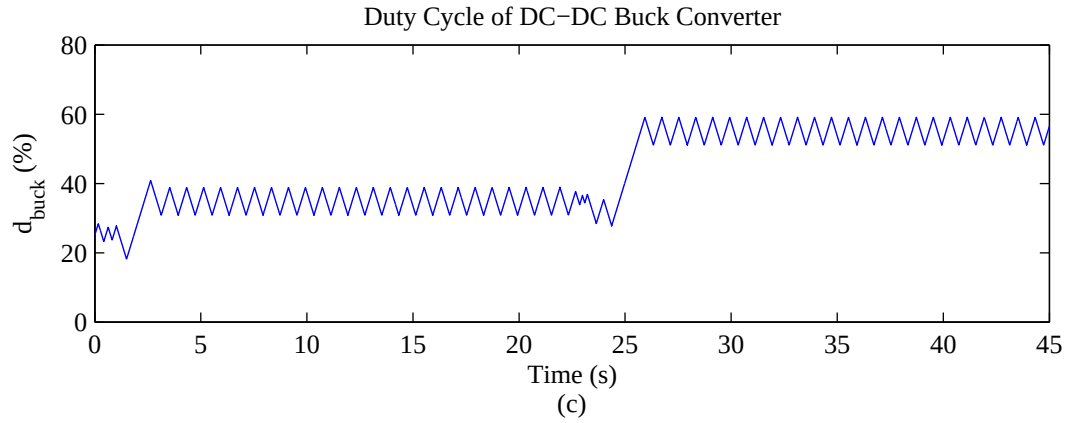

(c)

Figure 3.11: Transient experimental results for (a) alternator output power, (b) d_{boost}, and (c) d_{buck} when the proposed multivariable sliding-mode extremum seeking controller is applied to the alternator system and the speed changes from 300 to 500rpm at 24s.

Table 3.2: MPP Tracking Efficiency Comparison for Two Controllers in Experiment

	Controller	$\eta(\%)$
Steady State	Multivariable gradient-based ESC	87
	Multivariable sliding-mode ESC	90
Transient	Multivariable gradient-based ESC	78
	Multivariable sliding-mode ESC	85

This fact is validated through the experiments. As the parameters, $\alpha_i's$ are chosen to be very small, the output power will be smooth. However, by choosing $\alpha_i's$ very small, there will be no change in duty cycle as the alternator speed varies. Thus the algorithm cannot converge to the desired maximum power. Hence, $\alpha_i's$ cannot be selected to be very small. According to the convergence analysis in Chapter 2, a condition is presented in which the lower bound for α_i is restricted to guarantee convergence of the system in finite time: $2\boldsymbol{\tau p}^T \leq \sum_{1<i<n} \alpha_i$. In the experiments, the dynamic time delays are obtained as $\boldsymbol{\tau} = [\tau_1 \ \ \tau_2] = [1 \ \ 1.5]$. Hence, the inequality of $\alpha_1 + \alpha_2 > 1.9$ should be satisfied when choosing α_1 and α_2. Here, we selected the vector of $\alpha_i's$ as $[\alpha_1, \ \ \alpha_2] = [0.5, \ \ 1.5]$.

Designing appropriate values for the magnitudes of perturbation signals in multivariable gradient-based ESC is very important. The experiments show that small magnitudes of the perturbation signals lead to smooth output power. However, there is no change in the duty cycle as the alternator speed varies (since it cannot converge to the next desired maximum power). In contrast, as the amplitude of perturbation signals increases, the duty cycle variations increase while the output power profile becomes less smooth. Thus, a compromise should be made between the output power smoothness and the duty cycle variations. In the experiments, the amplitudes of the sine waveforms are set as $[A_1 \ \ A_2] = [0.01 \ \ 0.02]$, for the adding perturbation signals; and $[A_1 \ \ A_2] = [1 \ \ 0.5]$, for the multiplying perturbation signals. This helps to explain why the duty cycle changes are gradual in the experimental results of Fig. 3.8 and 3.10, when compared to the results for the proposed controller. Moreover, K_g and perturbation frequencies are selected as $K_g = [4 \ \ 0; 0 \ \ 2.5]$ and $[\omega_1 \ \ \omega_2] = [15 \ \ 10]$ for adding perturbation signal and $[\omega_1 \ \ \omega_2] = [5 \ \ 10]$ for multiplying perturbation signal. In [90] and [22], parameter selection in multivariable gradient-based ESC is fully discussed.

MPP Tracking Efficiency Comparison

For further comparison, consider the MPPT efficiency of two controllers. Let us use the criteria based on the following equation [15, 29]

$$\eta = \frac{\int_0^t P_{inst}(t).dt}{\int_0^t P_{MPP}(t).dt} \tag{3.13}$$

where P_{inst} is the instantaneous power using the MPPT controller with P_{MPP} being the expected maximum output power. From (3.13), it can be inferred that the tracking efficiency is the fractional relationship between two areas under the real and the expected maximum output power curves. The closer the real curve to the expected curve, the better the tracking efficiency [15]. The MPPT efficiency results for the steady state and the transient cases are presented in Table 3.2, which indicate that higher efficiency can be obtained for the proposed ESC method.

3.3 Conclusion

In this chapter, a novel multivariable sliding-mode extremum seeking controller is presented and used for MPPT in an alternator-based energy conversion system. The objective is to track the maximum power by controlling the alternator field current and output voltage. The experimental results demonstrate the efficiency of the proposed controller in achieving fast and smooth convergence with higher tracking accuracy when compared with the multivariable gradient-based ESC method. Moreover, a study is performed on disturbance rejection of the proposed controller. It is shown that the proposed controller can handle the disturbances better and faster in face of speed variations.

Chapter 4

Extremum Seeking PI Tuning for PMSM Current Regulation

Although PI controllers are widely used in industry, their effectiveness is often limited due to poor tuning. In this chapter, the application of extremum seeking method as an optimizer for tuning the PI gains is studied. To this end, a multivariable sliding-mode extremum seeking (MSES) PI tuning method is proposed and applied for current regulation in a brushless PMSM. The MSES tuning method utilizes extremum seeking as a real-time optimizer to adjust PI gains such that the effect of disturbances on the system is minimized. This is achieved through minimization of a cost function which characterizes the desired performance of the system. The stability of the proposed control strategy is investigated through a Lyapunov analysis and its performance is evaluated through experimental studies.

This chapter is organized as follows. In section 4.1, the proposed adaptive PI controller is introduced and its stability is investigated using the Lyapunov method. In section 4.2, the proposed scheme is applied for online tuning of a PI controller to regulate the shaft torque of a brushless PMSM. Furthermore, an algorithm for rotor position estimation is presented in this section. In section 4.3, performance of the proposed controller is investigated through several tests and compared with a conventional PI and a recently proposed PI controller using gradient-based extremum seeking tuning method. Finally, conclusions are presented in section 4.4.

4.1 Multivariable Sliding-Mode PI Tuning

4.1.1 Controller Design

Consider a general nonlinear plant as follows

$$y = f(u, t) \tag{4.1}$$

where $f : \mathbb{R} \to \mathbb{R}$, $y \in \mathbb{R}$ is the output and u is the input of the system. Let us assume that the following PI controller is used such that the plant output $y(t)$ follows the desired output $y_d(t)$

$$u(e, \boldsymbol{\theta}) = K_p e(t) + K_I \int_0^t e(\tau) d\tau \tag{4.2}$$

where K_p and K_I are the proportional and integral gains, respectively, and $e(t)$ is the tracking error defined as

$$e(t) = y_d(t) - y(t). \tag{4.3}$$

Let us define $\boldsymbol{\theta} = [K_P \;\; K_I]^T$ and $\Gamma(e) = [e(t) \;\; \int_0^t e_i(\tau) d\tau]^T$. Hence (4.2) can be written as

$$u(e, \boldsymbol{\theta}) = \Gamma^T(e)\boldsymbol{\theta}. \tag{4.4}$$

Assume that there exists an ideal PI controller u^* with optimal gain vector $\boldsymbol{\theta^*} = [K_P^* \;\; K_I^*]^T$ as follows

$$u^*(e, \boldsymbol{\theta^*}) = \Gamma^T(e)\boldsymbol{\theta^*}. \tag{4.5}$$

The goal is to design an adaptive law for PI gains such that the tracking error $e(t)$ converges to zero as $t \to 0$. In this case, the PI controller u approximates the ideal unknown u^* such that the error $e_u = u^* - u$ converges to zero as $t \to 0$. Considering (4.4) and (4.5), e_u can be written as

$$e_u = \Gamma^T(e)\tilde{\boldsymbol{\theta}} \tag{4.6}$$

where $\tilde{\boldsymbol{\theta}} = \boldsymbol{\theta^*} - \boldsymbol{\theta}$ is the gain estimation error.

In what follows, the MSES method is utilized as an optimizer to tune the PI gains K_P and K_I through an adaptive law such that optimal closed-loop performance control can be achieved. To this end, we use the following Integral Squared Error (ISE) as a universal cost function when using the extremum seeking approach

$$J(\boldsymbol{\theta}) = \frac{1}{T} \int_0^T e^2(t) dt. \tag{4.7}$$

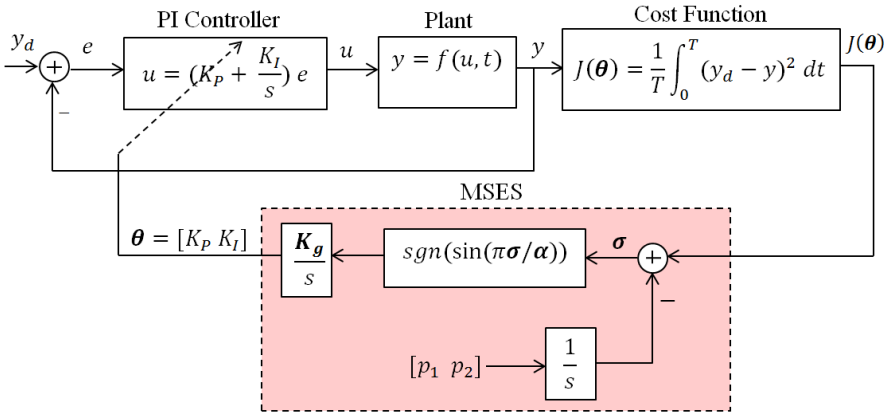

Figure 4.1: Block diagram of the proposed extremum-seeking PI tuning controller.

The multivariable extremum seeking algorithm varies the input vector $\boldsymbol{\theta}$ such that $J(\boldsymbol{\theta})$ reaches the minimum point.

Fig. 4.1 illustrates the overall proposed MSES PI tuning method. The proposed scheme utilizes two sliding surfaces σ_1 and σ_2 to optimize parameters K_P and K_I of the PI controller. Hence, the vector of sliding surfaces is defined as

$$\boldsymbol{\sigma(t)} = [\sigma_1\ \ \sigma_2] \tag{4.8}$$

where $\sigma_i = J - p_i t$ such that $p_i < 0 \quad (i = 1, 2)$ is the slope of i^{th} sliding surface. The vector of driving signals is defined as

$$\boldsymbol{p} = [p_1\ \ p_2]. \tag{4.9}$$

The optimizing control law is set as follows

$$\dot{\boldsymbol{\theta}} = K_g sgn(sin(\frac{\boldsymbol{\pi\sigma}}{\boldsymbol{\alpha}})) \tag{4.10}$$

where $sgn(.)$ is a 2×1 signum vector, $\boldsymbol{\alpha} = [\alpha_1\ \ \alpha_2]^T$ is a 2×1 vector for which each element is a positive constant, and $K_g = diag([k_{g1}\ \ k_{g2}])$ is a 2×2 diagonal positive definite matrix which determines the convergence rate. ES achieves optimization by forcing J to remain on the decreasing sliding surface vector, i.e., $\boldsymbol{\sigma} \to 0$. Thus, the system moves towards the optimum vector $\boldsymbol{\theta}^* = [K_P^*\ \ K_I^*]^T$.

4.1.2 Stability Analysis

To analyze the tracking error convergence and stability of the closed-loop system, consider the following Lyapunov-like function

$$V = \frac{1}{2}\boldsymbol{\sigma}\boldsymbol{\sigma}^T + \frac{1}{2}{e_u}^2. \tag{4.11}$$

The time derivative of V with respect to time is given by

$$\begin{aligned}\dot{V} &= \dot{\boldsymbol{\sigma}}\boldsymbol{\sigma}^T + \dot{e_u}e_u = (\frac{\partial J}{\partial f}\frac{\partial f}{\partial u}\frac{\partial u}{\partial \boldsymbol{\theta}}\dot{\boldsymbol{\theta}} - \boldsymbol{p})\boldsymbol{\sigma}^T - (\frac{\partial e_u}{\partial u}\frac{\partial u}{\partial \boldsymbol{\theta}}\dot{\boldsymbol{\theta}})e_u^T \\ &= (-f\frac{\partial f}{\partial u}\boldsymbol{\Gamma^T}(e)K_g sgn(sin(\frac{\pi\boldsymbol{\sigma}}{\alpha})) - \boldsymbol{p})\boldsymbol{\sigma}^T - (\boldsymbol{\Gamma^T}(e)K_g sgn(sin(\frac{\pi\boldsymbol{\sigma}}{\alpha}))\boldsymbol{\Gamma^T}(e)\tilde{\boldsymbol{\theta}}.\end{aligned} \tag{4.12}$$

To guarantee stability of the system, $\dot{V}$ should be negative. After performing algebraic manipulations, (5.17) can be rewritten as

$$\dot{V} = \sum_{i=1,2}(-f\frac{\partial f}{\partial u}\Gamma_i(e)K_{gi}sgn(sin(\frac{\pi\sigma_i}{\alpha_i})) - p_i)\sigma_i - \sum_{i=1,2}(\Gamma_i(e))^2\sum_{i=1,2}K_{gi}sgn(sin(\frac{\pi\sigma_i}{\alpha_i}))\tilde{\theta}_i. \tag{4.13}$$

Then it is sufficient that each term of (4.13) be negative. In the sliding-mode existence region $|\frac{\partial J}{\partial \theta_i}| > |\frac{p_i}{K_{gi}}|$, we can further define the sliding manifold vector as

$$\boldsymbol{\sigma} = [m_1\alpha_1 \;\; m_2\alpha_2], \;\; m_i \in J, \;\; i = 1, 2. \tag{4.14}$$

If $(2k-1)\alpha_i < \sigma_i(0) < 2k\alpha_i$, then $sgn(sin(\frac{\pi\sigma_i}{\alpha_i})) = -1$, and (5.5) is simplified as

$$\dot{V} = \sum_{i=1,2} -(|\frac{\partial J}{\partial \theta_i}|K_{gi} + p_i)|\sigma_i| - \sum_{i=1,2}(\Gamma_i(e))^2\sum_{i=1,2}K_{gi}\tilde{\theta}_i \tag{4.15}$$

Considering the existence region $|\frac{\partial J}{\partial \theta_i}| > |\frac{p_i}{K_{gi}}|$, and for $\frac{\partial J}{\partial \theta_i} > 0$ and $\theta_i < \theta_i^*$, $\dot{V}$ is negative. In this case, σ_i is kept at the sliding manifold $\sigma_i = 2k\alpha_i$ while the PI gain θ_i is less than the optimal value. Now, assume that $\frac{\partial J}{\partial \theta_i} < 0$. If $2k\alpha_i < \sigma_i(0) < 2(k+1)\alpha_i$, then $sgn(sin(\frac{\pi\sigma_i}{\alpha_i}))) = 1$. With a similar inference, the same equation as (4.15) is obtained. Then, in the sliding-mode existence region $|\frac{\partial J}{\partial \theta_i}| > |\frac{p_i}{K_{gi}}|$, for $\frac{\partial J}{\partial \theta_i} < 0$ and $\theta_i^* < \theta_i$, one can conclude that $\dot{V} \leq 0$. In this case, σ_i is kept at the sliding manifold $\sigma_i = (2k+1)\alpha_i$, while the PI gains are greater than the optimal values.

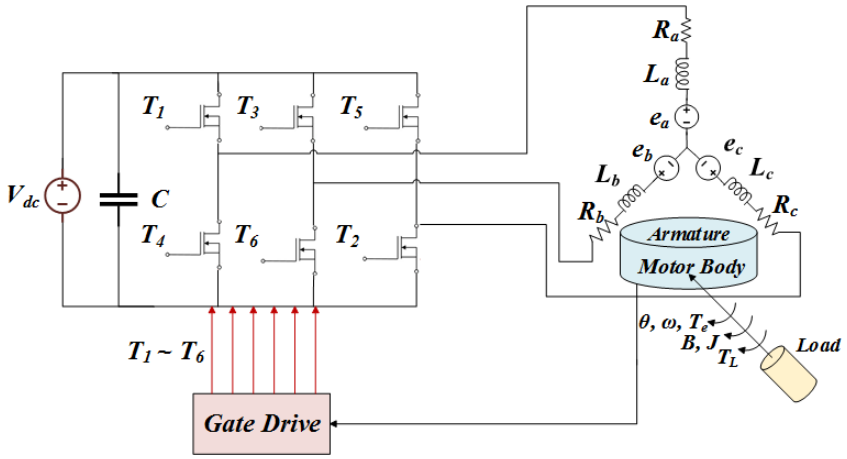

Figure 4.2: Permanent magnet synchronous motor and inverter circuitry.

4.2 Application to Current Regulation of Brushless PMSM

4.2.1 Problem Statement

Fig. 5.1 shows a typical three-phase closed-loop PMSM control circuit. The PMSM consists of an electrical and a mechanical subsystem. Assuming that the PMSM is a surface mounted type with star configuration, electrical equations of the motor for three phases are given by

$$\begin{aligned} v_{sa} &= i_{sa}R + L\frac{di_a}{dt} + e_a \\ v_{sb} &= i_{sb}R + L\frac{di_b}{dt} + e_b \\ v_{sc} &= i_{sc}R + L\frac{di_c}{dt} + e_c \end{aligned} \tag{4.16}$$

where v_{sa}, v_{sb} and v_{sc} are three phase stator voltages, i_{sa}, i_{sb} and i_{sc} are three phase stator currents, L is the inductance of each phase including the mutual inductance, and R is the resistance of stator windings in each phase.

The dynamic equation of PMSM is as follows

$$\begin{aligned} \frac{d\theta_m}{dt} &= \omega_m J\frac{d\omega_m}{dt} \\ &= T_m - T_L - B\omega_m \end{aligned} \tag{4.17}$$

where θ_m and ω_m are the PMSM mechanical angular position and velocity, respectively, J is the inertia, T_m is the electromagnetic torque, T_L is the load torque and B is the linear viscous friction coefficient.

The PMSM is connected to a three-phase bridge inverter and powered through six MOSFET switches of the inverter. The rotor position is detected using a position sensor such as an optical encoder or, in this study, Hall-effect sensors. The digital signals from the position sensors are used to determine the switching activity of the inverter [33]. The inverter switching should be controlled such that the desired electromagnetic torque is produced. The PMSM torque regulation is achieved by controlling the stator three phase currents.

The PMSM electromagnetic torque is given by [5, 76]

$$T = K_t[i_{sa}sin(\delta) + i_{sb}sin(\delta + \frac{2\pi}{3}) + i_{sc}sin(\delta - \frac{2\pi}{3})] \tag{4.18}$$

where i_{sa}, i_{sb} and i_{sc} are three phase sinusoidal currents, δ is the electrical angle of the shaft, and K_t is the torque constant which is a function of the rotor permanent magnetic flux λ_{pm} and number of poles ρ, i.e. $K_t = \frac{\rho}{2}\lambda_{pm}$.

Assume that the stator sinusoidal currents are

$$\begin{aligned} i_{sa} &= I_s sin(\sigma) \\ i_{sb} &= I_s sin(\sigma + \frac{2\pi}{3}) \\ i_{sb} &= I_s sin(\sigma - \frac{2\pi}{3}) \end{aligned} \tag{4.19}$$

where I_s is the amplitude of stator three-phase currents. Then (5.14) can be written as

$$T = K_t I_s[sin^2(\delta) + sin^2(\delta + \frac{2\pi}{3}) + sin^2(\delta - \frac{2\pi}{3})] \tag{4.20}$$

which can be further simplified as follows

$$T = \frac{3}{2}K_t I_s. \tag{4.21}$$

Based on (4.21), the brushless PMSM electromagnetic torque is proportional to the maximum amplitude of the stator current, i.e., $I_s \propto T_{shaft}$ [38]. Hence by controlling I_s, the PMSM shaft torque can be also adjusted.

4.2.2 Current Control using the Proposed MSES PI Tuning

Fig. 4.3 shows the block diagram of the proposed torque controller applied to brusless PMSM. The stator currents i_{sa}, i_{sb} and i_{sc} are sensed through current sensors and fed to the rectification block to obtain the maximum amplitude I_s for three phase currents. The *abc* to $\alpha\beta 0$ Clarke transformation is applied to

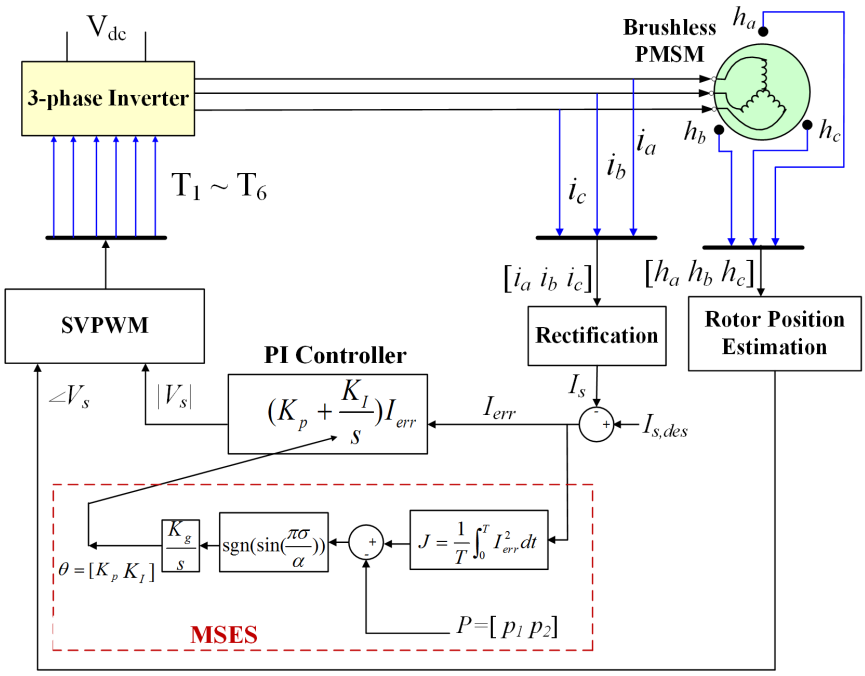

Figure 4.3: Block diagram of the proposed controller applied to a brushless PMSM.

three phase currents using [8]

$$\begin{bmatrix} i_\alpha \\ i_\beta \\ 0 \end{bmatrix} = \frac{2}{3} \begin{bmatrix} 1 & -\frac{1}{2} & -\frac{1}{2} \\ 0 & \frac{\sqrt{3}}{2} & -\frac{\sqrt{3}}{2} \\ \frac{1}{2} & \frac{1}{2} & \frac{1}{2} \end{bmatrix} \begin{bmatrix} i_{sa} \\ i_{sb} \\ i_{sc} \end{bmatrix}. \tag{4.22}$$

Hence i_α and i_β are obtained as follows

$$\begin{bmatrix} i_\alpha \\ i_\beta \\ 0 \end{bmatrix} = \begin{bmatrix} I_s sin(\omega t) \\ I_s cos(\omega t) \\ 0 \end{bmatrix}. \tag{4.23}$$

As shown in Fig. 4.3, the measured I_s is compared with the desired current $I_{s,des}$ which is proportional to the desired rotor torque. Thus the error I_{err} is obtained as follows

$$I_{err}(t, \boldsymbol{\theta}) = I_{s,des} - I_s \tag{4.24}$$

which is passed through a PI controller to generate the stator voltage magnitude. The PI control parameters are assumed to be tunable based on the error of the system using the the proposed multivariable sliding-mode extremum seeking tuning method.

Besides, the rotor angular position is measured using Hall-effect sensors. Since the rotor position obtained from Hall-effect sensors is discontinuous [78], an estimation algorithm is applied to the system to obtain the continuous rotor angle ϕ. To maximize the shaft torque, an angle of $\pi/2$ is considered between the rotor and stator magnetic fields. Then, the magnitude and angle of the generated stator voltage are passed to a space vector pulse width modulation (SVPWM) block to determine the switching sequence for the six switches of the inverter.

4.2.3 Rotor Position Estimation using Hall Effect Sensors

The discontinuous rotor position obtained from hall sensors results in non-sinusoidal phase currents. However, the PMSM produces sinusoidal electromotive force (emf) which should be supplied with sinusoidal phase currents to generate a constant torque [83]. To this end, the following rotor position estimation algorithm is applied to the system to generate the continuous rotor position.

Three Hall-effect sensors are usually pre-mounteded on PMSM rotors with a distance of 120 electrical degrees which detect the rotor position every 60 electrical degrees [70, 84]. Hence, six states can be considered for three Hall sensors as shown in Fig. 4.4. Based on these states, six sectors with $S = [0 \;\; \pi/3]$, $[\pi/3 \;\; 2\pi/3]$, $[2\pi/3 \;\; \pi]$, $[\pi \;\; 4\pi/3]$, $[4\pi/3 \;\; 5\pi/3]$, and $[5\pi/3 \;\; 2\pi]$ are defined which have the discrete values $y = 0, \pi/3, 2\pi/3, \pi, 4\pi/3, 5\pi/3$, and 2π, respectively.

Assume $\omega(t)$ is the instantaneous angular speed of the rotor which can be obtained as follows [13]

$$\omega(t) = \frac{y(t) - y(t - \Delta t)}{\Delta t} \quad \pi/4 \leq |y(t) - y(t - \Delta t)| \leq \pi/2 \tag{4.25}$$

where $y(t)$ is the value of rotor position in the current sector and Δt is the time difference between the current and the previous sector.

Calculating $\omega(t)$ for the case where rotor position changes from sector 6 (y= 2π) to sector 1 (y= $\pi/3$) of the next cycle (when $\omega > 0$), we have

$$\omega(t) = \frac{y(t) - y(t - \Delta t) + 2\pi}{\Delta t} \quad y(t - \Delta t) - y(t) \geq \pi/2. \tag{4.26}$$

Besides, for the case that rotor position changes from sector 1 (y= $\pi/3$) to sector 6 (y= 2π) of the previous cycle (when $\omega < 0$), we have

$$\omega(t) = \frac{y(t) - y(t - \Delta t) - 2\pi}{\Delta t} \quad y(t) - y(t - \Delta t) \geq \pi/2. \tag{4.27}$$

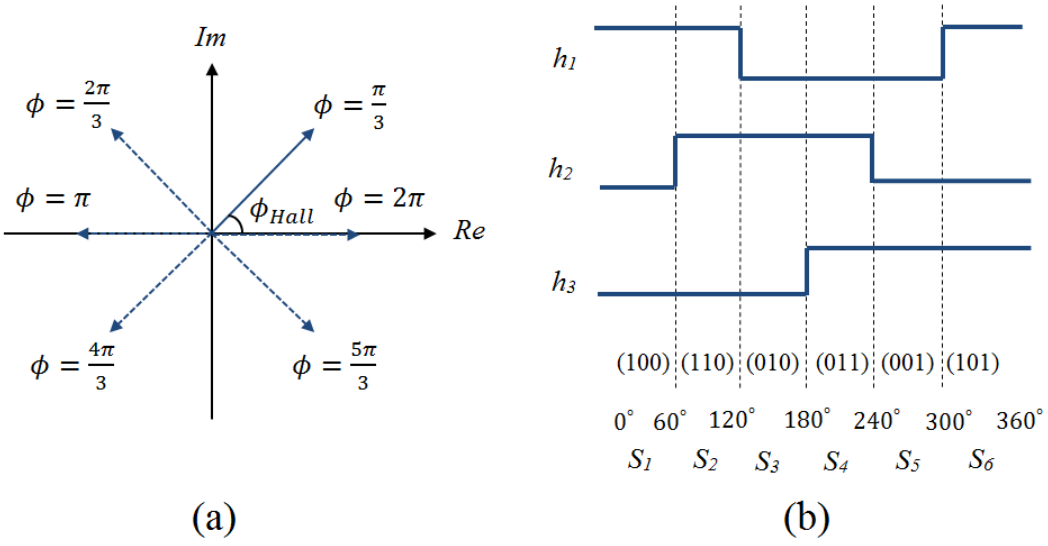

Figure 4.4: (a) Quantized states of ϕ_{Hall}, (b) Switching pattern of Hall sensors in one cycle.

Table 4.1: Experimental Parameters of the Setup

Parameter	Value
Terminal resistance phase to phase	0.2630 Ω
Terminal inductance phase to phase	10.033 mH
Nominal Voltage	24 V
Nominal current (max. continuous current)	7.39 A
Torque constant	23.2 mN.m/A
Speed constant	412 rpm/V
Number of pole pairs	1
Inverter DC voltage supply	30 V
Rotor inertia	53.8 g.cm^2
SVPWM frequency	10 kHz

Consequently, the angular rotor position is estimated as follows

$$\begin{cases} \phi(t) = y(t-\Delta t) + \omega(t-\Delta t)\Delta t & \omega > 0 \\ \phi(t) = y(t-\Delta t) + \omega(t-\Delta t)\Delta t + \frac{\pi}{3} & \omega < 0. \end{cases} \tag{4.28}$$

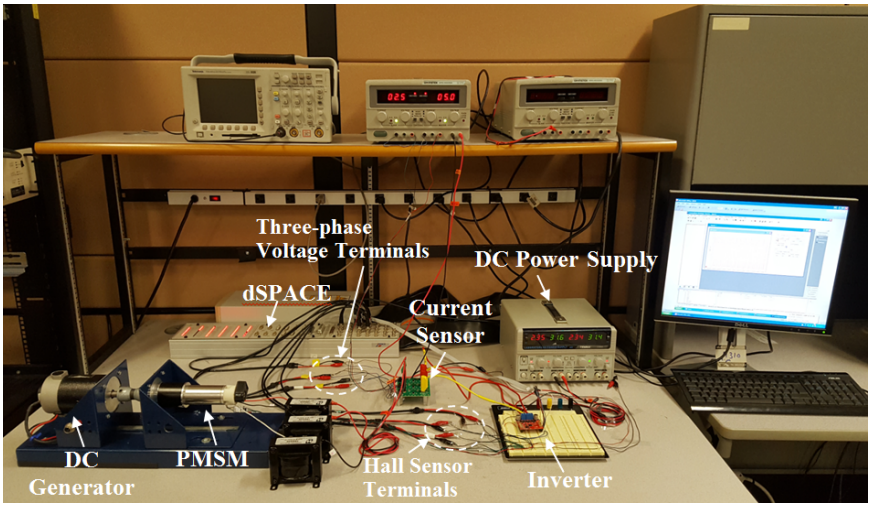

Figure 4.5: Experimental setup.

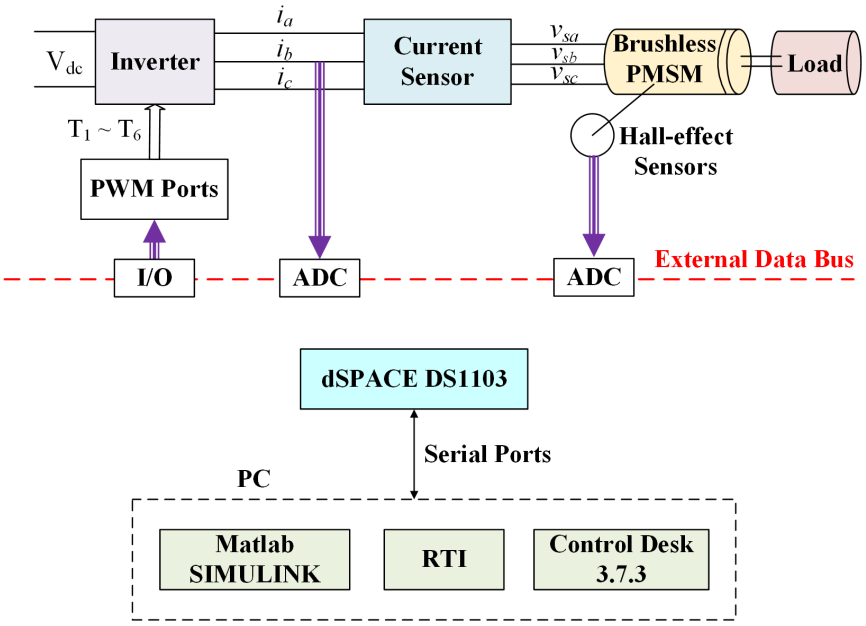

Figure 4.6: Real-time control structure of the setup using dSPACE control board.

4.3 Experimental Evaluation

4.3.1 Setup Description

Fig. 4.5 shows the experimental setup used in this project. A Maxon EC brushless permanent magnet synchronous motor is utilized with the objective of regulating the force applied to the motor shaft by controlling the PMSM current using the proposed MSES-tuned PI controller. The PMSM is connected to a

MAX Motion DC generator to produce the load torque. Since the internal motor inductance is very low ($0.033mH$ phase to phase), in all experiments an external inductor of $5mH$ with the resistance of $90m\Omega$ is connected to each phase terminal of the PMSM.

Fig. 4.6 shows the real-time control/hardware structure of the setup using dSPACE DS1103 board. The rotor position is obtained using Hall-effect sensors mounted on the motor. The measured Hall signals are sent to the controller via I/O ports of the dSPACE. The rotor position is obtained using the estimation scheme presented in section 4.2.3.

The PMSM is powered by a three-phase gate driver DRV 8305 by Texas Instruments. The inverter is connected to a DC power supply with $V_{dc} = 30V$. Six PWM pins of the inverter receive switching commands from the controller and produce the desired three phase stator currents.

An INA250A2 EVM current sensor is utilized in each phase to sense the phase current. The currents flowing through the shunt resistors of current sensors are multiplied by the current gain of INA250A2 (500mV/A) to generate the output voltages. The three-phase stator voltages are passed through dSPACE using ADC terminals and converted to the corresponding motor phase currents based on the gain of current sensors.

As shown in Fig. 4.6, the control block receives three phase currents along with position feedback, executes the torque control algorithm, and generates the gate signals via SVPWM. The SVPWM frequency is taken to be at least 10 times higher than the maximum motor rotation frequency, i.e., $f_{SVPWM} \geq 10 f_{max,motor} = 10kHz$. The output gate signals of the SVPWM are fed to the inverter switches through the I/O terminals of the dSPACE to regulate the phase currents.

4.3.2 Results

The proposed controller was built in the MATLAB/SIMULINK environment with a sampling frequency of $f_s = 10\ kHz$ and its performance was studied online using the *dSPACE Control Desk 3.7.3*. The setup specifications are shown in Table 4.1. In this table, the values for the phase-to-phase resistance and inductance are the total values considering both the motor and the external inductor resistance and inductance. Fig. 4.7 shows the experimental results when the proposed controller along with the rotor position estimation scheme presented in section 4.2.3 are applied to the PMSM. Assume that there is no load torque on the PMSM and the desired maximum amplitude of the stator phase currents is $I_{s,des} = 2A$. Fig. 4.7(a) shows the discontinuous rotor angle obtained from hall sensors as well as the continuous rotor angle obtained from the estimation

algorithm. To validate the estimation accuracy, the results are compared with those obtained from a shaft encoder mounted on the motor. Furthermore, the angle estimation error ratio (EER) is defined as

$$EER = \frac{Estimated\ rotor\ angle}{Actual\ rotor\ angle} \tag{4.29}$$

As the estimation improves, the EER gets close to 1. Ideally, when the estimated rotor angle matches the actual value, the $EER = 1$. Fig.4.7(b) shows the EER for the estimation in this study. As shown, the rotor angle estimation improves and gets to the actual value ($EER \approx 1$) in less than 0.2s which is reasonable in the long time span required in our case study.

The continuous stator position obtained from the estimation algorithm is fed to the SVPWM block and the inverter produces a sinusoidal phase current i_a as shown in Fig. 4.7(c). The quality of sinusoidal phase current depends on the SVPWM switching frequency as well as inductance values of the motor winding. By increasing f_{SVPWM} and L_{sabc}, the amplitude of high frequency oscillations on the sinusoidal waveform becomes smaller, resulting in a more smooth phase current. The PMSM produces a sinusoidal phase voltage v_a as shown in Fig. 4.7(d). Since the three phase currents are sinusoidal, the rotor torque and consequently I_s would be constant.

To study and compare the performance of the proposed controller, a similar current controller with fixed PI parameters and a recently proposed adaptive PI controller using gradient-based extremum seeking were applied to the setup and several tests were conducted which are presented in the following subsections.

Tracking Performance

In this experiment, the PMSM torque is regulated by changing the maximum amplitude of the desired stator phase current from $I_s = 2A$ to $I_s = 3A$ at $t = 15s$. Performance of the proposed controller, is compared with a similar current control using conventional PI controller as well as a gradient-based extremum seeking (GES) tuned PI controller. The conventional PI controller is tuned off-line using Ziegler-Nichols method such that stability of the controller is guaranteed [4, 55]. The obtained K_I and K_p are 0.7 and 0.95, respectively. The GES-tuned PI controller utilizes an online adaptive tuning method based on estimation of a gradient term and perturbing the PI gains using sinusoidal signals to minimize the cost function of the system [41]. For a fair comparison, the same cost function as defined in (4.7) is utilized for the GES-tuned PI controller. Moreover, the GES parameters are selected as $K_g = [1.5\ \ 0; 0\ \ 0.85]$,

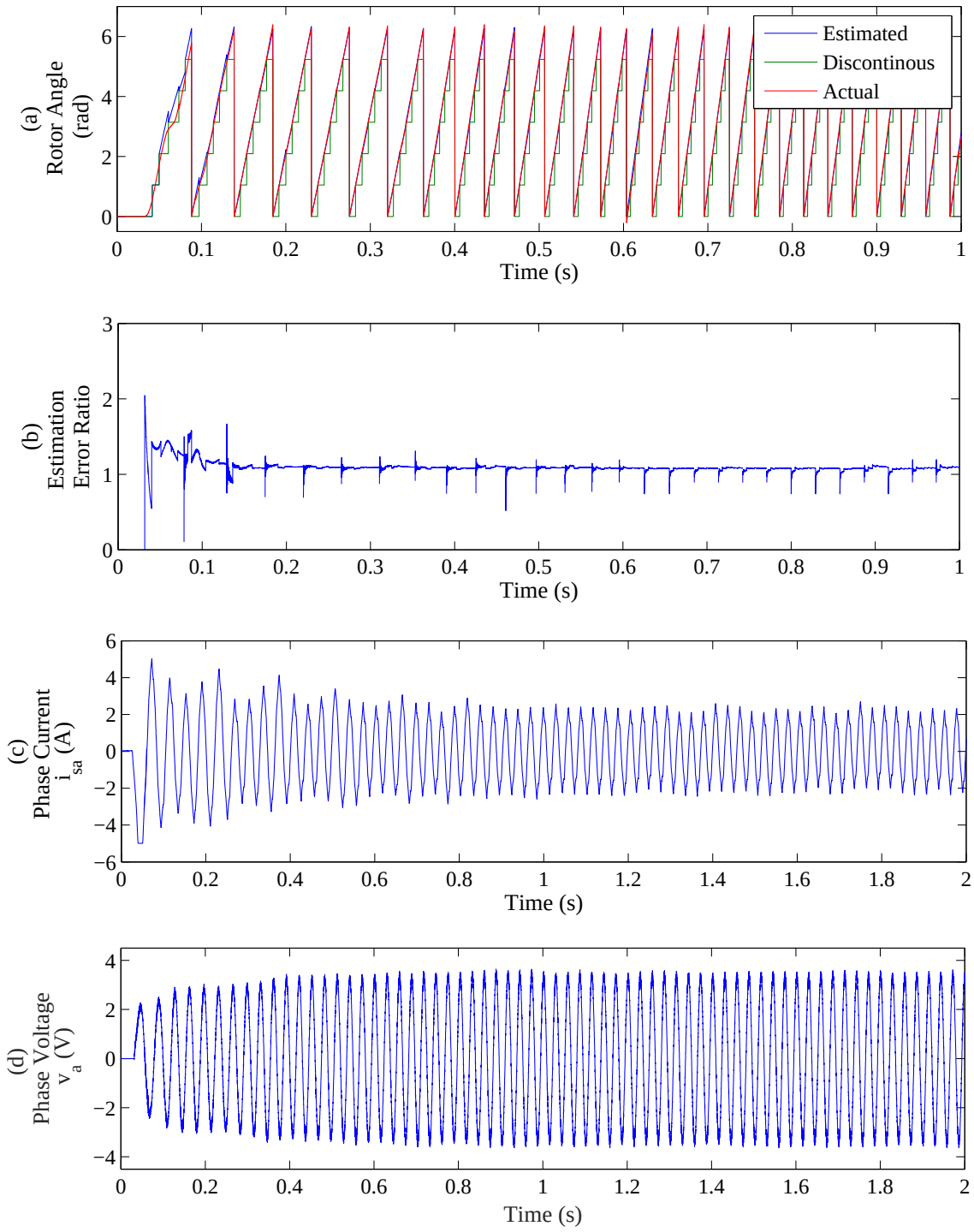

Figure 4.7: Experimental Results for (a) rotor angle estimation, (b) ratio of rotor angle estimation error (Estimated/Actual), (c) phase current i_{sa}, (d) terminal phase voltage v_a using the proposed MSES-tuned PI controller.

$[\omega_1 \ \omega_2] = [25 \ 15]$ for adding perturbation signal and $[\omega_1 \ \omega_2] = [15 \ 10]$ for multiplying perturbation signal.

Fig. 4.8 to Fig. 4.10 show the experimental results for three controllers. Before transient happens, the tracking performance of all controllers is relatively good. After $t = 15s$, the conventional PI controller tracks the desired value with some oscillations which needs re-tuning. However, the other two controllers exhibit better performance by having adaptive gains K_i and K_p. Comparing the two adaptive PI controllers, the GES-tuned PI controller has slight oscillations and reaches to steady state after $\approx 1s$. However, the other controller reaches the steady state very fast in less than $\approx 0.5s$. Comparing the figures showing evolution of the cost function for three controllers, the MSES-tuned PI controller can reach the minimum faster than the other two controllers. Moreover, as the desired amplitude I_s changes, the cost function increases slightly which has a higher value for the conventional and GES-tuned PI controllers. Furthermore, the average ISE values of the three controllers for 5 repetitions during the time interval $T = [0, 30]$ are obtained as 0.015, 0.041 and 0.077 for the MSES-tuned, GES-tuned, and conventional PI controllers, respectively.

Appropriate parameter selection improves performance of the proposed controller. Based on the experiments, increasing K_i results in an increase in the convergence speed of the proposed controller to $I_{s,des}$. However, as K_i becomes very large, I_s is distorted more. Moreover, as K_p increases, I_s becomes more smooth. But large values of K_p result in lower convergence speed of the PI controller. Thus the PI parameters should be selected such that fast convergence along with smooth tracking is achieved while stability is guaranteed.

Besides, choosing the ES parameters properly guarantees minimization of $J(\boldsymbol{\theta})$. As k_{gi} is increased, the convergence speed to the extremum point $\boldsymbol{\theta}^*$ increases. However, a fast convergence compromises steady-state performance [19], [97].

It is also desirable to keep α_i as small as possible, since a larger α results in large steady state oscillations of the PI parameters. However, $\alpha_i's$ cannot be selected to be very small. To guarantee convergence of the PI parameters to the optimum values, the lower bound of α_i should be restricted [19].

Accordingly, K_g and P are selected as $K_g = [1.7 \ \ 0; 0 \ \ 0.3]$ and $P = [0.1 \ \ 0.45]$. Based on the experiments, if α_1 and α_2 are greater than 1.5, K_i and K_p have large oscillations and I_s becomes unstable. In contrast, if α_1 and α_2 are selected to have a value less than 0.01, there would be no change in α_1 and α_2 as the desired stator current varies. Hence, $\alpha_i's$ are selected as $[\alpha_1 \ \ \alpha_2] = [0.06 \ \ 0.07]$.

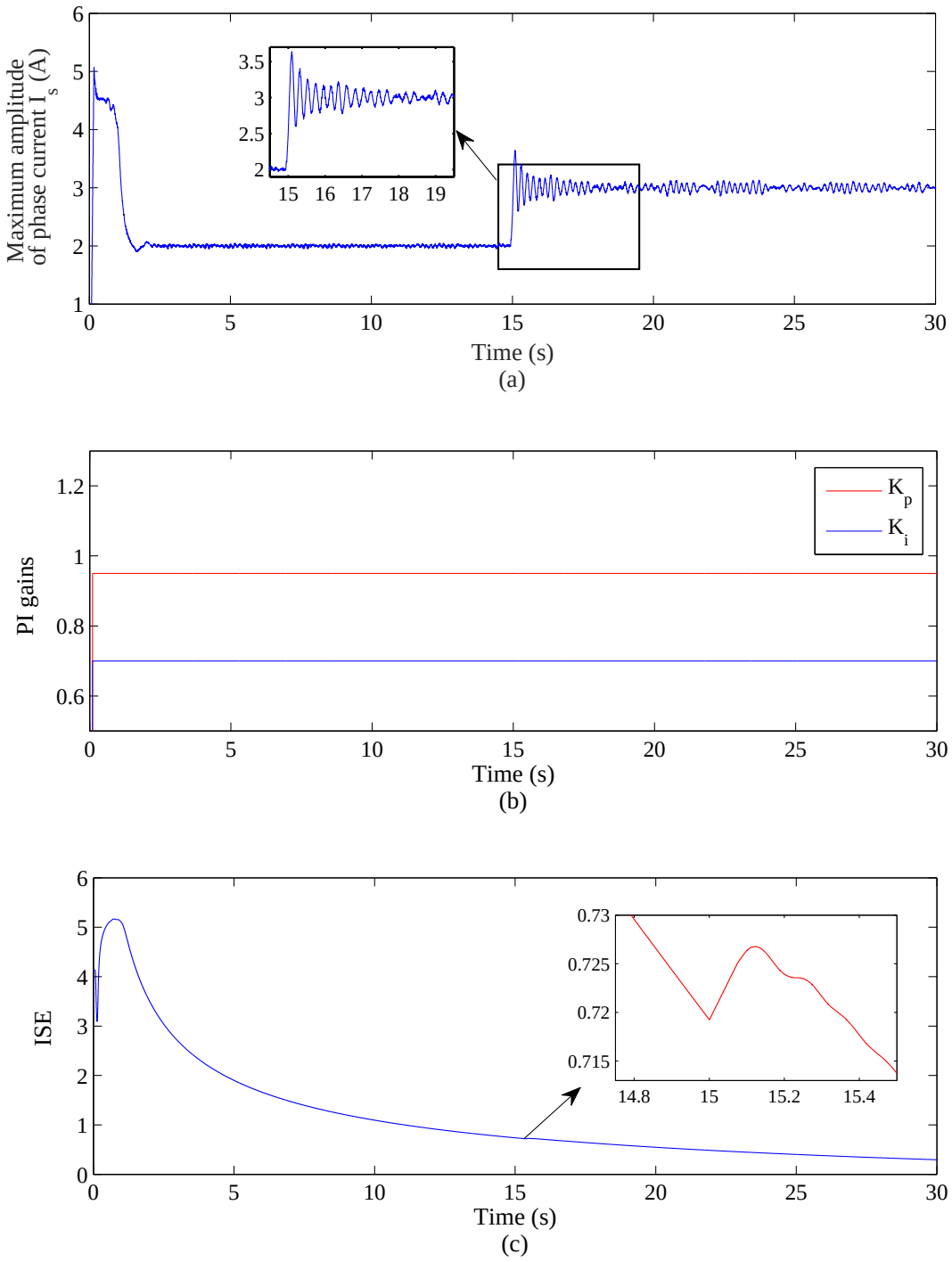

Figure 4.8: Tracking performance of the conventional PI controller when I_s changes from 2 to $3A$ at $t = 15s$: (a) I_s, (b) PI parameters, (c) evolution of cost function.

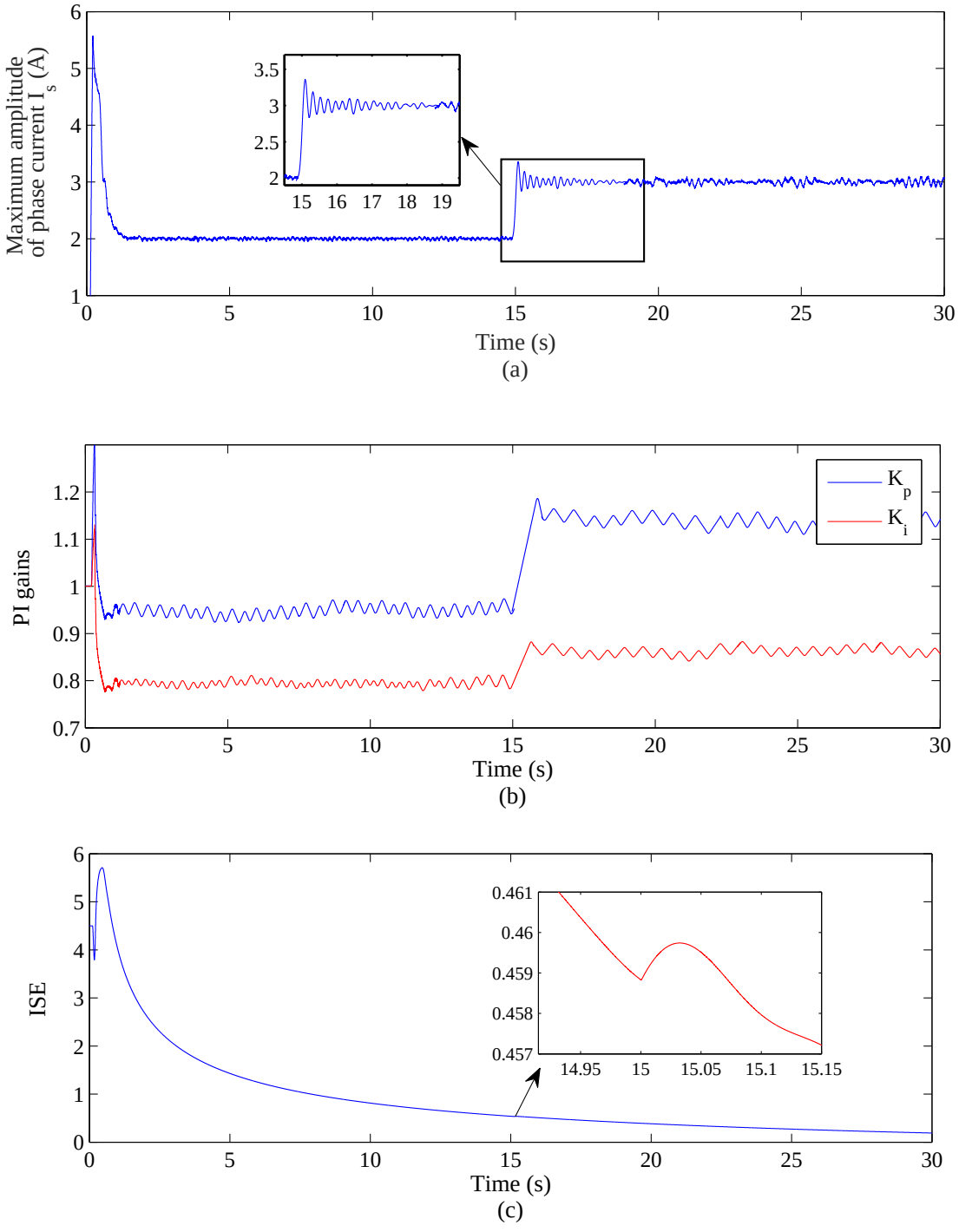

Figure 4.9: Tracking performance of the proposed GES-tuned PI controller when I_s changes from 2 to $3A$ at $t = 15s$: (a) I_s, (b) PI parameters, (c) evolution of cost function.

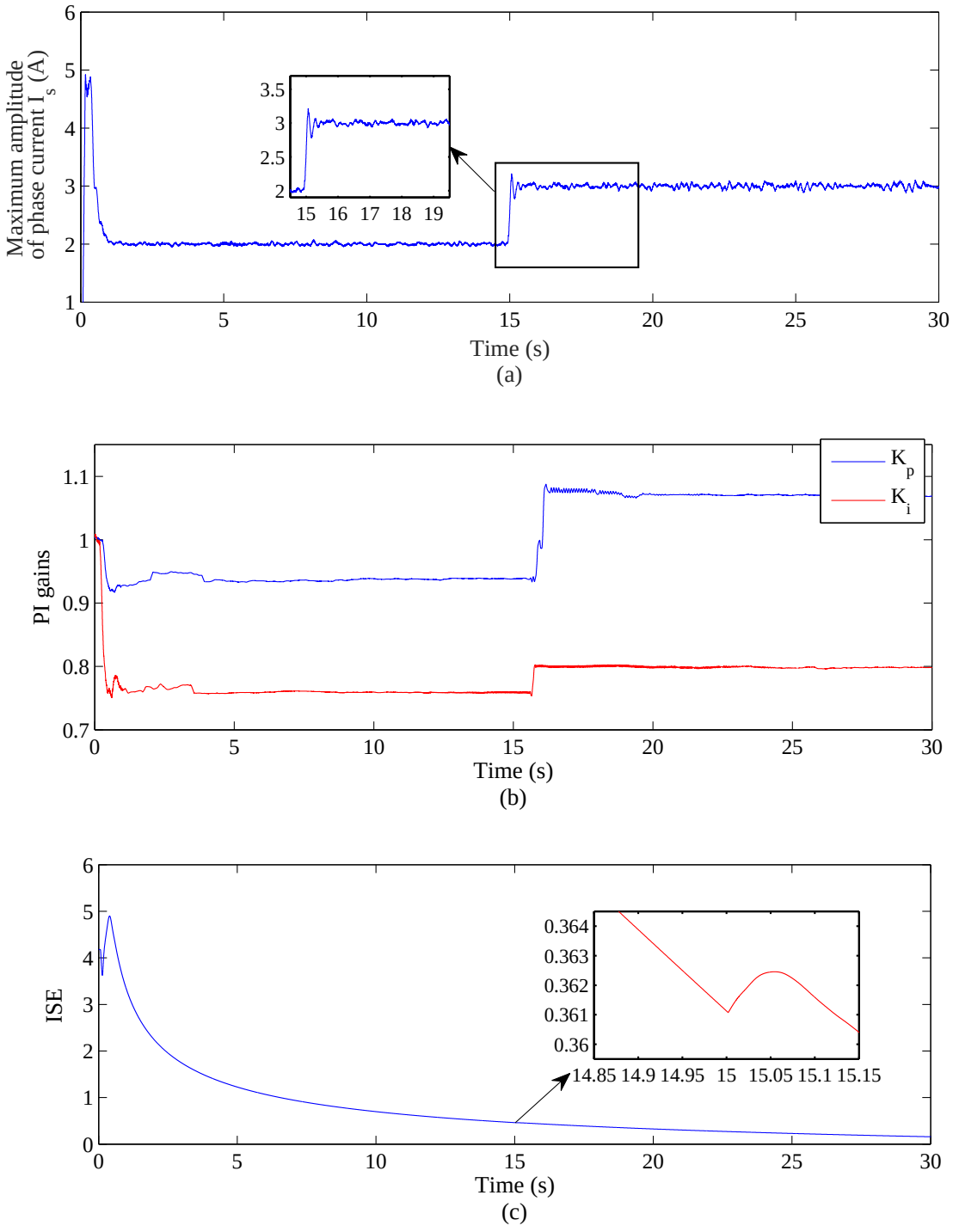

Figure 4.10: Evolution of the cost function in MSES tuning method when I_s changes from 2 to $3A$ at $t = 15s$: (a) I_s, (b) PI parameters, (c) evolution of cost function.

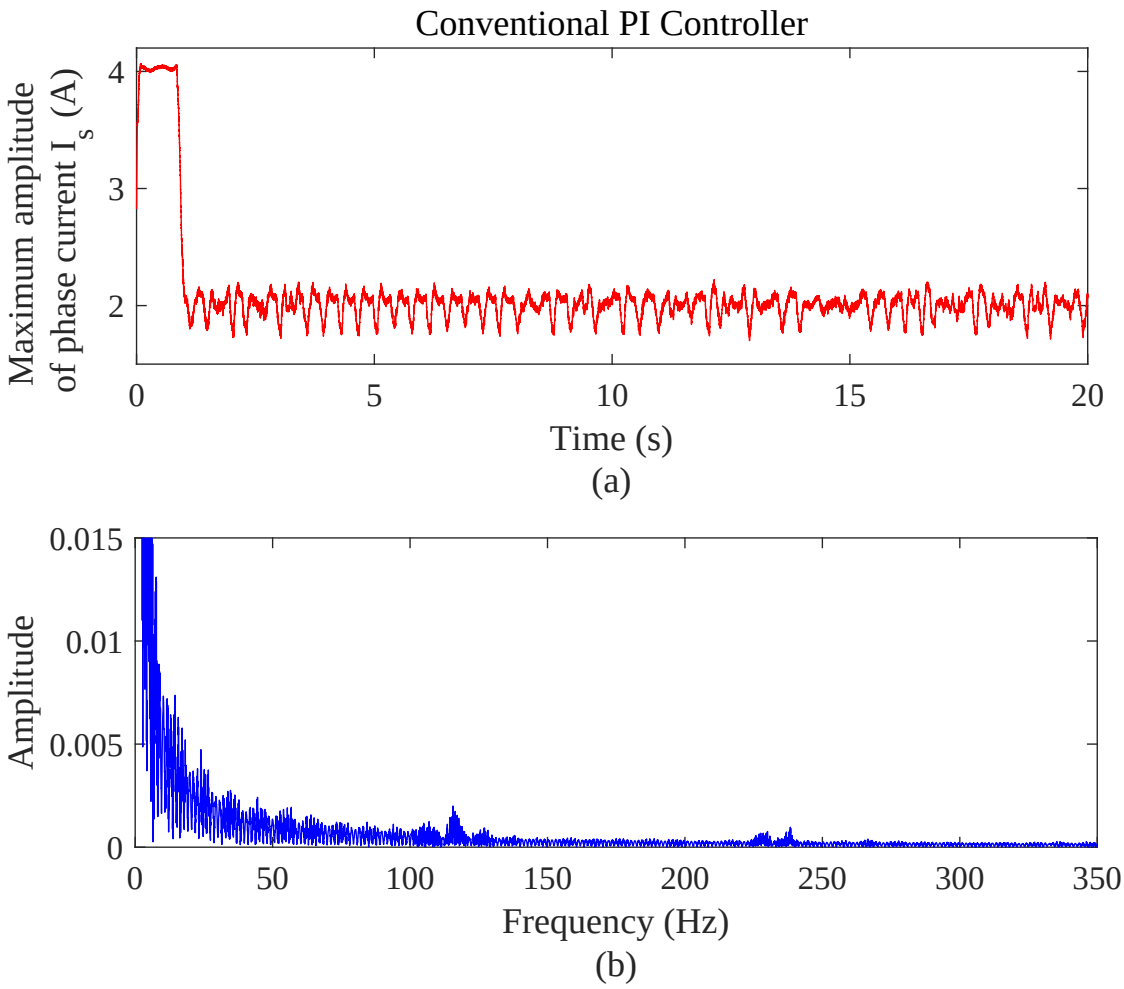

Figure 4.11: Effect of decreasing the motor impedance ($R = 105.5m\Omega$, and $L = 4.017mH$) for conventional PI controller.

Effect of Parameter Variations

In the next experiment, the three-phase impedance of the PMSM is changed to evaluate performance of the proposed controller to parametric variations. The initial resistance and inductance values in each phase of PMSM are $R = 131.5$ $m\Omega$ and $L = 5.017$ mH. First, assume that the three-phase impedance of the motor is decreased to $R = 105.5$ $m\Omega$ and $L = 4.017$ mH, i.e., the external inductor is replaced with another inductor with lower resistance and inductance. Then the proposed MSES-tuned PI and the GES-tuned PI controller used in previous test are applied to the system to see how well they can regulate the PMSM 3-phase current amplitude regardless of the change that has happened in the value of PMSM parameters (the phase impedance). Assume $I_{s,des} = 2A$. Fig.

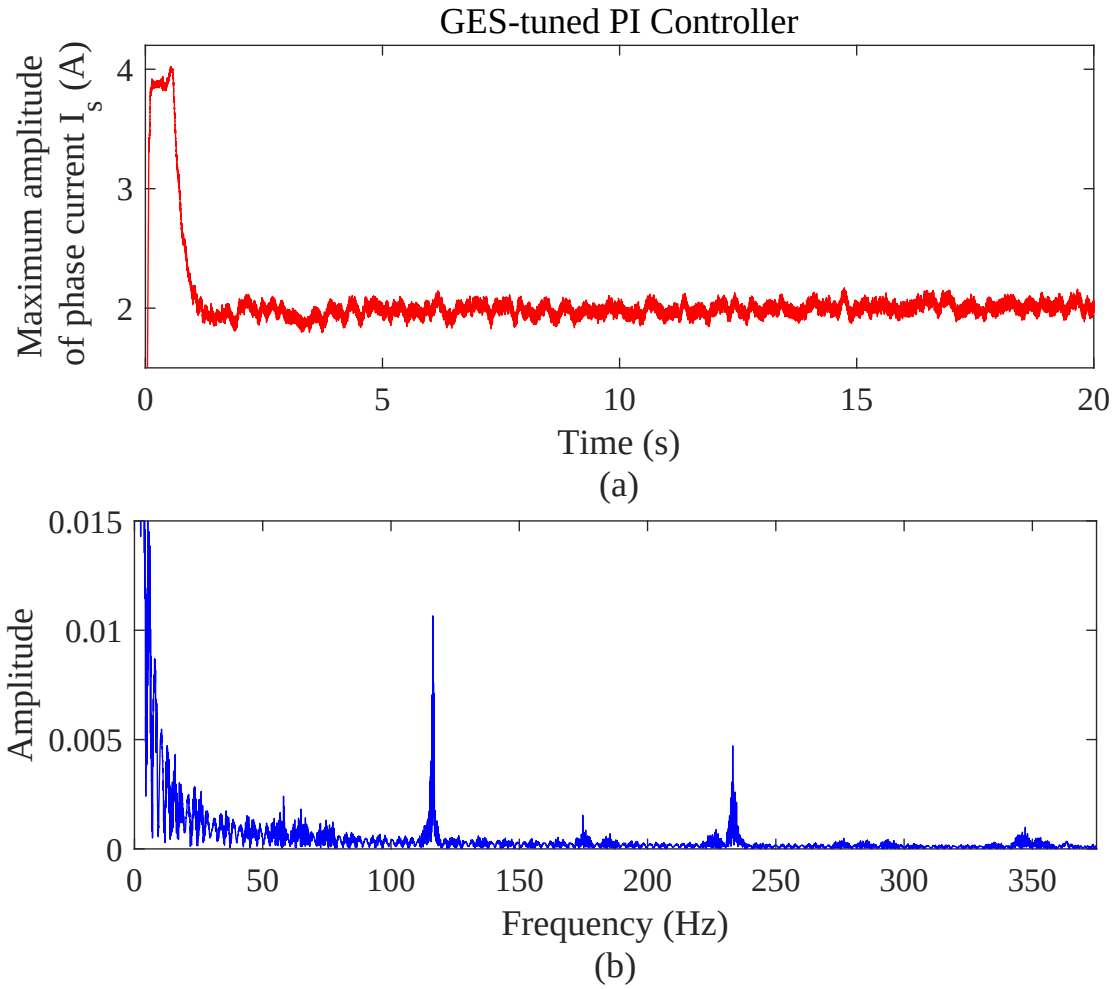

Figure 4.12: Effect of decreasing the motor impedance ($R = 105.5m\Omega$, and $L = 4.017mH$) for GES-tuned PI controller.

4.11 to Fig. 4.13 show the experimental results for current regulation as well as frequency spectrum for the three controllers. As shown, by decreasing the three-phase inductance of the motor, the amplitude of high frequency oscillations on the output response is increased when compared with the tracking response in previous study. The conventional PI controller needs manual offline re-tuning. The two adaptive controllers re-tune PI gains online to minimize the tracking response error, however, the proposed controller has a more smooth tracking response compared with the other controller.

To study robustness of the controllers in face of parameter variations, frequency spectrum of I_s was obtained for all controllers. Considering the fundamental frequency of $20Hz$, the amplitude of 6^{th} and 12^{th} harmonics in the GES-tuned PI controller is relatively high. However, no high-order harmonics can

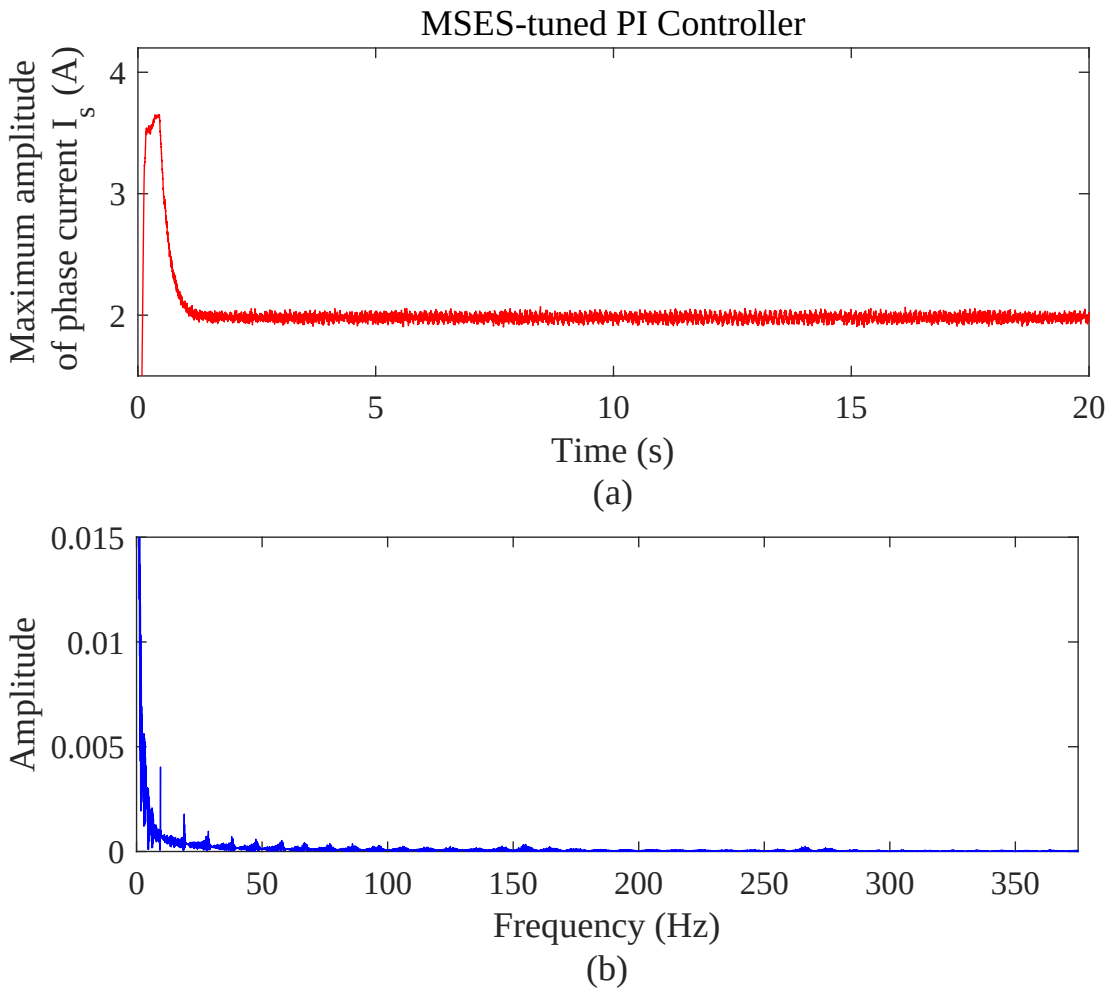

Figure 4.13: Effect of decreasing the motor impedance ($R = 105.5m\Omega$, and $L = 4.017mH$) for PI controller using MSES tuning.

be seen in the frequency spectrum of the proposed MSES-tuned PI controller, which means that the proposed controller is able to reject high-order frequencies better than the other controller when PMSM parameters vary. Moreover, compared with the proposed controller, the conventional PI controller has higher amplitude low-frequency harmonics.

Now assume that the three-phase impedance of the motor increases to $R = 156.5\ m\Omega$ and $L = 5.517\ mH$ by adding an inductor with resistance of $29m\Omega$ and inductance of $0.5mH$ to the external inductor of $5mH$. Then the three controllers with the same conditions as the previous case study are applied to the motor and the results for current regulation and frequency spectrum of I_s are obtained as shown in Fig. 4.14 to Fig. 4.16. As it can be seen, the proposed MSES-tuned PI controller reaches the steady state response in less than $2s$. However, the

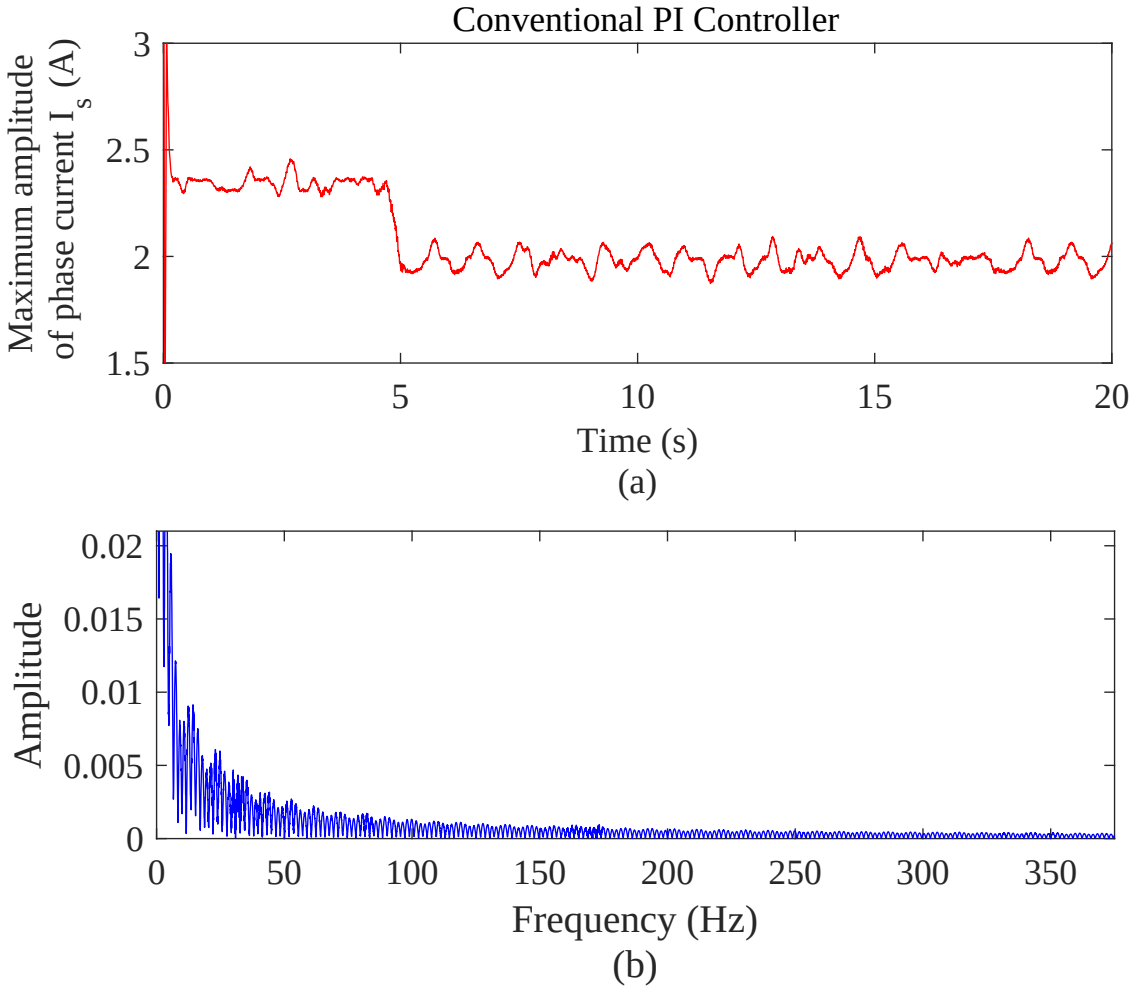

Figure 4.14: Effect of increasing the motor impedance ($R = 156.5m\Omega$, and $L = 5.52mH$) for conventional PI controller.

conventional PI controller reaches the steady state after $5s$ which is still not as smooth as the tracking result of the proposed controller. Choosing large values for three phase motor resistors limits the stator current from increasing. This explains why, in Fig. 4.14 to Fig. 4.16, I_s is limited and does not experience a sudden jump at the beginning of tracking. For further comparison of three controllers see Table 4.2. In this table, the average values of PI gains as well as the ISE during time interval $[0, 20]$ for five repetitions of test 2 are shown. Moreover, comparing the frequency spectrum in three controllers, the amplitude of high-order frequencies for the conventional and GES-tuned PI controllers is higher than the proposed control method.

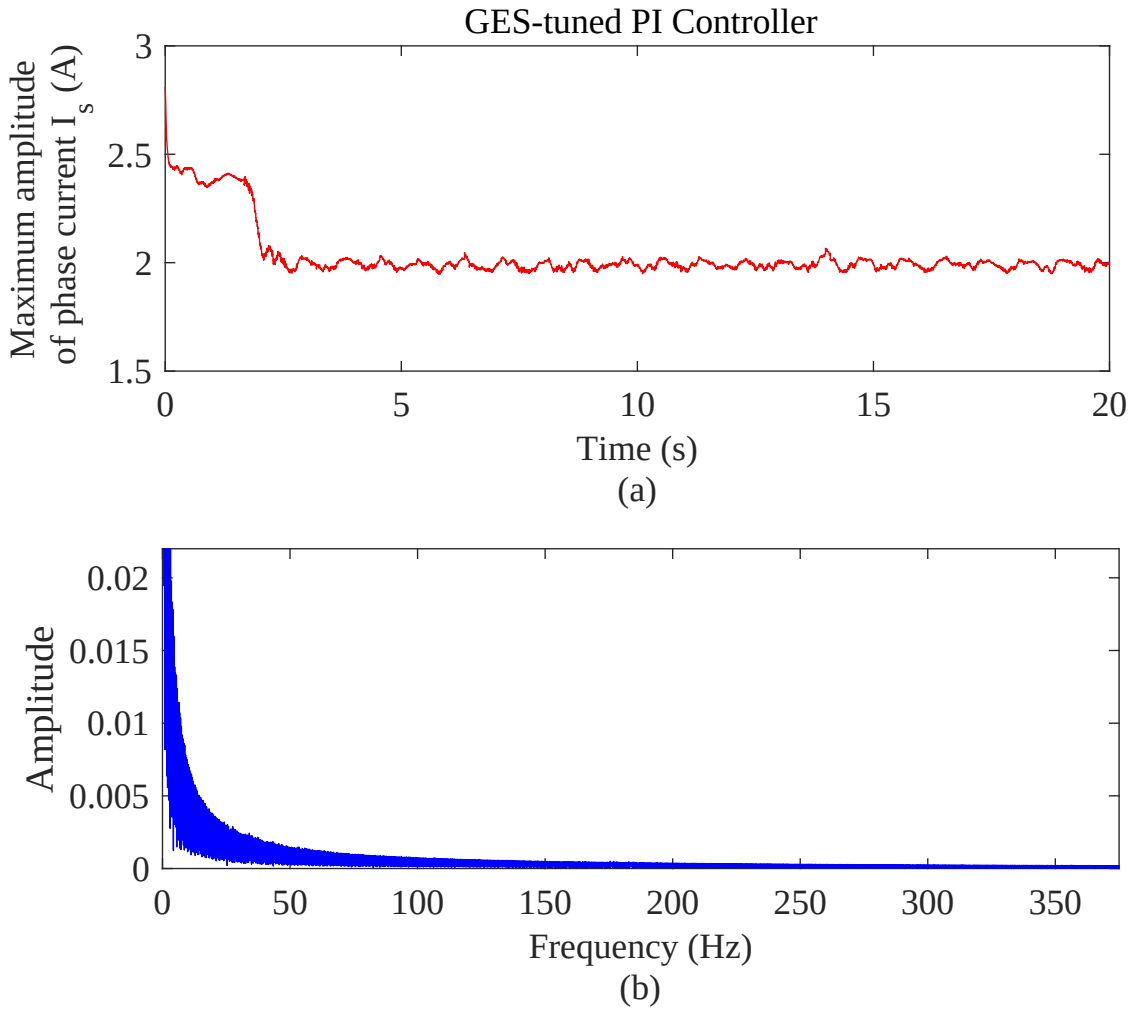

Figure 4.15: Effect of increasing the motor impedance ($R = 156.5m\Omega$, and $L = 5.52mH$) for GES-tuned PI controller.

Load Torque Disturbance

To test performance of the proposed controller in case of load torque disturbances, a variable load torque was applied to the motor. To generate the variable load torque T_L, a Maxon Motion DC generator with terminal resistance $R = 3.9\Omega$ and terminal inductance $L = 0.065mH$ was connected to the motor shaft and the load current was increased gradually between $t = 5s$ to $t = 20s$ from $i_{load} = 0A$ to $i_{load} \simeq 2.5A$ as shown in Fig. 4.17. Thus, we have [12]

$$T_m + T_L + T_f = I_{tot}\dot{\omega} \tag{4.30}$$

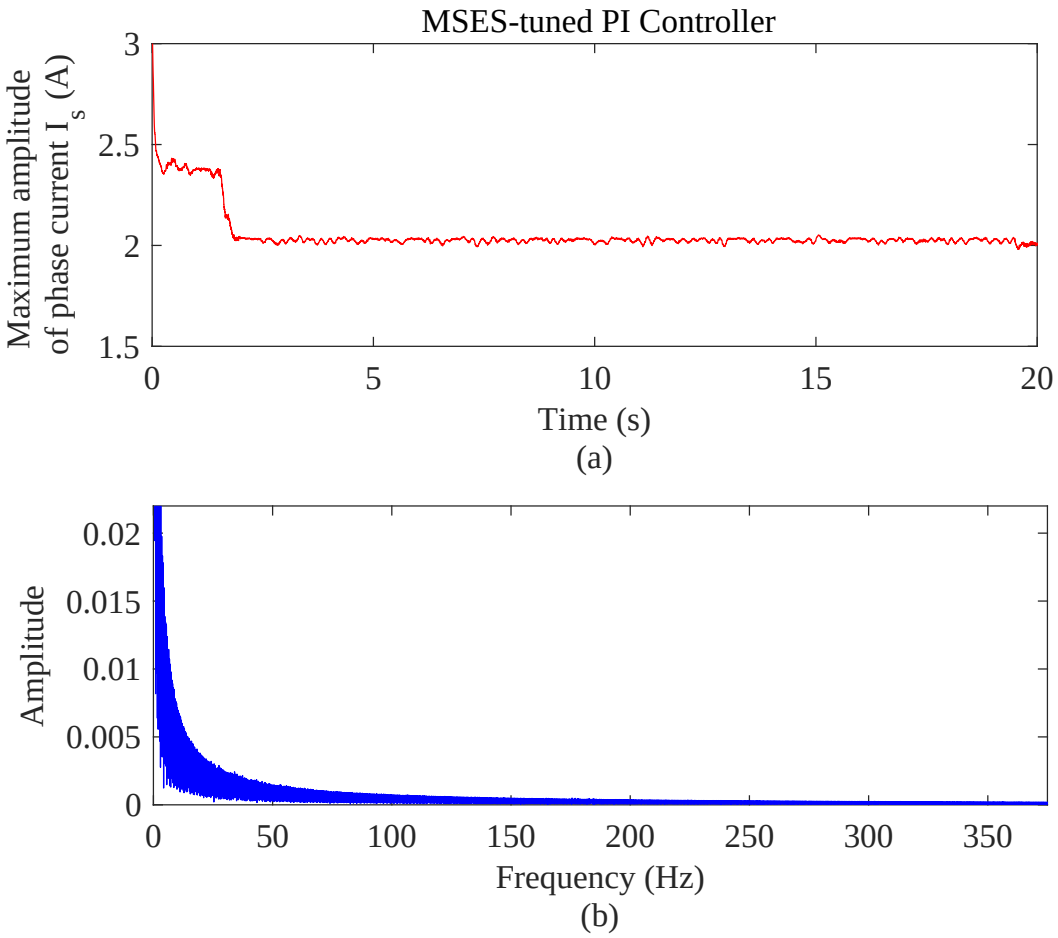

Figure 4.16: Effect of increasing the motor impedance ($R = 156.5m\Omega$, and $L = 5.52mH$) for PI controller using MSES tuning.

where T_m, T_L and T_f are motor, load, and friction torques, respectively. Moreover, I_{tot} is the total inertia of the shaft and ω is the motor angular velocity. When there is no load applied to the motor ($T_L = 0$) and the motor is in steady state, the angular velocity remains constant, i.e., $\dot{\omega} = 0$. Assuming that T_m is fixed, by applying a load torque to the motor, the friction torque and the shaft velocity will change. If the load torque T_L is applied in the same direction as T_m, the shaft velocity and the three-phase back-EMF increase. This disturbs the stator three-phase current.

In this experiment, the objective is that the controller keeps the stator maximum amplitude at $I_s = 3A$ regardless of the load torque disturbance. Fig. 4.18 to Fig. 4.20 show the experimental result for the three controllers when the DC generator and the motor are rotating in the same direction. In this case, I_s decreases during the loading process. As the load torque changes, the GES-tuned

Table 4.2: Comparison of Three Controllers Considering the Effect of Impedance Changes

	Controller	K_p	K_i	ISE
Decreasing impedance	MSES-tuned PI	1.15	0.64	0.0861
	GES-tuned PI	1.23	0.58	0.1045
	Conventional PI	0.95	0.7	0.1663
Increasing impedance	MSES-tuned PI	1.41	1.15	0.0185
	GES-tuned PI	1.93	1.21	0.0327
	Conventional PI	0.95	0.7	0.0716

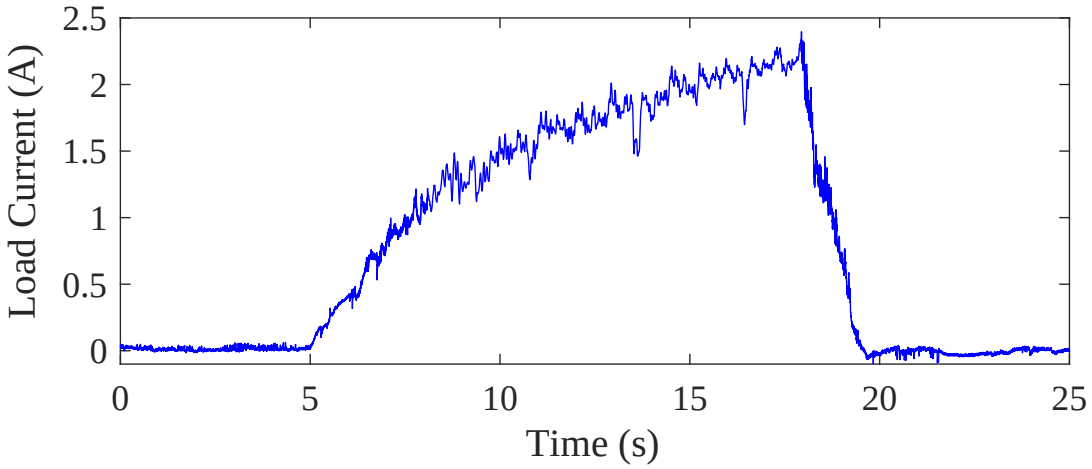

Figure 4.17: Variable load current applied to DC generator from $t = 5s$ to $t = 20s$.

and MSES-tuned PI controllers minimize the tracking error by re-tuning K_p and K_i. As shown, the proposed controller has a better performance in terms of rejecting the load torque disturbance when compared with the controller using gradient-based PI tuning as well as the conventional PI controller. Moreover, comparing the figures showing evolution of ISE, there is an increase in the amplitude of ISE at $t = 18s$ for the GES-tuned and conventional PI controllers, whereas no obvious change can be found in the ISE figure for the proposed MSES-tuned PI controller at the same time. To have a fair comparison, the test was conducted 5 times and the average ISE values during the time interval $[0, 25]$ were obtained as 0.1813, 0.1163 and 0.0758 for conventional, GES-tuned, and the proposed MSES-tuned PI controllers, respectively.

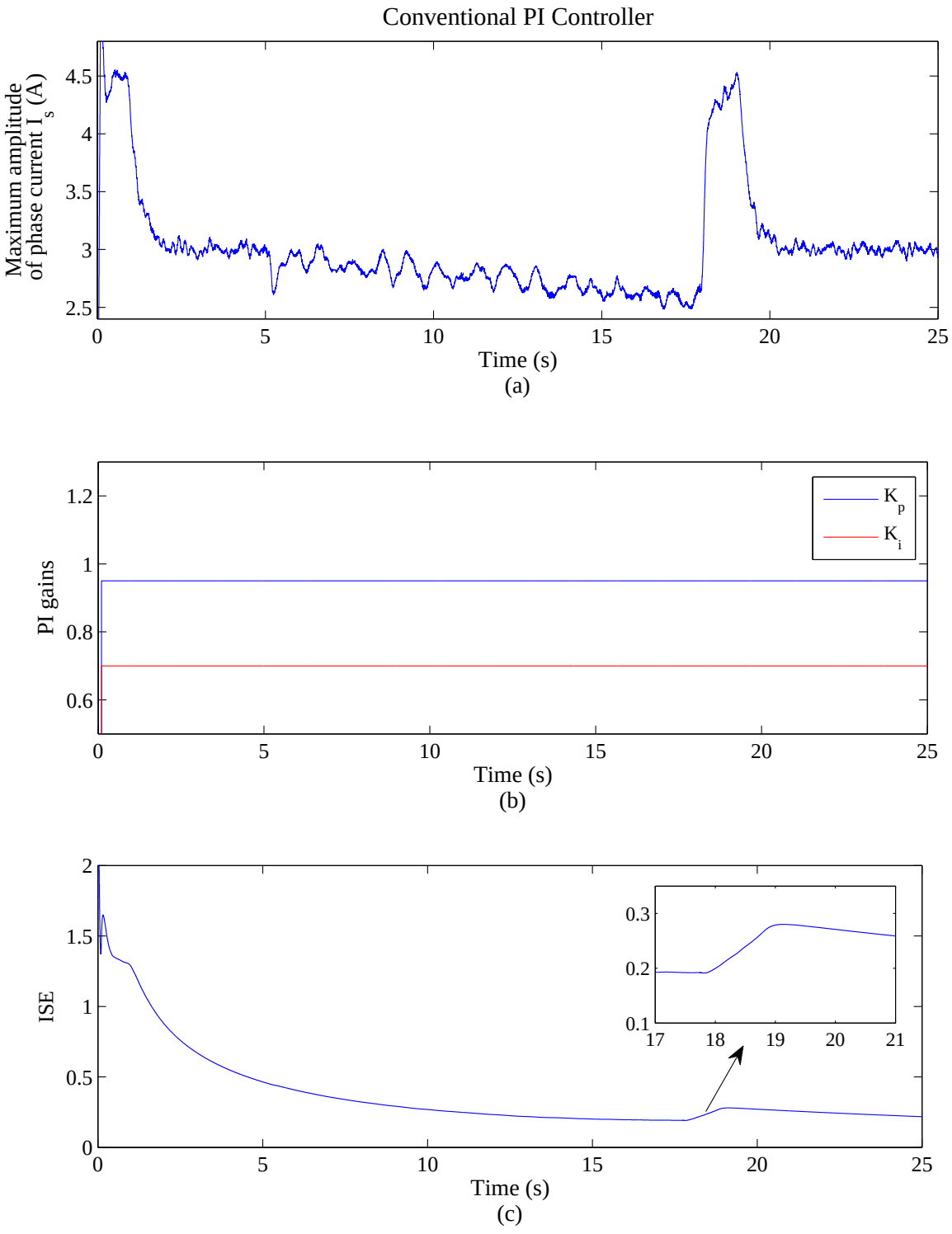

Figure 4.18: Tracking response of conventional PI controller in face of variable load torque.

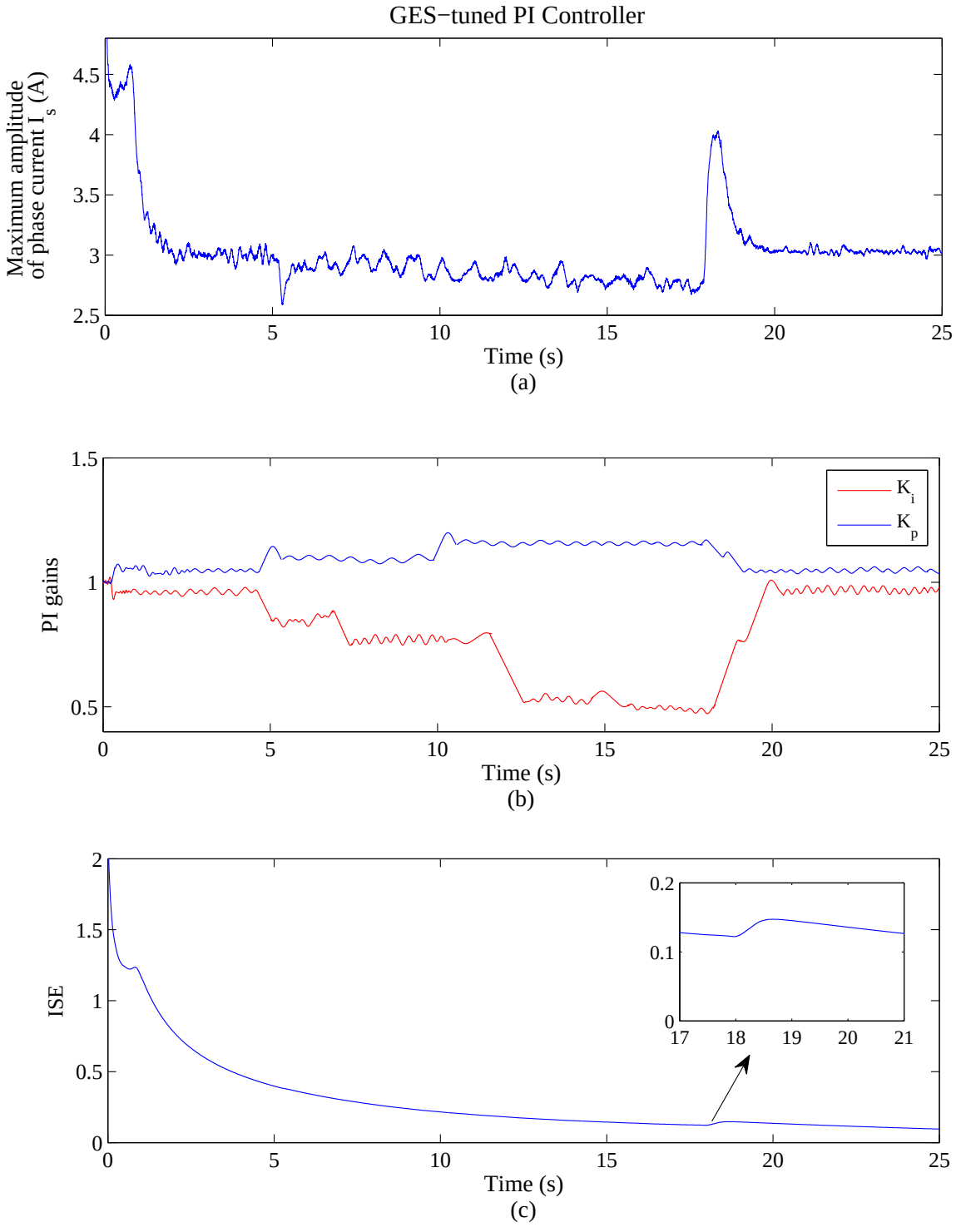

Figure 4.19: Tracking response of GES-tuned PI controller in face of variable load torque.

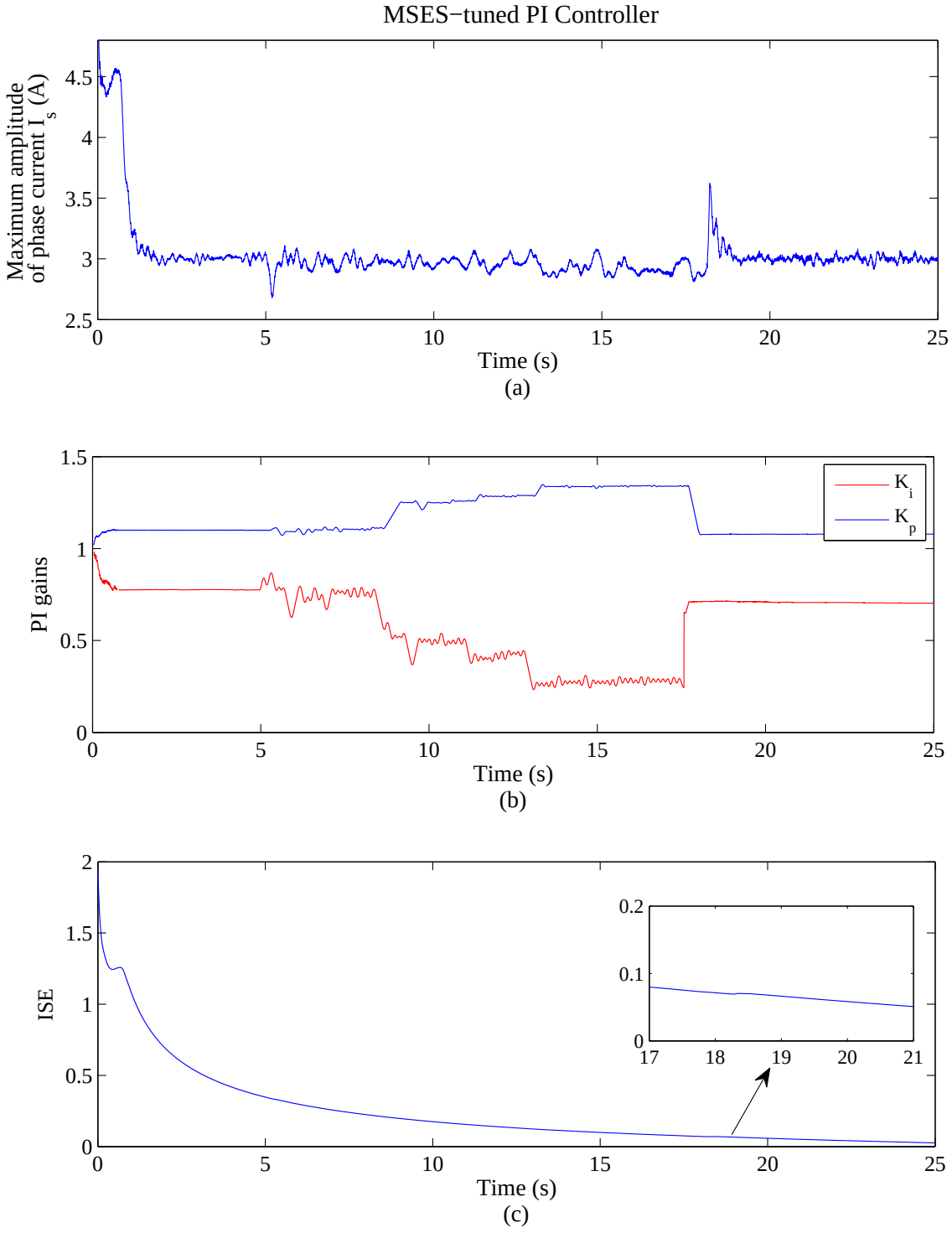

Figure 4.20: Tracking response of the proposed MSES-tuned PI controller in face of variable load torque.

4.4 Conclusion

In this chapter, a new PI tuning method based on multivariable sliding-mode extremum seeking is proposed. The proposed scheme makes PI parameters adaptive to minimize the effect of disturbances and parameter variations on the system performance. The proposed PI control is applied to a brushless PMSM to regulate the motor torque based on regulating the maximum amplitude of the stator three-phase currents. The rotor position is obtained using Hall-effect sensors followed by a continuous motor position estimation algorithm. The performance of proposed MSES-tuned PI controller is verified by comparing its control results with a conventional fixed-gain PI controller and a recently proposed adaptive PI controller using gradient-based ES tuning method. Experimental results reveal that the proposed controller has a faster convergence speed and a more smooth tracking response during transient conditions. Moreover, it has higher robustness to phase impedance variations and variable load torque disturbances compared with the other two controllers.

Chapter 5

PMSM Torque Ripple Minimization and Control using Multi-objective Extremum Seeking

Torque regulation is often required in mechatronic motion control applications such as exercise machines in which the mechanical force has to be regulated during the motion [14,53,93,94]. Although PMSMs are widely utilized in motor-driven exercise machines, their efficiency is limited due to parasitic torque pulsations when the machin is running at low speeds [71, 92]. Imperfections such as cogging torque, current measurement error, and non-sinusoidal flux density distribution around the air gap cannot always be filtered by the system inertia, which may lead to degradation of the drive system performance and undesirable mechanical vibrations [68]. In this chapter, a multi-objective extremum-seeking (MOES) approach is proposed for torque control of a PMSM and minimization of its torque ripple. The latter aspect is specifically important in human-machine interface applications such as haptic interfaces requiring smooth torque profiles at slow speeds. The proposed MOES scheme combines an adaptive iterative learning control (AILC) method with an adaptive PI controller which makes the system less sensitive to load disturbances and improves the control performance for torque regulation during transient events. Experiments are performed on a proof-of-concept exercise machine that generates desired torque profiles and mechanical impedance based on user's preference.

This chapter is organized as follows. In section 5.1, an overview of the motor-driven system which emulates an exercise machine using a PMSM is presented. In section 5.2, the proposed MOES is presented and applied to the system. In section 5.3, performance of the proposed controller is investigated through

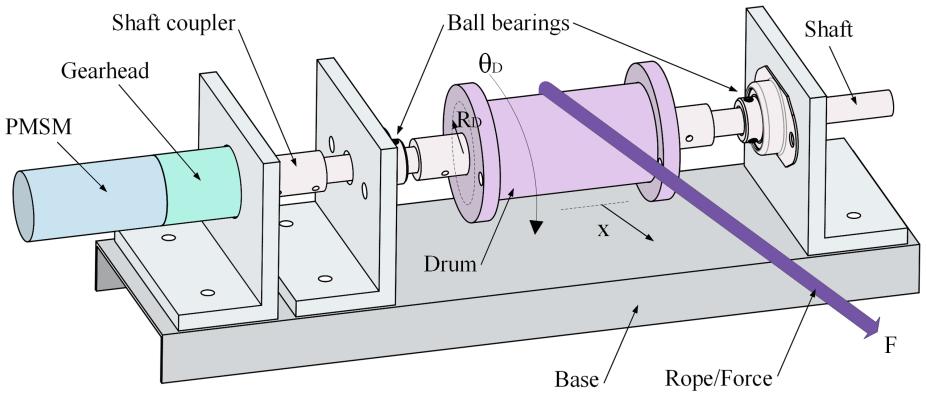

Figure 5.1: Mechanical structure of the motor-driven torque generator.

experimental tests and comparing the results with a recently proposed adaptive PI controller. Conclusions are presented in section 5.4.

5.1 Problem Formulation of the Drive System

5.1.1 Motor-driven Torque Generator

Fig. 5.1 shows the test bed for PMSM torque control. The system is comprised of a PMSM, a gear-head, and a cylindrical drum which are connected together through a shaft. The pull rope wound around the drum allows the user to apply force through the handle. Using PMSM, the machine can produce any desired amount of force and mechanical characteristics. The device is a simple force control system that can be utilized as an exercise machine with programmable force profiles and mechanical impedances. In this study we would like to emulate mechanical impedances such as spring or damper through force control at the end of the rope. Let us define the displacement x as follows

$$x = \theta_D R_D \tag{5.1}$$

where R_D and θ_D are radius and angular position of the cylindrical drum, respectively. As the user pulls the rope with force F, the motor applies a torque T_m in the opposite direction to the rope handle. When emulating a spring behavior, the motor torque should be proportional to the displacement of the handle, x, as follows

$$T_m \propto -x \tag{5.2}$$

Similarly, when a damper is emulated the torque should be proportional to the speed, $\dot{x}$, as follows

$$T_m \propto -\dot{x} \tag{5.3}$$

5.1.2 PMSM Torque Equation

Assuming that the PMSM has a star configuration, the motor electrical equations are given by

$$\begin{aligned} v_{sa} &= i_{sa}R + L\frac{di_a}{dt} + e_a \\ v_{sb} &= i_{sb}R + L\frac{di_b}{dt} + e_b \\ v_{sc} &= i_{sc}R + L\frac{di_c}{dt} + e_c \end{aligned} \tag{5.4}$$

where v_{sa}, v_{sb} and v_{sc} are the three phase stator voltages; i_{sa}, i_{sb} and i_{sc} are the three phase stator currents; L is the inductance of each phase, including the mutual inductance; and R is the resistance of stator winding per phase.

Then, the electromechanical torque generated by the PMSM can be obtained as follows [39]

$$P_m = \sum_{n=a,b,c} e_n i_{sn}. \tag{5.5}$$

Considering (5.4), in case of balanced stator currents, P_m can be rewritten as

$$P_m = \sum_{n=a,b,c} (v_{sn}i_{sn} - i_{sn}^2 R - \frac{1}{2}L\frac{di_{sn}^2}{dt}). \tag{5.6}$$

Accordingly, the motor electromagnetic torque is obtained as follows

$$T_m = \frac{P_m}{\omega_r} = \frac{1}{\omega_r}\sum_{n=a,b,c} (v_{sn}i_{sn} - i_{sn}^2 R - \frac{1}{2}L\frac{di_{sn}^2}{dt}) \tag{5.7}$$

where ω_r is the rotor angular velocity which is a function of the mechanical shaft speed ω_m and number of poles ρ, i.e., $\omega_r = \frac{2}{\rho}\omega_m$.

Assuming that the stator sinusoidal currents are

$$\begin{aligned} i_{sa} &= I_s sin(\sigma) \\ i_{sb} &= I_s sin(\sigma + \frac{2\pi}{3}) \\ i_{sc} &= I_s sin(\sigma - \frac{2\pi}{3}) \end{aligned} \tag{5.8}$$

where I_s is the amplitude of stator three phase currents and σ is the electrical angle of the shaft, the sum of the squares of phase currents results in a constant value as follows

$$\sum_{n=a,b,c} i_{sa}^2 = I_s^2[sin^2(\sigma) + sin^2(\sigma + \frac{2\pi}{3}) + sin^2(\sigma - \frac{2\pi}{3})] = \frac{3}{2}I_s^2. \tag{5.9}$$

Therefore, the third term of (5.7) vanishes and torque expression is reduced to

$$T_m = \frac{1}{\omega_m}\frac{\rho}{2}\sum_{n=a,b,c}(v_{sn}i_{sn} - \frac{3}{2}I_s^2R). \tag{5.10}$$

If the Ohmic losses in the windings are neglected, (5.10) reduces to a simple expression as follows

$$T_m = \frac{1}{\omega_m}\frac{\rho}{2}\sum_{n=a,b,c} v_{sn}i_{sn}. \tag{5.11}$$

Now consider the back-emf expression given by [5]

$$\begin{bmatrix} e_a \\ e_b \\ e_c \end{bmatrix} = \omega_r\lambda_m \begin{bmatrix} sin(\sigma) \\ sin(\sigma + \frac{2\pi}{3}) \\ sin(\sigma - \frac{2\pi}{3}) \end{bmatrix}. \tag{5.12}$$

where λ_m is the rotor permanent magnetic flux. Considering (5.5) and (5.12), the electromagnetic torque can be obtained as

$$T_m = \frac{\rho}{2}\lambda_m[i_{sa}sin(\sigma) + i_{sb}sin(\sigma + \frac{2\pi}{3}) + i_{sc}sin(\sigma - \frac{2\pi}{3})]. \tag{5.13}$$

After doing algebraic manipulations, (5.13) can be simplified as follows

$$T_m = K_tI_s. \tag{5.14}$$

where $K_t = \frac{3}{2}\frac{\rho}{2}\lambda_m$ is the torque constant of the motor. Based on (5.14), the PMSM electromagnetic torque is proportional to the maximum amplitude of the stator current, i.e., $I_s \propto T_{shaft}$ [86].

At high speeds, the motor torque ripples are filtered out by the rotor inertia. However, at low speeds, due to the low inertia filtering, the torque pulsations are large and can degrade the PMSM drive performance [25, 73]. Hence, in practice, the motor torque is expressed in the following general form

$$T_m = T_0 + \Delta T. \tag{5.15}$$

where T_0 is the dc component of torque and ΔT is the sum of harmonics generated by periodic torque pulsations; which are mainly due to cogging or non-

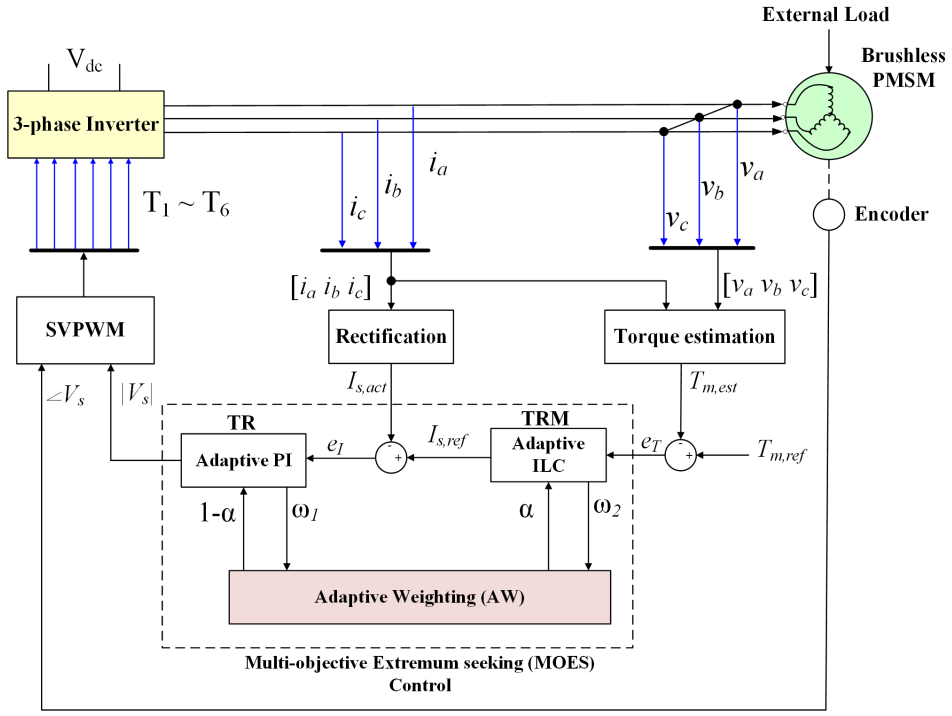

Figure 5.2: Block diagram of the proposed multi-objective extremum-seeking torque control (dashed line) applied to the exercise machine.

sinusoidal flux density distribution around the motor air gap. Generally, ΔT can be expressed in terms of low order harmonic components given by

$$\Delta T = T_1 sin(\rho\omega_r t + \theta_1) + T_2 sin(2\rho\omega_r t + \theta_2) + \sum_{i=1}^{\infty} T_{6i} sin(6i\rho\omega_r t + \theta_{6i}). \quad (5.16)$$

5.2 MOES Torque Control and Its Application to the Drive System

Fig. 5.2 shows the overall control block diagram of the drive system. The PMSM torque is controlled using the proposed MOES scheme which aims to satisfy two main objectives; namely torque ripple minimization (TRM) and torque regulation (TR) through TRM and TR blocks as shown in Fig. 5.2.

The TRM block utilizes an adaptive ILC scheme for which the gains are tuned based on a multi-variable sliding-mode extremum seeking (MSES) tuning method. To this end, the motor electromagnetic torque is estimated through the torque estimator block using (5.11). The proposed adaptive ILC generates the desired maximum amplitude of stator currents, $I_{s,ref}$, based on the torque error signal e_T. As shown in Fig. 5.2, the actual stator current I_s is obtained

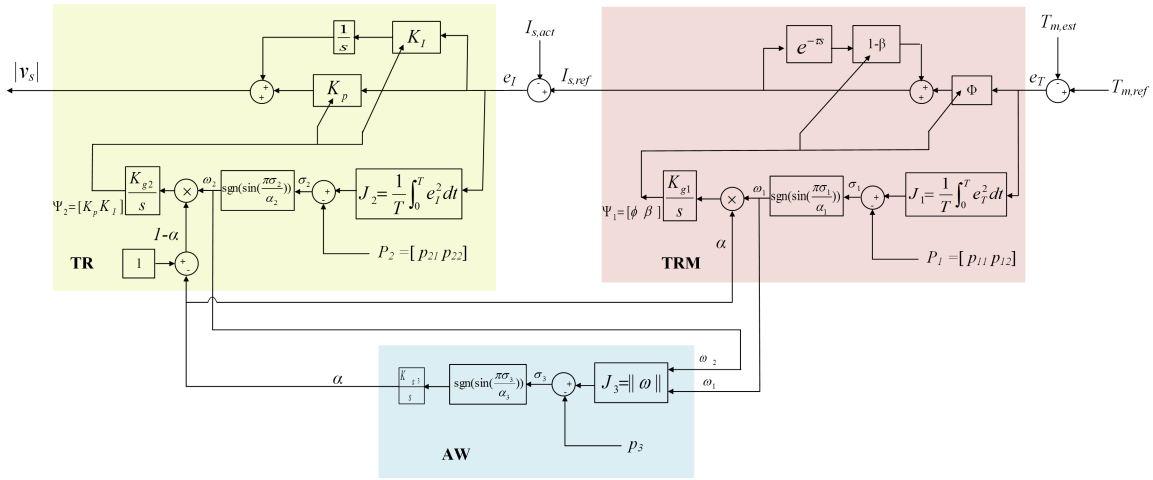

Figure 5.3: Block diagram of the proposed multi-objective torque control scheme.

through rectifying the stator three phase currents using the rectification method proposed in [86].

The TR block regulates the PMSM torque by controlling the magnitude of stator current using an adaptive PI controller for which the gains are tuned on-line based on MSES scheme. Then a scalar extremum seeking optimization is utilized in adaptive weighting (AW) block for scaling the two objective functions.

Additionally, the stator angular position is obtained through an encoder which is mounted on the motor shaft. The magnitude and angle of generated stator voltage are passed to a space SVPWM block to determine the switching sequence for the six switches of the inverter.

5.2.1 Torque Ripple Minimization (TRM) Block

For torque ripple minimization, an adaptive iterative learning control (AILC) scheme is proposed and applied to the system. The main idea of ILC is that by using the controller output data from the previous iteration cycle and the current error information, the control signal of the next iteration cycle is generated based on an iterative learning law [89].

Fig. 5.3 shows the proposed AILC scheme used in the TRM block. For torque ripple suppression it is required that the period of iteration cycle be consistent with that of the torque ripple. Hence, assuming that the period of iterative cycle is τ , one can take τ equal to the period of the first-order harmonic of torque ripple [68, 89]

$$\tau = 2\pi/\omega_r. \tag{5.17}$$

Assuming that the torque measurement is available, based on the TRM block in Fig. 5.3 the iterative learning law of the proposed AILC is as follows

$$I_{s,ref} = (1-\beta)e^{-\tau s} I_{s,ref} + \phi e_T \tag{5.18}$$

or equivalently

$$I_{s,ref}(k+1) = (1-\beta) I_{s,ref}(k) + \phi e_T(k+1) \tag{5.19}$$

where ϕ is the learning gain which is proportional to the torque ripple error e_T, and $k = 0, 1, 2, ...$ represents the k^{th} electrical cycle or the k^{th} iteration. The gain β is the relaxation (forgetting) factor which weakens the accumulative effect of non-periodic disturbance. The error $e_T(k+1)$ is obtained as follows

$$e_T(k+1) = T_{m,ref} - T_{m,est}(k+1) \tag{5.20}$$

where $T_{m,ref}$ and $T_{m,est}$ are the desired and estimated torques of the drive system, respectively. Considering (5.14), $e_T(k+1)$ can be written as

$$\begin{aligned} e_T(k+1) &= K_t(I_{s,ref} - I_{s,ref}(k+1)) \\ &= K_t(I_{s,ref} - [(1-\beta)I_{s,ref}(k) + \phi e_T(k+1)]) \\ &= K_t[(1-\beta)(I_{s,ref} - I_{s,ref}(k)) + \beta I_{s,ref} - \phi e_T(K+1)]. \end{aligned} \tag{5.21}$$

Considering the first line of (5.21), by substituting $k+1$ with k and multiplying two sides of equation by $(1-\beta)$, we have

$$(1-\beta)e_T(k) = K_t(1-\beta)(I_{s,ref} - I_{s,ref}(k)). \tag{5.22}$$

Substituting (5.22) in the last line of (5.21) yields

$$e_T(k+1) = (1-\beta)e_T(k) + K_t\beta I_{s,ref} - K_t\phi e_T(k+1). \tag{5.23}$$

As a result, $e_T(k+1)$ is obtained as follows

$$e_T(k+1) = \frac{1-\beta}{K_t\phi + 1} e_T(k) + \frac{K_t\beta I_{s,ref}}{1 + K_t\phi}. \tag{5.24}$$

The convergence condition is expressed as

$$|\rho| = |\frac{1-\beta}{K_t\phi + 1}| < 1. \tag{5.25}$$

Since $K_t > 0$, the convergence condition is satisfied with $\phi > 0$ and $|1 - \beta| < 1$. Hence, for $0 < \beta \leq 2$, the tracking error e_T will converge within a bound of $\frac{K_t \beta I_{s,ref}}{1+K_t\phi}$.

To have periodic torque ripple suppression in the steady state, it is desired that β be adequately small [89]. However, during a transient event, for instance a speed or load torque step, the system fails to present periodicity. In this case, according to (5.19), with smaller value of β in the range $(0, 2]$, the control signal $I_{s,ref}(k)$ of the current iteration will have a greater influence on the next iteration $I_{s,ref}(k+1)$. This leads to more significant accumulative effect of non-periodic disturbance. Hence, if the control signal from current iteration cycle is retained almost completely, it will inevitably lead to a greater fluctuation or longer settling time after that the transient happens. Therefore, during transient process the value of β cannot be very small and a fairy large value in the range of $(0, 2]$ is desirable. Moreover, the learning gain ϕ of the ILC is the same as the proportional gain in PID controller. To have periodic torque ripple suppression, larger values of ϕ are desired. However, ϕ cannot be selected to be very large since the controller becomes unstable.

Thus to adequately suppress the torque ripples under steady state condition, while preventing degradation of transient performance, an adaptive iterative learning control is proposed. The proposed scheme utilizes the multi-variable sliding-mode extremum seeking method for real-time tuning of the ILC gains $\boldsymbol{\Psi}_1 = [\phi \;\; \beta]$. This is achieved through minimization of the following cost function

$$J_1 = \frac{1}{T} \int_0^T e_T^2 dt \tag{5.26}$$

where T is the sampling period of the system, and e_T is defined as

$$e_T = T_{m,ref} - T_{m,est}. \tag{5.27}$$

The proposed scheme utilizes two sliding surfaces σ_{11} and σ_{12} to optimize parameters ϕ and β of the ILC. The vector of sliding surfaces is defined as

$$\boldsymbol{\sigma}_1 = [\sigma_{11} \;\; \sigma_{12}] \tag{5.28}$$

where $\sigma_{1i} = J - p_{1i}t$ such that $p_{1i} < 0 \;\; (i = 1, 2)$ is the slope of i^{th} sliding surface. Considering the vector of driving signals as

$$\boldsymbol{p}_1 = [p_{11} \;\; p_{12}] \tag{5.29}$$

Hence, the adaptive control law for tuning the gains of ILC is defined as follows

$$\dot{\boldsymbol{\Psi}}_1 = \alpha_1 K_{g1} sgn(sin(\frac{\pi \boldsymbol{\sigma}_1}{\boldsymbol{\gamma_1}})) \tag{5.30}$$

where α_1 is the weight associated to TRM block, $sgn(.)$ is a 2×1 signum vector, $\boldsymbol{\gamma_1} = [\gamma_{11} \;\; \gamma_{12}]^T$ is a 2×1 vector for which each element is a positive constant, and $K_{g1} = diag([k_{g11} \;\; k_{g12}])$ is a 2×2 diagonal positive definite matrix which determines the convergence rate. ES achieves the optimization by forcing J_1 to remain on the decreasing sliding surface vector, i.e., $\boldsymbol{\sigma_1} \to 0$. Thus, the system moves towards the optimum vector $\boldsymbol{\Psi}_1^* = [\phi^* \;\; \beta^*]^T$.

5.2.2 Torque Regulation (TR) Block

The detailed torque regulation (TR) block applied to the PMSM drive system is shown in Fig. 5.3. In this block, torque regulation is achieved using an adaptive PI controller for which the PI gains are tuned on-line based on multi-variable sliding-mode extremum-seeking method. The MSES tuning method covers the drawbacks of conventional PI controller by improving the controller performance in terms of tracking accuracy and robustness against disturbances [86]. This is achieved through minimization of the following cost function

$$J_2 = \frac{1}{T}\int_0^T e_I^2 dt \tag{5.31}$$

where $e_I = I_{s,ref} - I_{s,act}$. The MSES varies the input vector of the PI gains, $\boldsymbol{\Psi}_2 = [K_p \;\; K_i]$, such that J_2 is minimized. Similar to the MSES scheme utilized in the TRM block, the following optimization law is used for tuning the PI gains

$$\dot{\boldsymbol{\Psi}}_2 = \alpha_2 K_{g2} sgn(sin(\frac{\pi \boldsymbol{\sigma}_2}{\boldsymbol{\gamma_2}}) \tag{5.32}$$

where α_2 is the weight associated to TR block, $sgn(.)$ is a 2×1 signum vector, $\boldsymbol{\gamma_2} = [\gamma_{21} \;\; \gamma_{22}]^T$ is a 2×1 vector for which each element is a positive constant, and $K_{g1} = diag([k_{g21} \;\; k_{g22}])$ is a 2×2 diagonal positive definite matrix which determines the convergence rate. As J_2 is minimized, the system moves towards the optimum vector $\boldsymbol{\Psi}_2^* = [K_p^* \;\; K_i^*]^T$.

5.2.3 Adaptive Weighting (AW) Block

As discussed in previous sections, there are two control objectives assumed for the system. For torque ripple minimization, it is desired to minimize the objective function J_1 in the TRM block; while for torque regulation, the goal is to minimize the objective function J_2 such that the PI gains are tuned properly.

Hence, we are facing a multi-objective optimization problem and the performance information of the TRM and TR objective functions of the drive system is required.

When the motor is working at a constant speed (steady state), the torque ripple minimization becomes more critical than torque regulation. Hence, it is desired to increase the effect of TRM block so that the adaptive learning gain ϕ and the relaxation factor β will have a better effect on suppressing the torque ripples. During a transient process, the system fails to present periodicity. In such a case, it is desired to decrease the effect of relaxation factor β in the TRM block. On the other hand, it is required to increase the effect of TR block so that a faster and more precise regulation can be achieved.

The proposed scheme assigns an adaptive weight to each objective function using a scalar sliding-mode extremum seeking tuning method as shown in the AW block of Fig. 5.3. Hence, it does not require any performance information from the decision maker and can tune the weights online during the steady state and transient operation of the system.

The proposed MOES scheme optimizes the two objective functions (5.26) and (5.31) simultaneously by establishing an optimal trade-off between them and computing a set of optimal solutions for the system. Hence, the multi-objective problem is defined as

$$\lambda = \underset{\omega \in \chi}{arg\ min} ||\omega|| \tag{5.33}$$

where λ represents the minimum norm element and ω represents the convex combination of sliding-mode vectors $sgn(sin(.))$. To calculate the solutions of the multi-objective problem, we assign a weight to each objective function for scaling. This converts the multi-objective problem into a single objective function as follows

$$\chi = \Big\{\omega \in \mathbb{R} | \omega = \sum_{\mathrm{i}=1}^{2} \alpha_{\mathrm{i}} \mathrm{sgn}(\sin(\frac{\pi \boldsymbol{\sigma}_{\mathrm{i}}}{\boldsymbol{\gamma}_{\mathrm{i}}}));\ \ \alpha_{\mathrm{i}} \geq 0; \sum_{\mathrm{i}=1}^{2} \alpha_{\mathrm{i}} = 1\Big\}. \tag{5.34}$$

According to (5.34), since the number of objective functions is two, for simplicity consider α_1 and α_2 in (5.30) and (5.32) as $\alpha_1 = \alpha$ and $\alpha_2 = 1 - \alpha$; where α is the value obtained in the MOES block. In this study, the convex sum of

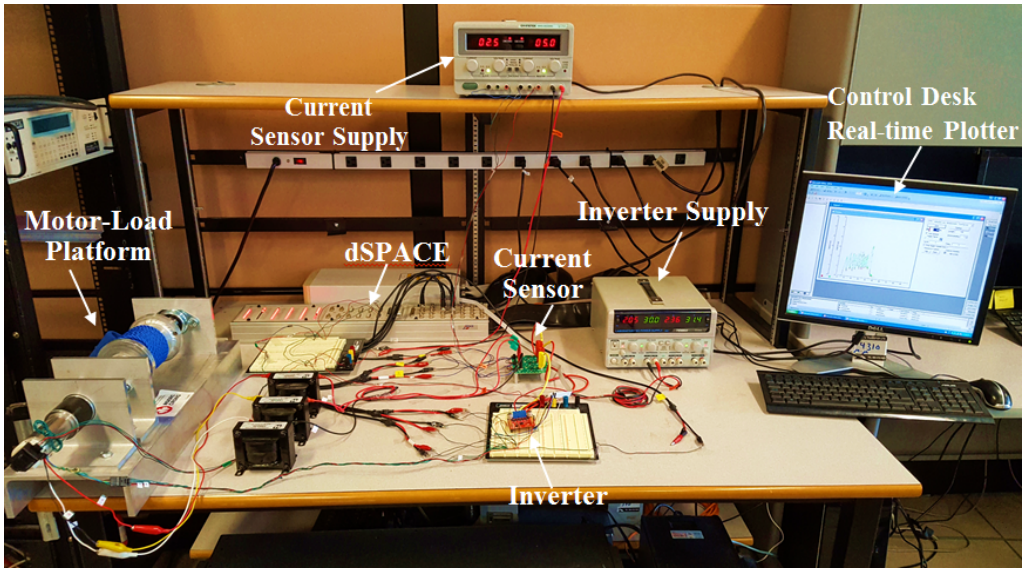

Figure 5.4: Experimental setup.

sliding-mode components gives the vector ω as

$$\begin{aligned}\omega &= \alpha\omega_1 + (1-\alpha)\omega_2 \\ &= \alpha \begin{bmatrix} sgn(sin(\frac{\pi\sigma_{11}}{\gamma_{11}})) & 0 \\ 0 & sgn(sin(\frac{\pi\sigma_{12}}{\gamma_{12}})) \end{bmatrix} + \\ &\qquad (1-\alpha) \begin{bmatrix} sgn(sin(\frac{\pi\sigma_{21}}{\gamma_{21}})) & 0 \\ 0 & sgn(sin(\frac{\pi\sigma_{22}}{\gamma_{22}})) \end{bmatrix}. \end{aligned} \quad (5.35)$$

Assuming $\omega_{11} = \alpha sgn(sin(\frac{\pi\sigma_{11}}{\gamma_{11}}))$, $\omega_{12} = \alpha sgn(sin(\frac{\pi\sigma_{12}}{\gamma_{12}}))$, $\omega_{21} = (1-\alpha)sgn(sin(\frac{\pi\sigma_{21}}{\gamma_{21}})))$, and $\omega_{22} = (1-\alpha)sgn(sin(\frac{\pi\sigma_{22}}{\gamma_{22}})))$, and using the Frobenius norm, $||\omega||$ is obtained as follows

$$||\omega|| = \sqrt{(\omega_{11}+\omega_{21})^2 + (\omega_{12}+\omega_{22})^2}. \quad (5.36)$$

The aim is to set the weights of multi-objective problem such that the minimum norm element λ is obtained, i.e., $||\omega||$ is minimized.

5.3 Experimental Evaluation

5.3.1 Implementation of Drive System

Fig. 5.4 shows the experimental setup which can be considered as a proof-of-concept exercise machine. A Maxon EC brushless permanent magnet synchronous motor is utilized to control the torque applied to the machine. Pa-

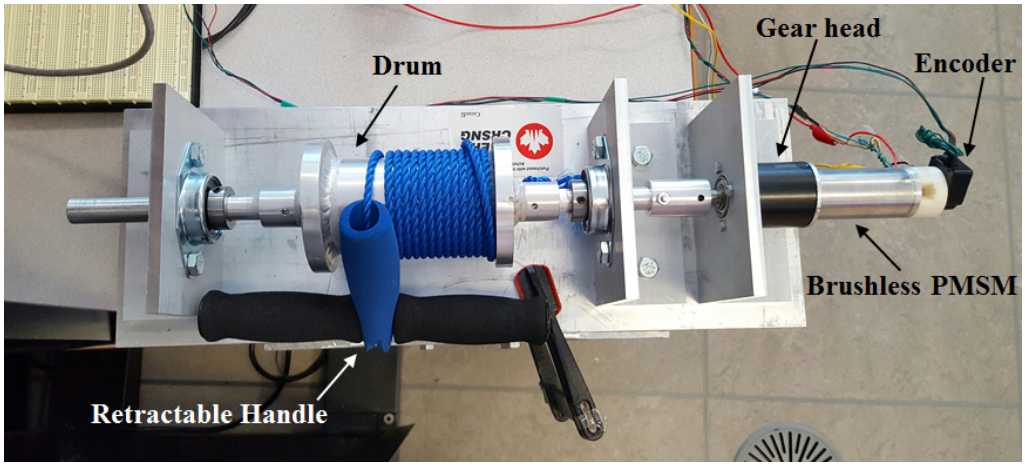

Figure 5.5: Motor-load platform of the setup.

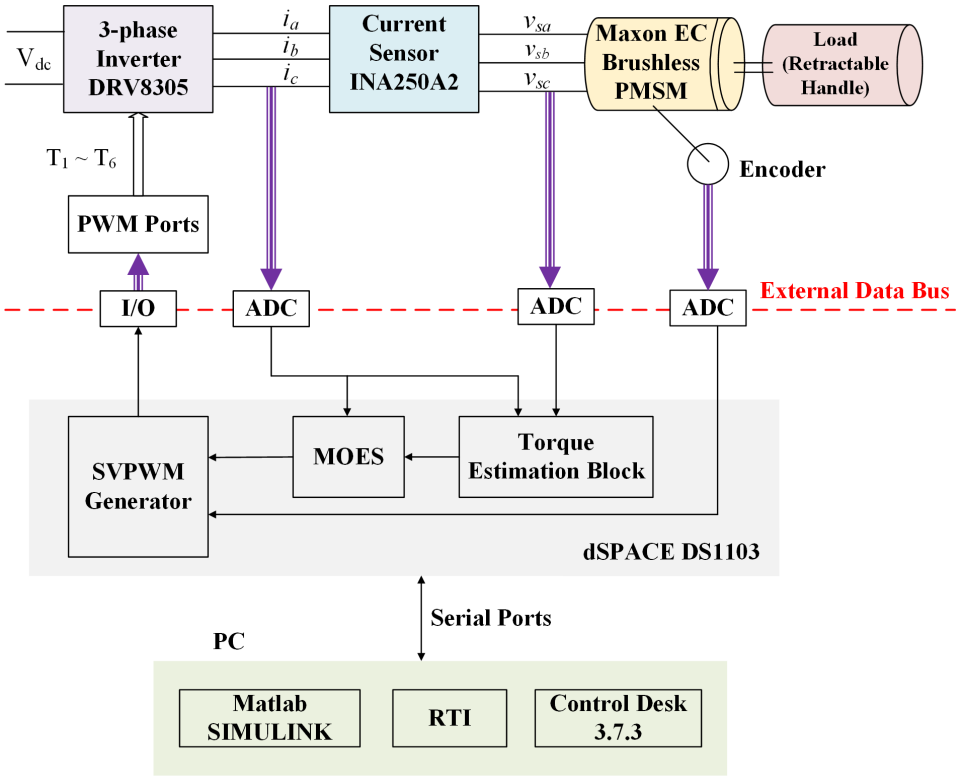

Figure 5.6: Real-time control structure of the setup using dSPACE control board.

rameters of the surface-mounted PMSM used in this study are listed in Table I.

Fig. 5.5 depicts the motor-load platform of the setup. As shown the PMSM is connected to an adjustable load through a gear head and motor shaft. The load

Table 5.1: Experimental Parameters of the Setup

Parameter	Value
Terminal resistance phase to phase	0.0829 Ω
Terminal inductance phase to phase	10.033 mH
Torque constant	0.14 N.m/A
Speed constant	659 rpm/V
Number of pole pairs	1
Inverter DC voltage supply	30 V
Rotor inertia	53.8 g.cm^2
SVPWM frequency	10 KHz
Gear ratio	6:1

is a retractable handle for which the force applied to can be adjusted manually by user. Moreover, an incremental optical encoder is employed for measurement of the rotor digital position and the resolution ratio is 1024 pulse per revolution (ppr).

Fig. 5.6, illustrates the real-time control/hardware configuration of the setup using dSPACE DS 1103 real-time control board. As shown, the measured rotor position as well as the stator three phase currents and voltages are sent to the controller through analog-to-digital converter (ADC) terminals of the dSPACE. The proposed controller was built in Matlab/SIMULINK environment with a sampling frequency of $f_s = 10\ kHz$ and its performance was studied using *dSPACE Control Desk 3.7.3*. The control block executes TRM and TR algorithms and generates the gate signals via SVPWM. The output gate signals of SVPWM are fed to the inverter switches through the I/O terminals of dSPACE. The performance evaluation of the proposed controller is presented in the following section.

5.3.2 Results

The proposed controller is applied to the exercise machine for the two cases i.e. damper and spring behavior of the machine. Performance of the proposed controller is studied under steady state and transient condition by comparing the results with an adaptive PI (API) controller. The API used in this study has been recently proposed in [86] for PMSM torque regulation which utilizes a similar MSES-tuned PI controller as the one in TR block of Fig. 5.3 and no TRM method. In the proposed controller, parameters of the MSE tuning scheme in the TRM block are initialized based on the discussion presented in 4.1.2 and

4.3.2 as follows: $K_{g1} = [7.5\ \ 0; 0\ \ 0.5]$, $\boldsymbol{\gamma_1} = [0.075\ \ 0.12]$, and $\boldsymbol{p_1} = [-0.5\ \ -0.6]$. Moreover, parameter initialization for the MSE tuning block of API the same as the one in TR block of the proposed controller as follows: $K_{g2} = [1.7\ \ 0; 0\ \ 0.3]$, $\boldsymbol{\gamma_2} = [0.06\ \ 0.07]$ and $\boldsymbol{p_2} = [-0.1\ \ -0.45]$. In the AW block, parameters of the scalar MSE tuning scheme are set as $K_{g3} = 0.5$, $\gamma_3 = 0.07$ and $p_3 = -1$.

Damping Effect

Assume that the controller is applied to the system and a user applies a force to the rope such that the motor speed changes from $\omega_r = 10rpm$ to $\omega_r = 20rpm$ at $t = 25s$. Then, the test is repeated for 10 times. However, due to space limitation, only the results for one repetition of the experiment are presented here. Fig. 5.7 depicts the experimental results for the API controller. As can be seen, the amplitude of motor torque changes proportionally to the speed variations from $T_m = 0.2N.m$ to $T_m = 0.5N.m$ at $t = 25s$. In this study, due to the small resistance of motor, we have utilized the torque estimation of (5.11) for which the ohmic losses of the motor windings are ignored. As shown in Fig. 5.7b, at low speeds, the amplitude of torque pulsations are considerable and a torque ripple minimization method is required to be applied to the system. Furthermore, the frequency spectrum of torque pulsations is also presented in Fig. 5.7e. This figure shows relatively high amplitudes for low-order harmonics at low speeds.

As shown in Fig.5.7a and b, as the transient condition happens during $[0s\ \ 3s]$ and $[25s\ \ 27s]$ the system fails to present periodicity and the tracking is not very precise. Hence, it is desired to increase the weight associated to the torque regulation block. During the steady state condition, the amplitude of periodic torque pulsations is considerable and torque minimization becomes more critical than torque regulation. To this end, the proposed multi-objective extremum-seeking controller is applied to the system and the experimental results are obtained as shown in Fig. 5.8. Utilizing an adaptive ILC scheme, the proposed controller achieves significant reduction in torque ripples as well as harmonic amplitudes (See Fig.5.8b and g). As shown in Fig. 5.8e, as the transient condition happens, the weight associated to the TR block, i.e. $1-\alpha$ increases so that the TR becomes more effective than TRM. Fig.5.8f shows the evolution of cost functions for TRM and TR blocks. Despite slight growth of the cost functions during the transient condition, the MSES tuning scheme used in TRM and TR blocks have adjusted the control parameters such that J_1 and J_2 are minimized and a high torque ripple suppression as well as a fast and precise tracking response is achieved.

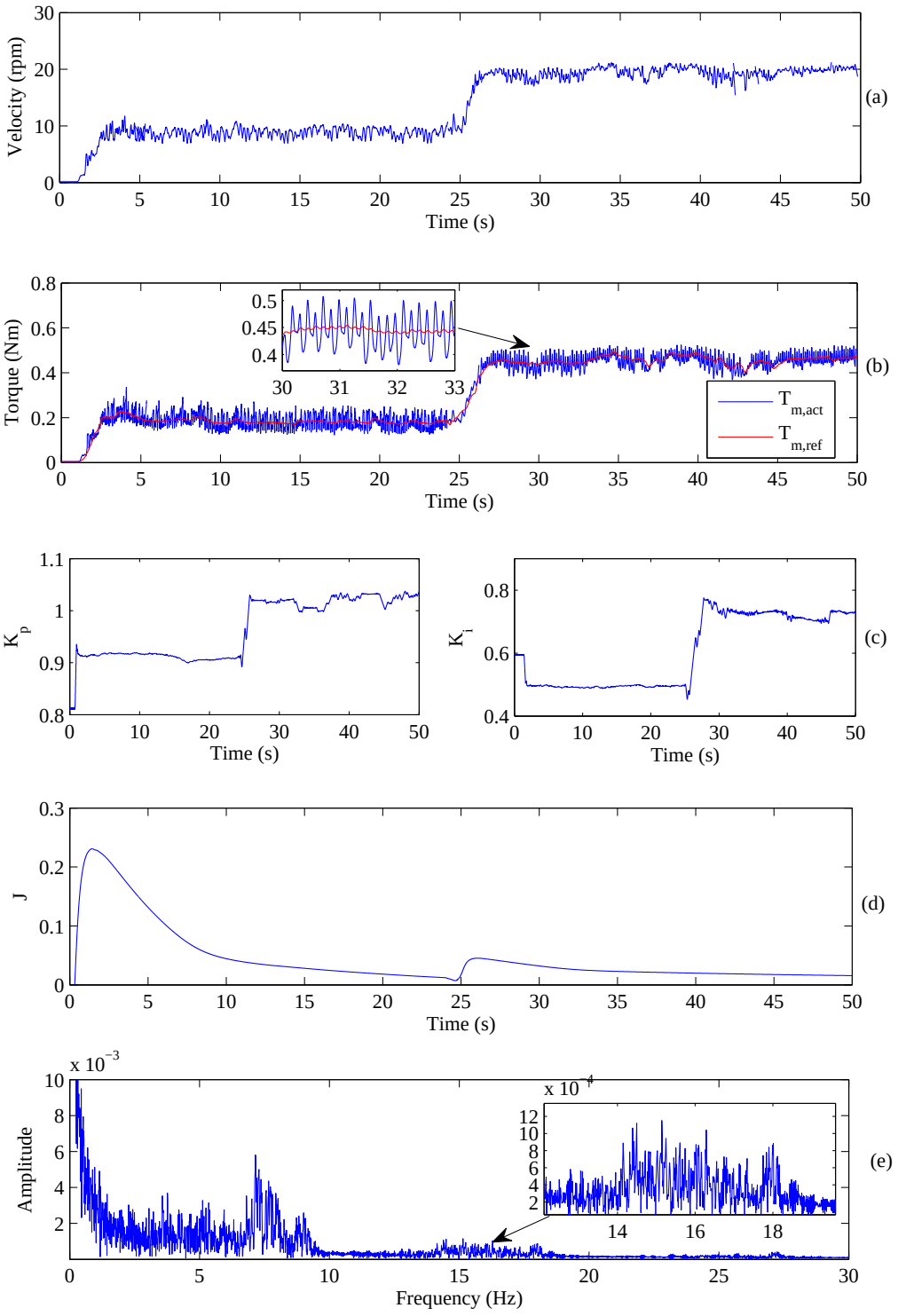

Figure 5.7: Damping-effect experimental results for the API controller: (a) rotor angular velocity, (b) torque response, (c) adaptive gains of PI, (d) evolution of cost function for MSES tuning, and (e) frequency spectrum.

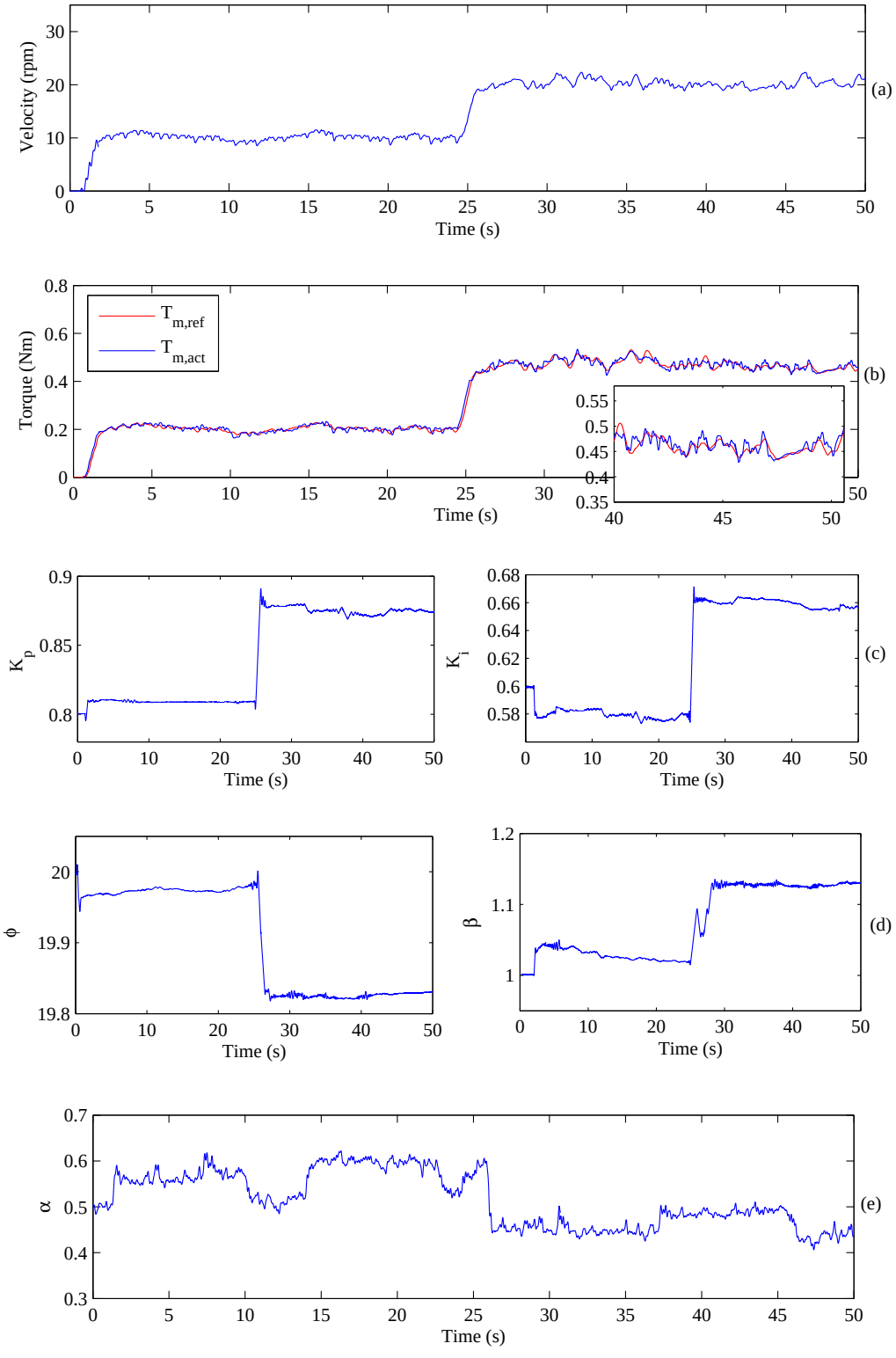
Velocity (rpm)
Time (s)
(a)
Torque (Nm)
$T_{m,ref}$
$T_{m,act}$
Time (s)
(b)
K_p
Time (s)
K_i
Time (s)
(c)
ϕ
Time (s)
β
Time (s)
(d)
α
Time (s)
(e)

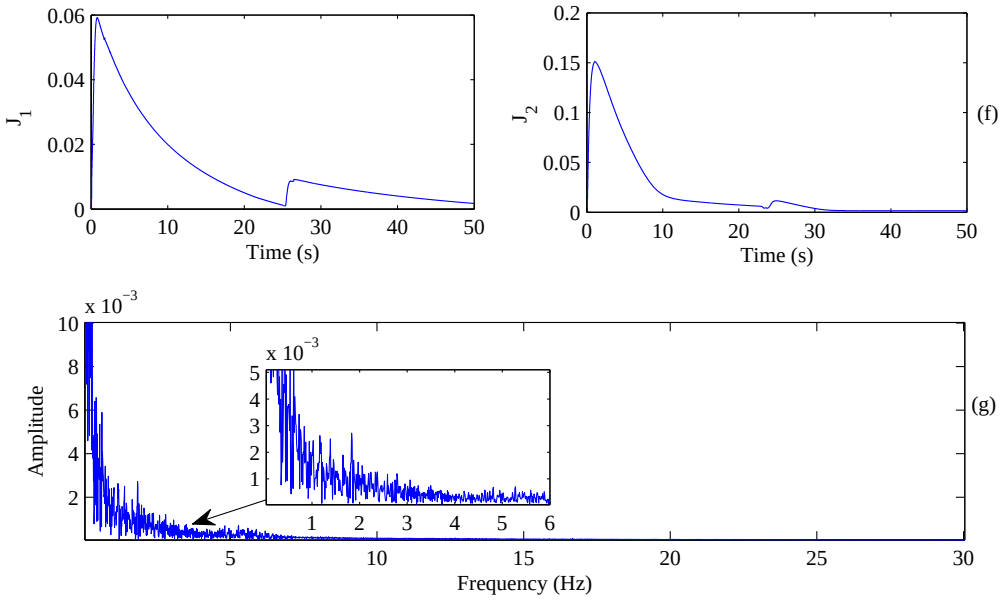

Figure 5.8: Damping effect experimental results for the proposed controller using MOES scheme: (a) rotor angular velocity, (b) torque response, (c) adaptive gains of PI, (d) adaptive gains of ILC, (e) multi-objective adaptive weight α, (f) evolution of cost function for MSES tuning in TRM (left) and TR (right) blocks, and (g) frequency spectrum.

Spring Effect

Now assume that we would like to generate mechanical spring behavior. The profile for displacement changes is as depicted in Fig. 5.9(a), where the user pulls the rope for $t = 10s$ to a distance of $x = 14cm$ from the initial place of the rope. Then the user keeps the rope at that place for $t = 25s$ and finally returns it to the beginning point with low speed. The performance of the proposed controller is compared with the API controller when the discussed displacement profile is applied to the exercise machine and the test is repeated for 10 times. Here, only the results for one repetition of the experiment are presented.

As shown in Fig. 5.9, the torque changes proportionally to displacement; however, the amplitude of torque ripples are high and a TRM method is required. Fig. 5.10 shows the experimental results when the proposed MOES controller is applied to the system for which the torque ripples have decreased for $\simeq 10\%$ compared with the result obtained using API controller. Furthermore, comparing the results for the TR cost function and frequency spectrum of the two controllers one can observe that the proposed controller has a lower cost function as well as lower amplitude harmonics. This is evidently shown in the

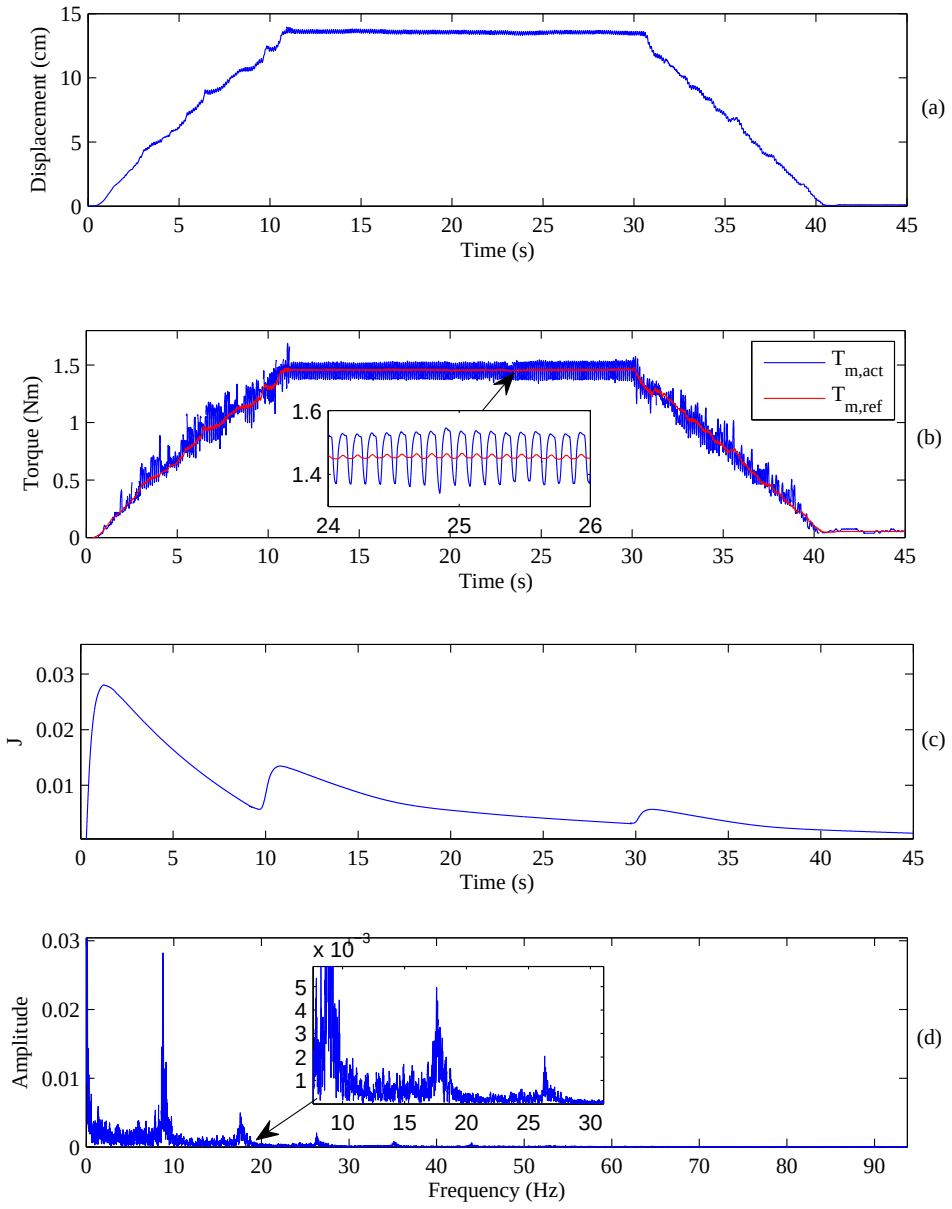

Figure 5.9: Experimental results for the API controller: (a) rope displacement, (b) torque response, (c) evolution of cost function for MSES tuning, and (d) frequency spectrum.

zoomed area of Fig. 5.9(d) and Fig.5.10(d) for the frequency interval of [0Hz 95Hz].

Furthermore, consider the torque ripple factor which is defined as the ratio of the peak-to-peak torque ripple to the rated torque of the PMSM [68]

$$TRF = \frac{T_{m,pk-pk}}{T_{m,rated}} \times 100 \tag{5.37}$$

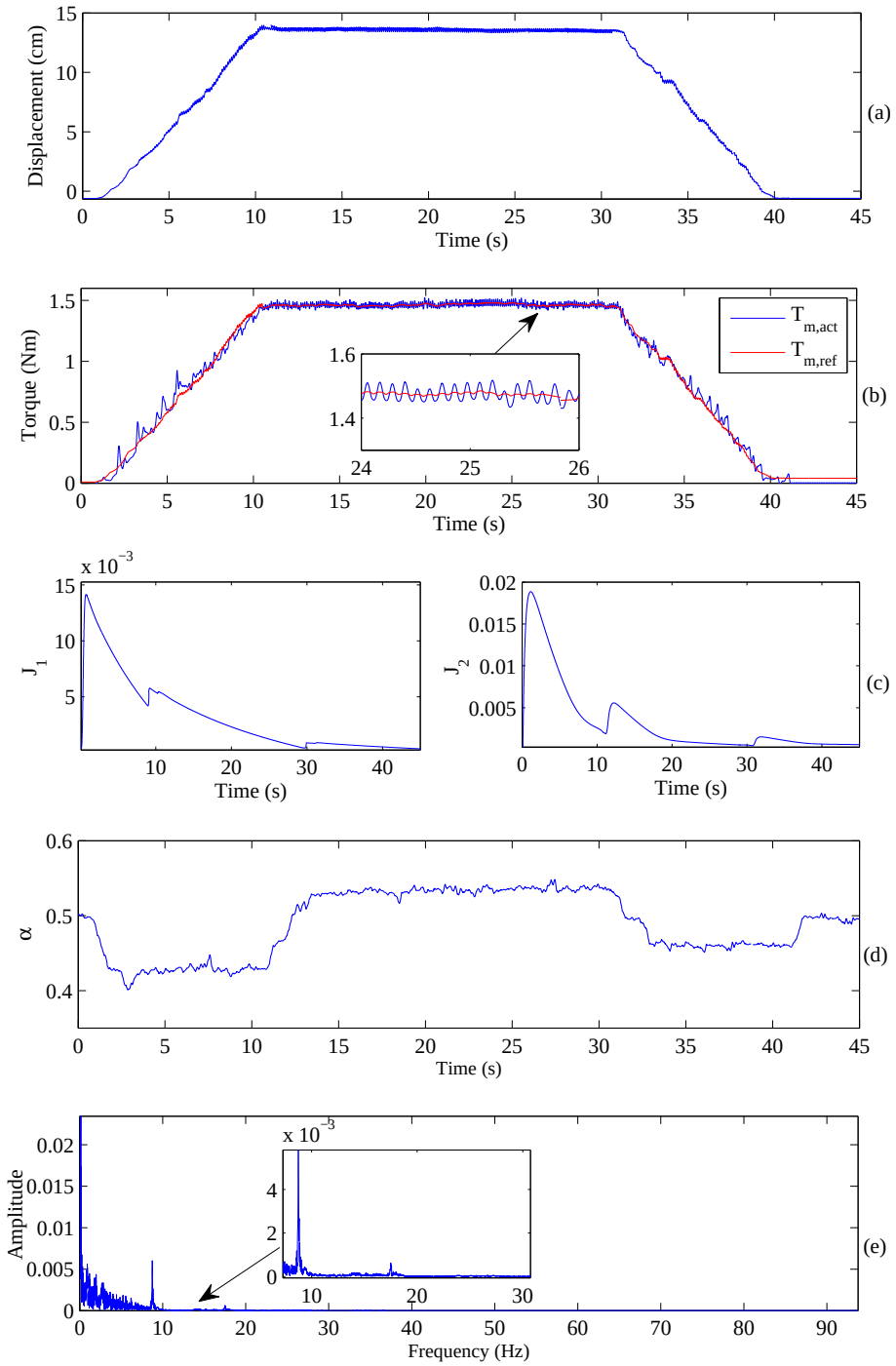

Figure 5.10: Experimental results for the proposed controller using MOES scheme: (a) rope displacement, (b) torque response, (c) evolution of cost function for MSES tuning in TRM (left) and TR (right) blocks, (d) multi-objective adaptive weight α, and (e) frequency spectrum.

Table 5.2: Comparison of the Average TRF for API and the proposed MOES controller

	Controller	TRF
Damping Effect	API	38%
	MOES	5%
Spring Effect	API	18%
	MOES	9%

Table 5.3: Comparison of the Average RMSE for API and the proposed MOES controller

	Controller	RMSE
Damping Effect	API	0.0275
	MOES	0.0227
Spring Effect	API	0.0128
	MOES	0.0036

Also consider the root-mean-square (RMS) of tracking error (e_I) over the first 6×10^5 iterations given by [54]

$$RMSE = \sqrt{\frac{1}{n}\sum_{p=0}^{n}(e_k)^2}. \tag{5.38}$$

where e_k is the error between the desired and actual motor torque at k^{th} iteration of the control, and n is the total number of iterations. To make a fair comparison, the average values obtained for the TRF and RMSE for 10 repetitions of the tests both for damping and spring behavior are presented in Table 5.2 and 5.3. As can be seen, the proposed MOES controller demonstrates a better performance, both in spring and damping behavior, when compared with the other controller.

5.4 Conclusion

In this chapter, a multi-objective extremum seeking optimization approach is proposed and applied for PMSM torque control. The proposed scheme utilizes an extremum seeking optimization for tuning the gains of an ILC and a PI controller such that high torque ripple suppression and accurate torque regulation for the PMSM is achieved under steady state and transient conditions. Performance of the proposed MOES-based controller was investigated through experiments

by comparing the results with a recently proposed adaptive PI controller. The results indicate the effectiveness of the proposed scheme in reducing the torque ripples up to 33% and 9% as well as improving the torque regulation up to 17% and 70% when the system is operated to create damping and spring behaviors, respectively.

Chapter 6

Summary, Conclusions, and Suggestions for Future Work

6.1 Summary and Conclusion

In this thesis, a multivariable sliding-mode extremum seeking scheme is proposed and its performance is studied in several power electronic control/optimization applications. The key contributions of the present dissertation can be summarized as follows:

1. The control design of the proposed multivariable sliding-mode extremum-seeking scheme was presented. Then a rigorous analysis of its convergence and stability both outside and inside the ϵ-vicinity of the extremum point was conducted.
2. The proposed scheme was applied for MPPT in an alternator-based energy conversion system through controlling the alternator field current and output voltage at various speeds. The experimental results demonstrate the efficiency of the proposed controller in achieving faster convergence and higher tracking accuracy when compared with a recently proposed multivariable gradient-based ESC.
3. The performance of the proposed scheme is verified in an optimization application. To this end, the proposed MSES is utilized for PI tuning in PMSM current regulation. The experimental results indicate that the proposed tuning method can improve the control performance in terms of accuracy, parametric variations and load torque disturbances when compared with recent controllers.
4. A multi-objective extremum-seeking scheme is proposed for PMSM torque ripple minimization and current regulation at low speeds. The proposed controller was applied on a proof-of-concept exercise machine and its performance was studied trough several experiments. The results validate the

effectiveness of the proposed controller in terms of torque ripple suppression, steady-state and transient performance, as well as load disturbance rejection.

6.2 Suggestions for Future Research

Based on the experience gained and the results obtained in the course of this research, the following suggestions may be considered for future work.

6.2.1 Studying the Effect of Coupling Elements in the Proposed MSES Controller

In the proposed MSES controller, K_g is defined as an $n \times n$ diagonal positive definite matrix. This leads to a straightforward stability analysis and low computational burden. If the coupling control parameters are considered as well, the precision of the control increases, while the system computational cost will increase which may not be suitable in some applications where fast tracking is required. Hence, a compromise should be made. In this regard, studying the effect of coupling elements in the proposed MSES controller would be an interesting topic for future work.

6.2.2 PMSM Sensorless Control

One main drawback of using high-resolution position sensors such as pulse encoder in PMSMs is their high cost. On the other hand, Hall-effect sensors have low precision at PMSM low-speed applications such as exercise machine. In this case, the sensor failure may cause instability in the control system [21]. Therefore, improving the proposed control strategy to a sensorless control scheme is an interesting topic for future work.

6.2.3 Removing External PMSM Inductances

The Maxon EC brushless PMSM used in Chapters 4 and 5 is a lightweight motor with small resistance and inductance values. This gives rise to higher levels of current/torque ripples as well as current rise time. Hence, in this study external inductances have been added to the PMSM phase terminals. However, using external inductances increases the system cost and size. Moreover, in some applications, using large inductors undesirably slows current control response. Therefore, removing the external inductances and changing the control topology such as using a multilevel DC link is proposed as continuation of the present work.

6.2.4 Regenerative Exercise Machine

To increase the efficiency of the proposed exercise machine in Chapter 5, it is desired to convert mechanical vibration energy generated by user in the motor-load platform into electric battery charge utilized as DC supply of inverter. To this end, extending the proposed controller as a power electronic regenerative control scheme is worth to be a subject of future work.

6.2.5 Using Variable DC Link in PMSM Control

In the designed exercise machine, if the back EMF voltage of PMSM becomes greater than the voltage of DC source, the direction of current flow changes to DC source. Hence, the DC source trips and disconnects. On the other hand, in regenerative case, a challenge happens when the back EMF voltage drops to small values. In this case, even if a boost converter is utilized in the circuit, the current is not enough to charge the battery. Therefore, as an other opportunity for future work, it is desired to change the system drive topology to have a variable DC link.

Bibliography

[1] Riccardo Antonello, Matteo Carraro, and Mauro Zigliotto. Maximum-torque-per-ampere operation of anisotropic synchronous permanent-magnet motors based on extremum seeking control. *IEEE Transactions on Industrial Electronics*, 61(9):5086–5093, 2014.

[2] Kartik B Ariyur and Miroslav Krstic. *Real-time optimization by extremum-seeking control*. John Wiley & Sons, 2003.

[3] Andrzej Banaszuk, Kartik B Ariyur, Miroslav Krstić, and Clas A Jacobson. An adaptive algorithm for control of combustion instability. *Automatica*, 40(11):1965–1972, 2004.

[4] Mehmet Baskin and Bulent Caglar. A modified design of PID controller for permanent magnet synchronous motor drives using particle swarm optimization. In *16th International Power Electronics and Motion Control Conference and Exposition (PEMC)*, pages 388–393, 2014.

[5] Todd D Batzel and Kwang Y Lee. Commutation torque ripple minimization for permanent magnet synchronous machines with hall effect position feedback. *IEEE Transactions on Energy Conversion*, 13(3):257–262, 1998.

[6] Frede Blaabjerg, Marco Liserre, and Ke Ma. Power electronics converters for wind turbine systems. *IEEE Transactions on industry applications*, 48(2):708–719, 2011.

[7] Frede Blaabjerg and Ke Ma. Future on power electronics for wind turbine systems. *IEEE Journal of Emerging and Selected Topics in Power Electronics*, 1(3):139–152, 2013.

[8] Milan Brejl and Michal Princ. Using the PMSM vector control eTPU function. *Application Note, Rev. 1*, 2006.

[9] Vahe Caliskan, David J Perreault, Thomas M Jahns, and John G Kassakian. Analysis of three-phase rectifiers with constant-voltage loads. *Circuits and Systems I: Fundamental Theory and Applications, IEEE Transactions on*, 50(9):1220–1225, 2003.

[10] Berk Calli, Wouter Caarls, Pieter Jonker, and Martijn Wisse. Comparison of extremum seeking control algorithms for robotic applications. In *2012 IEEE/RSJ International Conference on Intelligent Robots and Systems (IROS)*, pages 3195–3202, 2012.

[11] Ching Chuen Chan and KT Chau. An overview of power electronics in electric vehicles. *IEEE transactions on Industrial Electronics*, 44(1):3–13, 1997.

[12] S-H Chang, P-Y Chen, Y-H Ting, and S-W Hung. Robust current control-based sliding mode control with simple uncertainties estimation in permanent magnet synchronous motor drive systems. *IET Electric Power Applications*, 4(6):441–450, 2010.

[13] Lianghui Dong, Yingwei Huang, Juri Jatskevich, and Jinglin Liu. Improved fault-tolerant control for brushless permanent magnet motor drives with defective Hall sensors. *IEEE Transactions on Energy Conversion*, 31(2):789–799, 2016.

[14] Shufang Dong, Ke-Qian Lu, Jian Qiao Sun, and Katherine Rudolph. Adaptive force regulation of muscle strengthening rehabilitation device with magnetorheological fluids. *IEEE Transactions on neural systems and rehabilitation engineering*, 14(1):55–63, 2006.

[15] JM Enrique, E Duran, M Sidrach-de Cardona, and JM Andujar. Theoretical assessment of the maximum power point tracking efficiency of photovoltaic facilities with different converter topologies. *Solar Energy, Sci*, 81(1):31–38, 2007.

[16] Youssef Errami, Mohammed Ouassaid, and Mohamed Maaroufi. A performance comparison of a nonlinear and a linear control for grid connected PMSG wind energy conversion system. *International Journal of Electrical Power & Energy Systems*, 68:180–194, 2015.

[17] Shirin Fartash Toloue, Seyed Hossein Kamali, and Mehrdad Moallem. Multivariable sliding-mode extremum seeking PI tuning for current control of a PMSM. *IET Electric Power Applications*, 2019.

[18] Shirin Fartash Toloue, Seyed Hossein Kamali, and Mehrdad Moallem. Torque ripple minimization and control of a permanent magnet synchronous motor using multi-objective extremum seeking. *IEEE/ASME Transactions on Mechatronics*, 2019.

[19] Sh. FartashToloue and M. Moallem. Multivariable sliding-mode extremum seeking control with application to MPPT of an alternator-based energy conversion system. *IEEE Transactions on Industrial Electronics*, 64(8):6383–6391, 2017.

[20] Guodong Feng, Chunyan Lai, and Narayan C Kar. An analytical solution to optimal stator current design for PMSM torque ripple minimization with minimal machine losses. *IEEE Transactions on Industrial Electronics*, 64(10):7655–7665, 2017.

[21] José Carlos Gamazo-Real, Ernesto Vázquez-Sánchez, and Jaime Gómez-Gil. Position and speed control of brushless dc motors using sensorless techniques and application trends. *sensors*, 10(7):6901–6947, 2010.

[22] Aboozar Ghaffari, Miroslav Krstic, and Saradhi Seshagiri. Power optimization for photovoltaic microconverters using multivariable newton-based extremum seeking. *Control Systems Technology, IEEE Transactions on*, 22(6):2141–2149, 2014.

[23] Aboozar Ghaffari, Saradhi Seshagiri, and Miroslav Krstic. Power optimization for photovoltaic micro-converters using multivariable gradient-based

extremum-seeking. In *American Control Conference (ACC), 2012*, pages 3383–3388, 2012.

[24] Azao Ghaffari, Miroslav Krstic, and Sridhar Seshagiri. Extremum seeking for wind and solar energy applications. *Mechanical Engineering*, 136(3):S13, 2014.

[25] Alfonso Gómez-Espinosa, Víctor M Hernández-Guzmán, Manuel Bandala-Sánchez, Hugo Jiménez-Hernández, Edgar A Rivas-Araiza, Juvenal Rodríguez-Reséndiz, and Gilberto Herrera-Ruíz. A new adaptive self-tuning fourier coefficients algorithm for periodic torque ripple minimization in permanent magnet synchronous motors (PMSM). *Sensors*, 13(3):3831–3847, 2013.

[26] Feng Guihong, Li Yan, Luan Juli, and Zhang Bingyi. A position sensorless control system of low speed and high torque PMSM based on sliding mode observer. In *2007 International Conference on Electrical Machines and Systems (ICEMS)*, pages 974–978, 2007.

[27] Lennart Harnefors and H-P Nee. Model-based current control of AC machines using the internal model control method. *IEEE transactions on industry applications*, 34(1):133–141, 1998.

[28] Anthony J Healey and David Lienard. Multivariable sliding mode control for autonomous diving and steering of unmanned underwater vehicles. *Oceanic Engineering, IEEE Journal of*, 18(3):327–339, 1993.

[29] Chihchiang Hua and Chihming Shen. Study of maximum power tracking techniques and control of dc/dc converters for photovoltaic power system. In *Power Electronics Specialists Conference, 1998. PESC 98 Record. 29th Annual IEEE*, volume 1, pages 86–93, 1998.

[30] Reza Ilka, Yousef Alinejad-Beromi, and Hamid Yaghobi. Cogging torque reduction of permanent magnet synchronous motor using multi-objective optimization. *Mathematics and Computers in Simulation*, 2018.

[31] Rakib Islam, Iqbal Husain, Abbas Fardoun, and Kevin McLaughlin. Permanent magnet synchronous motor magnet designs with skewing for torque ripple and cogging torque reduction. In *2007 IEEE Industry Applications Annual Meeting*, pages 1552–1559, 2007.

[32] Z Jabbour, A Riwan, S Moreau, Jonathan Van Rhijn, and G Champenois. Identification and compensation of torque ripples of a PMSM in a haptic context. In *IECON 2010-36th Annual Conference on IEEE Industrial Electronics Society*, pages 1665–1670, 2010.

[33] Thomas M Jahns, Gerald B Kliman, and Thomas W Neumann. Interior permanent-magnet synchronous motors for adjustable-speed drives. *IEEE Transactions on Industry Applications*, (4):738–747, 1986.

[34] G Jayabaskaran, B Adhavan, and V Jagannathan. Torque ripple reduction in permanent magnet synchronous motor driven by field oriented control using iterative learning control with space vector pulse width modulation. In *International Conference on Computer Communication and Informatics (ICCCI)*, pages 1–6, 2013.

[35] Zhenyu Jia and Byeongwoo Kim. Direct torque control with adaptive PI speed controller based on neural network for PMSM drives. In *International Conference on Electrical Engineering, Control and Robotics (EECR)*, volume 160, pages 1–5, 2018.

[36] J-W Jung, Y-S Choi, VQ Leu, and HH Choi. Fuzzy PI-type current controllers for permanent magnet synchronous motors. *IET electric power applications*, 5(1):143–152, 2011.

[37] Shyam Kamal, Asif Chalanga, Kumar P Ramesh, and B Bandyopadhyay. Multivariable continuous integral sliding mode control. In *Recent Advances in Sliding Modes (RASM), 2015 International Workshop on*, pages 1–5, 2015.

[38] J Karthikeyan and R Dhana Sekaran. Current control of brushless DC motor based on a common dc signal for space operated vehicles. *International Journal of Electrical Power & Energy Systems*, 33(10):1721–1727, 2011.

[39] Ritesh Kumar Keshri and Prabhat Ranjan Tripathi. Torque estimator for a permanent magnet brushless DC motor drive. In *Transportation Electrification Conference (ITEC), 2015 IEEE International*, pages 1–5, 2015.

[40] Nick Killingsworth and Miroslav Krstic. Auto-tuning of PID controllers via extremum seeking. In *Proceedings of American Control Conference*, pages 2251–2256, 2005.

[41] Nick J Killingsworth and Miroslav Krstic. PID tuning using extremum seeking: online, model-free performance optimization. *IEEE control systems*, 26(1):70–79, 2006.

[42] SK Korovin and VI Utkin. Use of slip mode in problems of static optimization. *Automation and Remote Control*, 33(4):570, 1972.

[43] SK Korovin and VI Utkin. Using sliding modes in static optimization and nonlinear programming. *Automatica*, 10(5):525–532, 1974.

[44] Eftichios Koutroulis and Kostas Kalaitzakis. Design of a maximum power tracking system for wind-energy-conversion applications. *IEEE transactions on industrial electronics*, 53(2):486–494, 2006.

[45] Eftichios Koutroulis, Kostas Kalaitzakis, and Nicholas C Voulgaris. Development of a microcontroller-based, photovoltaic maximum power point tracking control system. *IEEE Transactions on power electronics*, 16(1):46–54, 2001.

[46] Miroslav Krstić. Performance improvement and limitations in extremum seeking control. *Systems & Control Letters*, 39(5):313–326, 2000.

[47] Miroslav Krstić and Hsin-Hsiung Wang. Stability of extremum seeking feedback for general nonlinear dynamic systems. *Automatica*, 36(4):595–601, 2000.

[48] Yeong-Chau Kuo, Tsorng-Juu Liang, Jiann-Fuh Chen, et al. Novel maximum-power-point-tracking controller for photovoltaic energy conversion system. *IEEE transactions on industrial electronics*, 48(3):594–601, 2001.

[49] BH Lam, SK Panda, J-X Xu, and KW Lim. Torque ripple minimization in PM synchronous motor using iterative learning control. In *Industrial Electronics Society, 1999. IECON'99 Proceedings. The 25th Annual Conference of the IEEE*, volume 3, pages 1458–1463, 1999.

[50] Shihua Li and Zhigang Liu. Adaptive speed control for permanent-magnet synchronous motor system with variations of load inertia. *IEEE Transactions on Industrial Electronics*, 56(8):3050–3059, 2009.

[51] Whei-Min Lin, Chih-Ming Hong, and Chiung-Hsing Chen. Neural-network-based MPPT control of a stand-alone hybrid power generation system. *IEEE transactions on power electronics*, 26(12):3571–3581, 2011.

[52] Jing Liu, Hongwen Li, and Yongting Deng. Torque ripple minimization of PMSM based on robust ILC via adaptive sliding mode control. *IEEE Transactions on Power Electronics*, 33(4):3655–3671, 2018.

[53] Ming-Hsiang Lo, Chang-Chieh Yu, Chu-Pin Su, Tzu-Yu Liu, Hui-Pin Huang, and Ming-Yang Cheng. Design and implementation of a vision-based treadmill system driven by a permanent magnet synchronous motor. In *Industrial Electronics Society, 2007. IECON 2007. 33rd Annual Conference of the IEEE*, pages 2892–2897, 2007.

[54] Slawomir Mandra, Krzysztof Galkowski, Harald Aschemann, and Andreas Rauh. Guaranteed cost iterative learning controlâĂŤan application to control of permanent magnet synchronous motors. In *9th International Workshop on Multidimensional (nD) Systems (nDS)*, pages 1–6, 2015.

[55] Thomas E Marlin and TE Marlin. *Process control: designing processes and control systems for dynamic performance*, volume 2. McGraw-Hill New York, 1995.

[56] Yao Meng and Xiangzhong Meng. Design and implementation of a PMSM servo drive system applied to intelligent patrol robots. In *IOP Conference Series: Materials Science and Engineering*, volume 397, page 012064. IOP Publishing, 2018.

[57] B Nahid Mobarakeh, F Meibody-Tabar, and FM Sargos. A self organizing intelligent controller for speed and torque control of a PMSM. In *Conference Record of the 2000 IEEE Industry Applications Conference. Thirty-Fifth IAS Annual Meeting and World Conference on Industrial Applications of Electrical Energy (Cat. No. 00CH37129)*, volume 2, pages 1283–1290, 2000.

[58] Yasser Abdel-Rady Ibrahim Mohamed and Ehab F El-Saadany. A current control scheme with an adaptive internal model for torque ripple minimization and robust current regulation in PMSM drive systems. *IEEE Transactions on Energy Conversion*, 23(1):92–100, 2008.

[59] Scott J Moura and Yiyao A Chang. Lyapunov-based switched extremum seeking for photovoltaic power maximization. *Control Engineering Practice*, 21(7):971–980, 2013.

[60] Tiago Roux Oliveira and Miroslav Krstić. Newton-based extremum seeking under actuator and sensor delays. *IFAC-PapersOnLine*, 48(12):304–309, 2015.

[61] H Khomami Pamsari, M Alizadeh Bidgoli, M Rajabzadeh, SMT Bathaee, and S Ozgoli. Application of a new multivariable sliding mode controller for the single machine infinite bus systems. In *Power Electronics, Drive Systems and Technologies Conference (PEDSTC), 2011 2nd*, pages 211–216, 2011.

[62] Tinglong Pan, Zhicheng Ji, and Zhenhua Jiang. Maximum power point tracking of wind energy conversion systems based on sliding mode extremum seeking control. In *2008 IEEE Energy 2030 Conference*, pages 1–5, 2008.

[63] Yaodong Pan and U Ozguner. Sliding mode extremum seeking control for linear quadratic dynamic game. In *Proceedings of the 2004 American Control Conference*, volume 1, pages 614–619, 2004.

[64] Yaodong Pan, Ümit Özgüner, and Tankut Acarman. Stability and performance improvement of extremum seeking control with sliding mode. *International Journal of Control*, 76(9-10):968–985, 2003.

[65] David J Perreault and Vahe Caliskan. A new design for automotive alternators. In *SAE CONFERENCE PROCEEDINGS P*, pages 583–594. SAE; 1999, 2000.

[66] David J Perreault and Vahe Caliskan. Automotive power generation and control. *IEEE Transactions on Power Electronics*, 19(3):618–630, 2004.

[67] K Pirabakaran and VM Becerra. Automatic tuning of PID controllers using model reference adaptive control techniques. In *Industrial Electronics Society, IECON 2001-27th Annual Conference of the IEEE*, volume 1, pages 736–740, 2001.

[68] Weizhe Qian, Sanjib K Panda, and Jian-Xin Xu. Torque ripple minimization in PM synchronous motors using iterative learning control. *IEEE Transactions on Power Electronics*, 19(2):272–279, 2004.

[69] Habib-ur Rehman and Longya Xu. Alternative energy vehicles drive system: Control, flux and torque estimation, and efficiency optimization. *IEEE Transactions on Vehicular Technology*, 60(8):3625–3634, 2011.

[70] G.V Rmana and S. Lalitha Kumari. a novel technique for PMSM drives to estimate the high resolution rotor position. *International Journal of Advanced Research in Electrical, Electronics and Instrumentaion Engineering*, 2(7):2860–2868, 2013.

[71] U Rupar, F Lahajnar, and P Zajec. Iterative-learning-based torque-ripple compensation in a transverse flux motor. *IET control theory & applications*, 6(3):341–348, 2012.

[72] Sanjib K Sahoo, Sanjib K Panda, and Jian-Xin Xu. Indirect torque control of switched reluctance motors using iterative learning control. *IEEE Transactions on Power Electronics*, 20(1):200–208, 2005.

[73] Wang Sibo, Zhao Huichao, Li Zhiyu, and Wang Xiaoxu. A new torque ripple test method based on pmsm torque ripple analysis for electric vehicles. In *EVS28 International Electric Vehicle Symposium and Exhibition*, pages 1–10, 2015.

[74] Hebertt Sira-Ramírez. Multi-variable sliding mode control. In *Sliding Mode Control*, pages 127–163. Springer, 2015.

[75] Jeongwon Sohn, Seungwoo Hong, and Myoungho Sunwoo. Alternator torque model based on equivalent circuit of synchronous generator for electric power management. *IEEE Transactions on Vehicular Technology*, 62(8):3593–3602, 2013.

[76] Jorge Solsona, Maria I Valla, and Carlos Muravchik. Nonlinear control of a permanent magnet synchronous motor with disturbance torque estimation. *IEEE Transactions on Energy Conversion*, 15(2):163–168, 2000.

[77] Wang Song, Shi Shuang-Shuang, and Chen Chao. Simulation of pmsm vector control system based on non-linear PID and its easy DSP realization. In *2009 Chinese Control and Decision Conference*, pages 949–953, 2009.

[78] Xinda Song, Jiancheng Fang, and Bangcheng Han. High-precision rotor position detection for high-speed surface PMSM drive based on linear Hall-effect sensors. *IEEE Transactions on Power Electronics*, 31(7):4720–4731, 2016.

[79] Masakazu Soshi, Nicholas Raymond, and Shinji Ishii. Spindle rotational speed effect on milling process at low cutting speed. *Procedia CIRP*, 14:159–163, 2014.

[80] DARJUSZ Swierczynski, M Kazmierkowski, and Frede Blaabjerg. DSP based direct torque control of permanent magnet synchronous motor (PMSM) using space vector modulation (DTC-SVM). In *IEEE Int. Symp. Ind. Electron*, volume 3, pages 723–727, 2002.

[81] Y Tan, WH Moase, C Manzie, D Nesic, and IMY Mareels. Extremum seeking from 1922 to 2010. In *29th Chinese Control Conference (CCC)*, pages 14–26, 2010.

[82] Akbar Tohidi, Ali Shamsaddinlou, and Ali Khaki Sedigh. Multivariable input-output linearization sliding mode control of dfig based wind energy conversion system. In *Control Conference (ASCC), 2013 9th Asian*, pages 1–6, 2013.

[83] Hamid A Toliyat, Mehdi Abolhassani, Peyman Niazi, and Lei Hao. DSP-based control of variable speed drives. In *Elsevier Power Electronics Handbook (Fourth Edition)*, pages 1303–1323. 2018.

[84] Hamid A Toliyat and Steven G Campbell. *DSP-based electromechanical motion control*. CRC press, 2003.

[85] Shirin Fartash Toloue and Mehrdad Moallem. A multi-surface sliding-mode extremum seeking controller for alternator maximum power point tracking. In *IECON 2015-41st Annual Conference of the IEEE Industrial Electronics Society*, pages 001501–001506, 2015.

[86] Shirin Fartash Toloue and Mehrdad Moallem. Torque control of a brushless DC motor using multivariable sliding mode extremum seeking PI tuning. In *Industrial Electronics Society, IECON 2017-43rd Annual Conference of the IEEE*, pages 2917–2922, 2017.

[87] Shirin Fartash Tolue and Mehrdad Moallem. Multivariable sliding-mode extremum seeking control with application to alternator maximum power point tracking. In *IECON 2016-42nd Annual Conference of the IEEE Industrial Electronics Society*, pages 229–234. IEEE, 2016.

[88] Limei Wang, Mingxiu Tian, and Yanping Gao. Fuzzy self-adapting PID control of PMSM servo system. In *2007 IEEE International Electric Machines & Drives Conference*, volume 1, pages 860–863, 2007.

[89] Changliang Xia, Weitao Deng, Tingna Shi, and Yan Yan. Torque ripple minimization of PMSM using parameter optimization based iterative learning control. *Journal of Electrical Engineering & Technology*, 11(2):425–436, 2016.

[90] Yan Xiao, Yaoyu Li, and John E Seem. Multi-variable extremum seeking control for mini-split air-conditioning system. 2014.

[91] Huimin Xu, Xuedong Zhang, and Xiangjie Liu. Predictive variable gain iterative learning control for PMSM. *Journal of Control Science and Engineering*, 2015:38, 2015.

[92] Jian-Xin Xu, Sanjib Kumar Panda, Ya-Jun Pan, Tong Heng Lee, and BH Lam. A modular control scheme for PMSM speed control with pulsating torque minimization. *IEEE Transactions on industrial electronics*, 51(3):526–536, 2004.

[93] Yunda Yan, Jun Yang, Zhenxing Sun, Chuanlin Zhang, Shihua Li, and Haoyong Yu. Robust speed regulation for pmsm servo system with multiple sources of disturbances via an augmented disturbance observer. *IEEE/ASME Transactions on Mechatronics*, 23(2):769–780, 2018.

[94] HT Yang, TH Tseng, TH Ai, YH Wu, and SH Yeh. A grid-connected energy conversion system for a treadmill with auto-transferring modes between a motor and a generator. In *Industrial Electronics Society, IECON 2015-41st Annual Conference of the IEEE*, pages 000316–000321, 2015.

[95] Her-Terng Yau, Chih-Jer Lin, and Chen-Han Wu. Sliding mode extremum seeking control scheme based on PSO for maximum power point tracking in photovoltaic systems. *International Journal of Photoenergy*, 2013, 2013.

[96] Chun Yin, YangQuan Chen, and Shou-ming Zhong. Fractional-order sliding mode based extremum seeking control of a class of nonlinear systems. *Automatica*, 50(12):3173–3181, 2014.

[97] Hai Yu and Umit Ozguner. Extremum-seeking control strategy for abs system with time delay. In *Proceedings of the 2002 American Control Conference (IEEE Cat. No. CH37301)*, volume 5, pages 3753–3758, 2002.

[98] Chunlei Zhang and Raúl Ordóñez. Numerical optimization-based extremum seeking control with application to abs design. *IEEE Transactions on Automatic Control*, 52(3):454–467, 2007.

[99] Hongwei Zhang, Fa-shan Yu, Xu-hui Bu, and FZ Wang. Robust iterative learning control for permanent magnet linear motor. *Electric Machines and Control*, 16(6):81–86, 2012.

[100] Yongpeng Zhang, Cajetan M Akujuobi, Warsame H Ali, Charlie L Tolliver, and L-S Shieh. Load disturbance resistance speed controller design for PMSM. *IEEE Transactions on Industrial Electronics*, 53(4):1198–1208, 2006.

[101] Ping Zheng, Jing Zhao, Jianqun Han, Jie Wang, Zhiyuan Yao, and Ranran Liu. Optimization of the magnetic pole shape of a permanent-magnet synchronous motor. *IEEE Transactions on Magnetics*, 43(6):2531–2533, 2007.